Oxidized Graphene on Ir(111): Wetting and Icephobic Properties Investigated on the Macroscopic and Atomic Scale

Signe Kyrkjebø

Masters Thesis in Physics

University of Bergen

Department of Physics and Technology

Supervisor: Bodil Holst

Co-supervisors: Liv Hornekær and Ranveig Flatabø

June 30, 2020

Abstract

Icing remains a huge challenge in a wide range of industries, from airplanes to optical sensors and wind turbines. Today's ice-combating approaches include thermal, mechanical, and chemical methods, which come with power, cost, and environmental drawbacks. The development of an icephobic coating, which is a coating that repels ice formation, will have huge advances. The lightweight, durability, and optical transparency of graphene, a 2D carbon material, makes it an interesting material for coatings. Graphene oxide is one of the most common graphene derivatives. Chemically synthesized graphene oxide is hydrophilic and has been predicted to have superior icephobic properties. A new type of oxidized graphene was discovered on Ir(111) in 20018, where the dominating functional group on the basal plane is enolates.

This thesis work presents the first study of the wetting and icephobic properties of oxidized graphene on Ir(111). Two O-Gr/Ir(111) samples with low ($\sim$ 8 %) and high (saturated) oxygen coverage, were prepared and characterized in ultra-high vacuum by scanning tunneling microscopy and x-ray photoelectron spectroscopy. These samples are referred to as the low- and high-coverage sample throughout this thesis. The icephobic and wetting surface properties of O-Gr/Ir(111) were studied under ambient conditions by measuring the water contact angles, the freezing onset temperature, and the freezing delay times. The sample with saturated oxygen coverage was characterized by scanning tunneling microscopy and x-ray photoelectron spectroscopy after the icing experiments to investigate the durability of the coating on the atomic level.

The results show that oxidized graphene on Ir(111) is almost hydrophobic under ambient conditions with a water contact angle of $71^\circ \pm 5^\circ$ and $77^\circ \pm 6^\circ$ for the low- and high-coverage sample, respectively. The water contact angle is similar to that of bare Ir(111) and appears to be independent of the oxygen coverage indicating that oxidized graphene on Ir(111) is transparent to wetting. The freezing onset temperature is found to be $-18°\text{C} \pm 1°\text{C}$ and $-21°\text{C} \pm 1°\text{C}$ for the low- and high-coverage sample, respectively. Thus, the freezing onset temperature appears to decrease with increasing oxygen coverage. The surface analysis after the icing experiments show that oxygen species and/or water intercalates through graphene edges between the graphene layer and the Ir(111) substrate, accompanied by the loss of oxygen-containing functional groups. An article on the basis of these results will be submitted to Carbon, and is included in the Appendix

B.2.

Acknowledgments

I wish to express my sincere appreciation to my supervisor professor Bodil Holst to give me the opportunity to work with this project, for her encouragement and her knowledge that together provided for an excellent guidance throughout this thesis. I want to express my gratitude to co-supervisor professor Liv Hornekær at the institute of Science and Technology at Aarhus University, to welcome me to the Surface Dynamics Group and for giving valuable and constructive suggestions throughout this project. I would like to thank my co-supervisor researcher Ranveig Flatabø at University in Bergen for guidance and valuable experience through the wetting and icing experiment, for all discussions, insightful thesis input and last but not least, for the social support. A special thanks to researcher assistant Andrew Cassidy and former postdoc Martha Scheffler at Aarhus University for serving the great amount of assistance and guidance to anything XPS, STM and UHV chamber related, as well as continuous input on the thesis writing. It has been great to have your patience and knowledge as support during this project.

I would like to acknowledge the rest of the Surface Dynamics group in Aarhus University and the Nanophysics group in Bergen for providing great working environments, for input over coffee and group meetings. Finally, I must express gratitude to my partner Mikkel, and to my family and friends for their love and support throughout this thesis.

Contents

Chapter 1

Introduction

Ice formation remains a huge challenge for a wide range of outdoor equipment operating in cold climates, such as road, air, and sea transportation, power transmission lines, optical sensors, and wind turbines. Until the last decade, the main focus in research and industry has been directed towards de-icing techniques, which aim to remove ice *after* accumulation. Current strategies involve i) thermal heating, ii) the mechanical method (e.g. ice removed by scratching), and iii) chemical method (e.g. fluids applied to lower the freezing point via chemical reagents) [1]. These techniques are generally inefficient, as they are energy and time consuming, and often have a negative effect on the environment. Icephobic surfaces are surfaces that repel ice formation, and represents a more desirable approach in combating ice because they prevent ice accumulation *before* it takes place. However, there are few icephobic surfaces that have industrial applications to this date, and thus the development of robust icephobic coatings will have huge advances and are of tremendous importance [2].

The lightweight, durability, and optical transparency of graphene, a 2D carbon material, make it an interesting material for coatings. Graphene oxide is one of the most common graphene derivatives. The potential applications of graphene oxide include energy storage [3], water treatment [4], sensors [5] and protective coatings [6]. Chemically synthesized graphene oxide is hydrophilic and is predicted to have superior icephobic properties. Among others, Zoakie et al. [7], have theoretically predicted the freezing onset temperature for water between two graphene oxide sheets to be -37°C.

In 2018, a new type of oxidized graphene was discovered on iridium(111). On this surface, the dominating functional group on the basal plane is enolates [8]. Up to the beginning of this thesis work the macroscopic wetting and icing properties of this surface had not been studied/investigated.

1.1 Thesis Objective

- To perform the first investigation of wetting and icing properties of oxidized graphene on Ir(111). The measurements carried out were water contact angles (WCA), freezing onset temperature, and freezing delay.
- To perform atomic level surface analysis (scanning tunneling microscopy and x-ray photoelectron spectroscopy) to correlate the surface chemistry with the macroscopic properties.
- To perform atomic level surface analysis before and after the macroscopic experiments to investigate the durability of the coating on the atomic level.

1.2 Thesis Overview

Chapter 2 provides a brief introduction to the theory of the wetting and icephobic properties of a surface, including a discussion of how the two are related. Chapter 3 presents a brief overview of the experimental work done on graphene, graphene growth, and functionalization of graphene, and argue why functionalized graphene can be a good candidate for an icephobic coating. Chapter 4 describes the different experimental techniques used, and chapter 5 provides detailed information on material preparation and measurements. Finally, the experimental results are presented and discussed in chapter 6. Conclusion and suggestions for future work are presented in chapter 7.

Chapter 2

Theory of Wettability and Ice Nucleation

This chapter provides the fundamental concepts behind the wetting of surfaces and relates this to icephobicity. Firstly, a definition of the therm icephobicity is presented. Secondly, the wetting of a surface is discussed, followed by an introduction of classical nucleation theory. The chapter finishes with a discussion of superhydrophobicity and icephobicity. The icing and wetting properties of graphene and functionalized graphene is discussed in Chapter 3.

2.1 Icephobicity

Icephobicity is the ability of a surface to prevent and/or to repel ice formation. An ideal icephobic surface can be characterized by the following criteria: i) a low median freezing onset temperature T_O, defined as which temperature ice nucleates in a sessile water droplet placed on a surface when the entire system is cooled in a slow, quasi-steady manner or a long ice nucleation time, τ_{av}, defined as the average time required for ice to nucleate in a supercooled droplet [9, 10], ii) low ice adhesion strength (lower than 100 kPa) so that when ice is formed, it can easily be removed [11, 12], and iii) a long-term durability [2]. Thus, developing icephobic surfaces is a complex task, and it has proved challenging to develop robust icephobic surfaces for real-life outdoors installations. To develop an icephobic surface, detailed knowledge about dynamic wetting, thermodynamics (the nucleation theory), and surface topography and chemistry is required. In this thesis work, the freezing onset (T_O) and the freezing delay time (τ_{av}) were used as metrics to investigate the icephobicity of the oxidized graphene surface. Additionally, the durability of the surface was investigated by comparing the surface before and after the icing experiments.

2.2 Liquid-Solid Interactions and Wetting

Wetting is the ability of a liquid to maintain contact with a solid surface defined by the molecular interactions between two interphases. In a bulk phase, the molecules are held together by forces (F) that equilibrate each other and therefore the net force is zero. At the interphase, however, some forces are missing which results in a net force pointing in towards the bulk phase. Work has to be done against this force to bring an atom or a molecule to the interface. This work is stored in the atom or molecule at the interphase as potential energy [13]. As such, the interfacial energy is defined as the work (W) required to build an area of a particular surface. In liquids, the interfacial energy can be expressed as [13],

$$\gamma = \frac{\Delta W}{\Delta A} = \frac{F\Delta x}{\Delta A}; \qquad [\gamma] = \frac{N}{m}, \tag{2.1}$$

where ΔA is the increase of the interfacial area and x is the distance the atom/molecule has to travel.

Note that this equation is not valid for solid interfaces. For a solid interphase, the work needed to displace atoms and molecules in the bulk has to be considered. Theoretical methods can be implemented but will not be elaborated in this thesis work. The most common way to experimentally measure the interfacial surface energy is through water contact angle experiments [14].

2.2.1 The Static Contact Angle

Ideal Surfaces

Figure 2.1 shows a droplet sitting on an ideal, i.e. smooth and chemically homogeneous, surface. The water contact angle, θ, is measured along the boundary of the three-phase (solid-liquid-vapor) contact line.

If the contact line is displaced with a quantity of dx along the solid surface (as shown in figure 2.2), the surface energies can be balanced as follows [15]:

$$dE = dx \cdot (\gamma_{sl} - \gamma_{sv}) + dx \cdot \gamma_{lv} cos\theta, \tag{2.2}$$

where γ_{lv}, γ_{sl} and γ_{sv} denote the liquid-vapor, surface-liquid and surface-vapor interfacial energy, respectively. At equilibrium, E is minimum, i.e. $dE/dx = 0$, and the equation reduces to Young's equation [16, 17]:

$$\gamma_{lv} cos(\theta_Y) = \gamma_{sv} - \gamma_{sl}, \tag{2.3}$$

where θ_Y is the equilibrium contact angle. Hence, the contact angle is strongly dependent on the interfacial energies of the system.

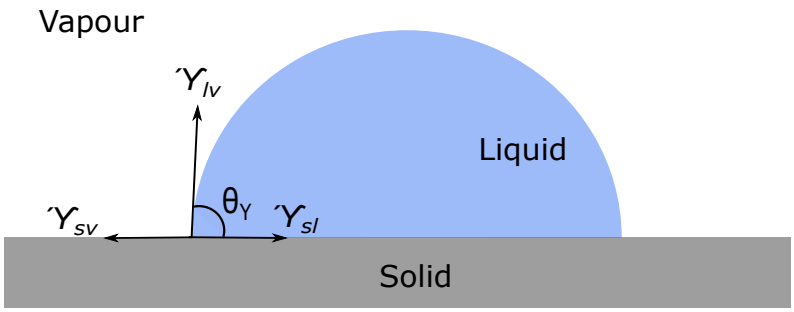

Figure 2.1: A dropet siting on a surface. θ is the droplet-solid contact angle, and γ_{sv}, γ_{lv}, and γ_{sl} denotes the solid-vapor, liquid-vapor and solid-liquid interfacial energy, respectively.

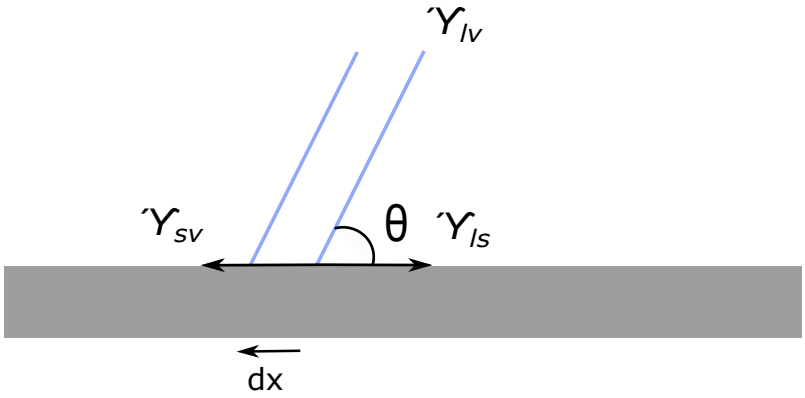

Figure 2.2: The contact line displaced by the quantity dx.

In figure 2.3, surfaces with different wettabilities are presented. Surfaces with contact angles lower than 90° are *hydrophilic* and are surfaces where wetting is favorable. Surfaces with contact angles greater than 90° are *hydrophobic* and are surfaces where wetting is unfavorable. More extreme, surfaces with contact angles lower than 5° are called superhydrophilic and are extremely easy to wet. Contrary, surfaces with contact angles greater than 150° are called superhydrohpobic and are extremely difficult to wet. Early research on icephobicity was centered on the idea that superhydrophobic surfaces would also be icephobic, because water is repelled from these surfaces. The relation between wetting and icephobicity is discussed in more detail in section 2.4. Details about the wetting on graphene and functionalized graphene can be found in section 3.4 and section 3.5, respectively.

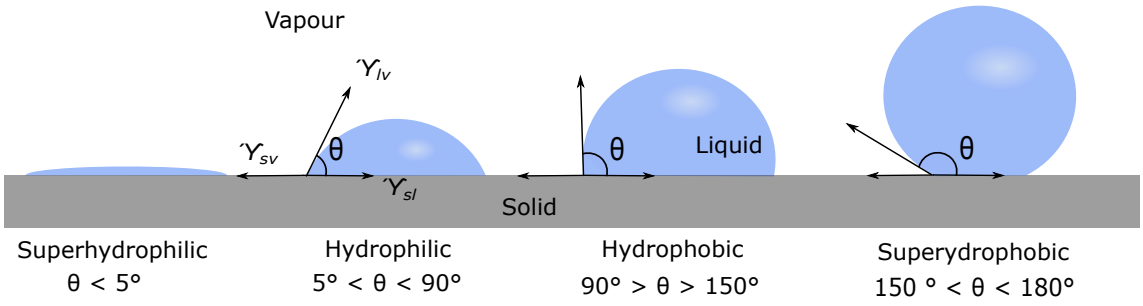

Figure 2.3: Wetting of different fluids. From left to right: the surface obtain extremely high wetting, high wetting, low wetting, and extremely low wetting properties.

Real Surfaces

Real surfaces do not have perfect smoothness but consist of physical and chemical heterogeneity. The regime on real rough surfaces can be divided into two competing categories: homogeneous wetting regime, or heterogeneous wetting regime. These two regimes are mainly described by two models, the Wenzel model and Cassie-Baxter model, respectively. Both models are only valid when the droplet is much larger than the textured surface scale.

The Wenzel model [18] describes the homogeneous wetting regime, where the droplet is in touch with the concave sites at the rough surface, as illustrated in fig 2.4a). Wenzel extended Young's equation to include the surface roughness by introducing the surface roughness factor, r [117]:

$$r = \frac{A_{actual}}{A_{apparent}}. \tag{2.4}$$

A_{actual} is the solid-droplet contact area (shown with the green lines in figure 2.4a)) and $A_{apparent}$ is the apparent area solid-droplet contact area (shown with the red line in figure 2.4a)). Young's equation is then modified to [18]:

$$cos(\theta_W) = r \cdot cos(\theta_Y), \tag{2.5}$$

where θ_W is the apparent contact angle. θ_Y is the contact angle of the smooth surface with the same material. If $r > 1$ and the surface is hydrophobic ($\theta > 90°$), the contact angle increase with roughness.

The Cassie-Baxter model [19] describes the heterogeneous wetting regime, where the surface topography is not filled with water but contains trapped air, as shown in figure 2.4b). This system

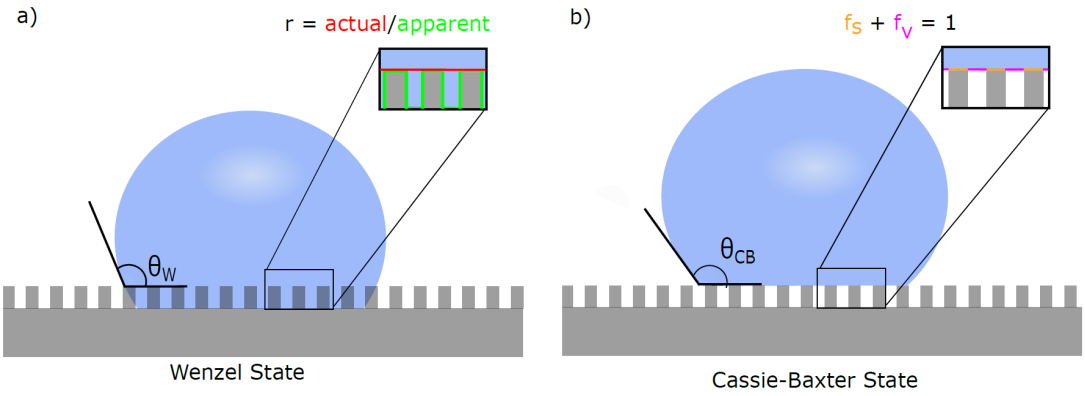

Figure 2.4: Illustration in droplet in a) Wenzel state. The and b) Cassie-Baxter State

consists of two domains; one is the droplet-solid area and the other is the droplet-vapor area. If f_s is the fraction of the droplet-solid contact area (shown with the orange lines) over the apparent area and f_v is the droplet-vapor contact area (shown with the pink lines) over the apparent area, the Cassie equation [20] describes a chemical two-component surface by:

$$cos(\theta_C) = f_s cos(\theta_{Y,s}) + f_v cos(\theta_{Y,v}), \tag{2.6}$$

where $\theta_{Y,s}$ and $\theta_{Y,v}$ is Young's contact angle on solid and vapor substrate, respectively.

The Cassie-Baxter model assumes that the local contact angle on the trapped air is $\theta_{Y,v} = 180°$. Since $f_s + f_v = 1$, the Cassie equation 2.6 can be expressed as the Cassie-Baxter equation [19]:

$$cos(\theta_C B) = -1 + f_s(cos\theta_{Y,s} + 1). \tag{2.7}$$

Furthermore, the Cassie-Baxter equation can be modified to take the roughness r of the solid surface into account [21]:

$$cos(\theta_{CB}) = -1 + r \cdot f_s(cos\theta_{Y,s} + 1). \tag{2.8}$$

If $f_s = 1$ the Cassie-Baxter equation becomes the Wenzel equation. A droplet in the Cassie-Baxter state exhibit less angle hysteresis, it is more mobile and thus has lower contact angle hysteresis (discussed in section 2.2.2), and has lower adhesion to the surface compared to a droplet in Wenzel state. On superhydrophobic surfaces, the Cassie-Baxter state is to be preferred over the Wenzel state.

2.2.2 The Contact Angle Hysteresis

Figure 2.5a) and b) shows the relation between Gibbs energy and the apparent contact angle for a liquid on an ideal and real surface, respectively. From this figure, it is clear that on an ideal surface, only one contact angle is stable. On a real surface, however, several local metastable contact angles can exist. Real surfaces exhibit two limiting values of the contact angle; the receding contact angle θ_r (minimum) and the advancing contact angle θ_a (maximum). The difference between these two angles is referred to as the contact angle hysteresis, H [22]:

$$H = (cos\theta_r - cos\theta_\alpha). \tag{2.9}$$

Physical and chemical heterogeneities will induce local metastable contact angles by the so-called pinning effect, as shown in figure 2.6. These heterogeneities will directly affect the hysteresis [23] and hence, the contact angle hysteresis provides a direct measure of the physical and chemical heterogeneity of a surface. One common way to measure the hysteresis experimentally is by using the volume addition and subtraction technique [22]. By adding volume to a droplet, the advancing contact angle can be found, and similarly, by withdrawing volume from the same droplet, the receding contact angle can be found.

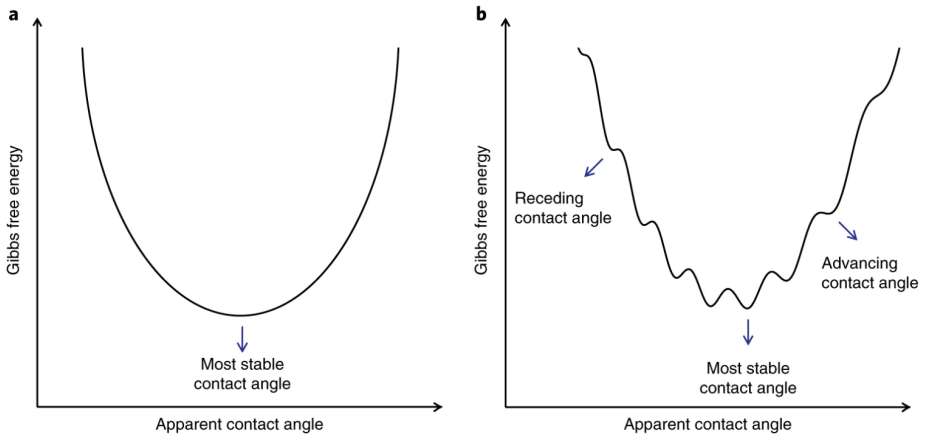

Figure 2.5: The relation of gibbs fre energy of an ideal and real wetting system and the apparent contact angle. a) An ideal wetting system has only one stable contact angle (Young's contact angle). b) A real surface has a global free energi minimum but also local, metastable minima. The largest measurable contact angle is the adcvanced contact angle, and the lowest measurable contact angle is the receding contact angle. Illustration copied from [22]

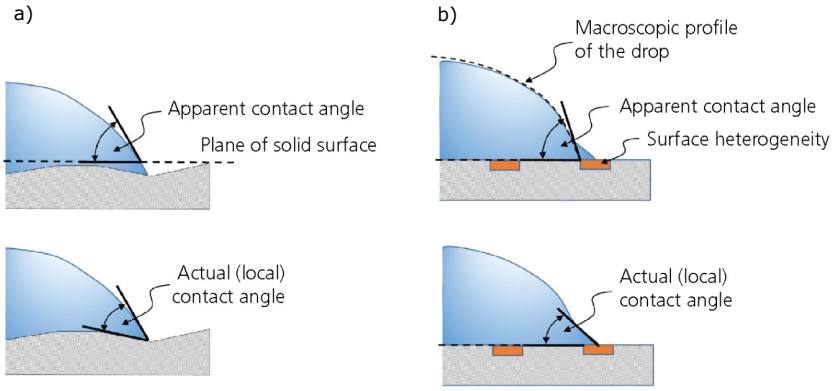

Figure 2.6: Schematic of the pinning effect due to a) roughness and b) chemical heterogeinity, copied from [24].

2.2.3 Roughness Influence on the Contact Angle

The contact angle is a simple, macroscopic quantity that provides microscopic insight to the surface wetting properties. However, there are some difficulties related to this type of measurements. Two of the quantities in Young's equation (equation 2.3), namely γ_{sv} and γ_{sl}, are not physically measurable and therefore Young's equation lack of experimental verification to this date [25].

The interpretation of the contact angles and how it can be used to study the properties of a surface has been discussed since Young first reported the contact angle over two centuries ago [16]. While Young's equation seems simple and only consider the thermodynamic properties of the line between three phases, the contact angle on real surfaces are sensitive to many microscopic factors; physical geometry such as roughness, contamination, and chemical heterogeneity [24]. Physical and chemical heterogeneities can act as pinning sites as they might change the local contact angle, ultimately affecting the global contact angle (as shown in figure 2.6).

Roughness has widely been studied in relation to the contact angles [26, 27, 28, 23]. The root mean square roughness (R_{RMS}) is a quantative tool when discussing roughness and is defined as the standard deviation of the elevation, z values, within the given area,

$$R_{RMS} = \sqrt{\sum_{ij} \frac{(z_{ij} - z_{avg})^2}{N}}, \tag{2.10}$$

where z_{avg} is the avarage of the z value within the given area, z is the value for a given point (i,j), and N is the number of points within the given area.

The threshold for which R_{RMS} value that influences the macroscopic contact angle is unclear. At first, it was suggested that R_{RMS} smaller than 100 nm will not affect contact angle hysteresis [28, 27]. Extrand et al. studied contact angles on surfaces with roughness in the range 0.3 nm -

269 nm, and found that contact angles were not dependent on surface roughness but rather the chemical nature of the surface [29]. In contrast, Delmas et al. [26] recently showed that the minimum defect size necessary to produce a contact angle hysteresis is of molecular dimensions ($\sim$ 1 nm). Other studies suggest that the density of defects and the defect shape influence the pinning effect of the droplet [23]. Sharper surface features might lead to stronger pinning than round-shaped features. In conclusion, the exact influence of surface topography on static contact angles on the nanometric scale is not yet known due to the complexity of the problem [23].

In this thesis work, the static water contact angle (WCA) is studied; that is, the apparent WCA after a sessile water droplet is deposited on a surface. This apparent WCA represents either a metastable equilibrium (local minimum in the Gibbs energy curve) state or the equilibrium state (lowest minimum in the Gibbs energy curve) of the system and lies between the receding and advancing WCA [22]. The static WCA will be analyzed in the light of the physical and chemical heterogeinity of the surface. As such, the WCA is used as a measure for the "ground state" of the oxidized graphene surface. Before every freezing cycle, the WCA was measured. A sudden change in the WCA indicates changes in the surface properties.

2.3 Icing

Ice formation occurs in many different forms of precipitation, such as snow, fog icing, and frost formation. It is in this project focused on ice formation from impinging droplets. That is, when droplets of liquid water come in contact with a surface that is lowered to a subzero temperature, ice nucleation may begin.

2.3.1 The Classical Ice Nucleation Theory

Nucleation is the first step in forming a new thermodynamic phase. The classical nucleation theory uses thermodynamics to describe the rate at which the first steps of the nucleation process occur. The very first step in ice nucleation is that an ice embryo (e.g. an assumed spherical cluster of several water molecules) is formed in the liquid phase, as shown in figure 2.7. In principle, an ice embryo may nucleate either at the interface between droplet and air (homogeneous nucleation) or at the interface between droplet and a foreign body (heterogeneous nucleation). Heterogeneous nucleation is energetically favorable and will, therefore, dominate the nucleation process when a foreign body is present. Pure water in complete dust-free environments can withstand extremely low temperatures before spontaneously freezing (below -40°C) [30].

The rate of nucleation, J, is the number of ice embryos formed per volume·time (units $m^{-3}s^{-1}$). From the classical nucleation theory, it can be shown that the heterogeneous ice nucleation rate,

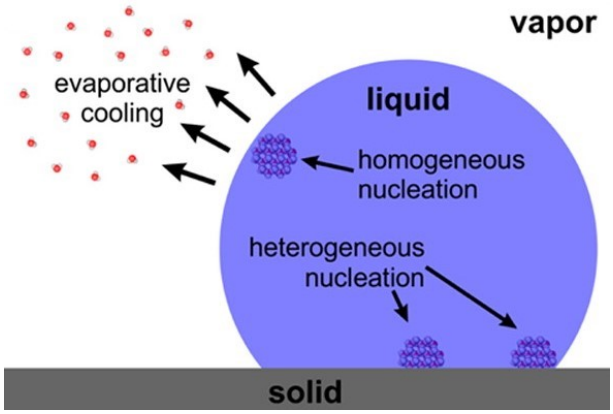

Figure 2.7: Ice embryos in water droplet can either nucleate at the droplet-surface interface (heterogeneous nucleation) or at the droplet-air interface (homogeneous nucleation). The first is strongly energetically favorable. Copied from [31].

J, on a surface can be expressed by the following equation [32, 33]:

$$J(T) = N_s Z w^{(+)} e^{\frac{-\Delta G^*}{kT}}, \tag{2.11}$$

where ΔG^* is the free energy barrier for an ice embryo to form (discussed in section 2.3.2), T is the temperature and k is the Boltzmann constant. The prefactor is a product of three terms, N_s which is the number of the nucleation sites, Zeldovich factor Z, which gives the probability that an ice embryo at the top of the barrier will nucleate to form a new phase rather than dissolve (typically in the order of 10^{-2}), and w^+ which is the rate of impinging molecules into the ice embryo (such that the ice embryo grow).

The impingement rate, $w^{(+)}$ is given by [33]:

$$w^{(+)} = \zeta \frac{k_B T}{d^5 \eta} A \tag{2.12}$$

where ζ is a correction factor (in the order 10^{-3}-10^{-5}), d is the diameter of the ice embryo sphere, η is the liquid viscosity and A is the surface area of the ice embryo. Hence, the kinetic prefactor is inverse proportional to the viscosity of the fluid.

The average nucleation time delay (τ_{av}), is inverse proportional to the nucleation rate, ie. [2]:

$$\tau_{av} = \frac{1}{J(t)}. \tag{2.13}$$

Thus, it is clear from equation 2.11 that in order to delay the icing process, the water-surface contact area should be minimized (so that less heterogeneous nucleation sites N_S are available), higher viscosity at the solid-droplet interface, and that the free energy barrier (ΔG) should be maximized. As will become clear in the following, ΔG can be altered by the contact angle (θ_{IW})

and the surface roughness of the surface (R).

2.3.2 Free Energy Barrier ΔG

Homogeneous Ice Nucleation

From thermodynamics, Gibbs free energy, ΔG, of a nucleus is given by a volume term and a surface term [34]:

$$\Delta G = n\Delta\mu + A\gamma_{IW}, \tag{2.14}$$

where n is the number of particles in the ice embryo, $\Delta\mu$ is the chemical potential between the two phases, A is the surface area of the ice embryo, and γ_{IW} is the ice-water interfacial energy.

For a spherical embryo with radius r, one has $n = 4\pi r_c^3\rho_c/3$, where ρ_c is the particle number density, and $A = 4\pi r^2$, such that equation 2.14 can be written as [34]:

$$\Delta G = \frac{4}{3}\pi r^3\rho_c\Delta\mu + 4\pi r^2\gamma_{IW}. \tag{2.15}$$

The first term is the volume term where $\Delta\mu$ is always negative. The second term is surface-area term, where γ_{IW} is the ice-water interfacial energy which is always positive.

ΔG is plotted in figure 2.8. From the plot, it is evident that surface term dominates for a small radius, whereas the bulk term dominates for a larger radius. At an intermediate value of r, ΔG reach a maximum, ie. a critical ice embryo size with maximum energy [35]:

$$[\frac{dG}{dr}] = 0, \rightarrow r_c = \frac{2\gamma_{IW}}{\Delta\mu}. \tag{2.16}$$

After the ice embryo has passed the critical radius, ΔG becomes more negative and the growth of the ice embryo becomes highly favorable and eventually leads to a solidification of the whole droplet. Thus, r_c represents the minimum size of a stable ice embryo.

The free energy barrier an ice embryo must overcome to nucleate, is obtained by substituting equation 2.16 into equation 2.14:

$$\Delta G^*_{hom} = \frac{16\pi\gamma_{IW}^3}{3(\Delta\mu)^2} \tag{2.17}$$

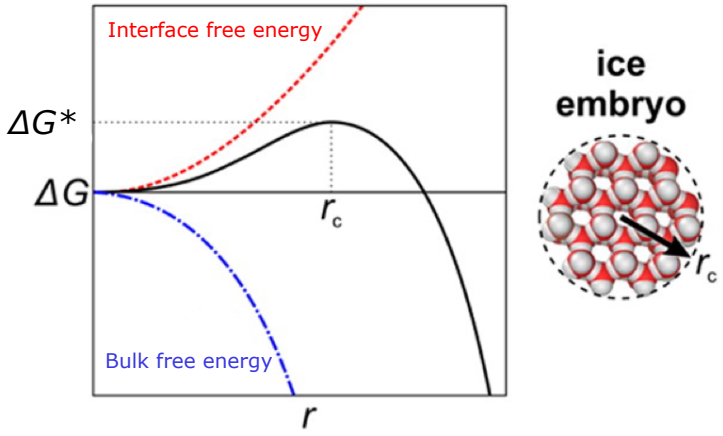

Figure 2.8: A plot of gibbs free energy (black curve) versus radius of embryo. Blue curve is the bulk free energy (first term in equation 2.14) and red curve is the interface free energy (second term in equation 2.14). An ice embryo of critical size r_c is shown as the inset. Illustration copied and modified from [9].

Heterogeneous Ice Nucleation

In homogeneous nucleation, the surface area is approximately a sphere. In heterogeneous nucleation, however, the surface area is always smaller than that of a sphere since part of the nucleus boundary is accommodated by the surface (or a foreign body). Therefore, by equation 2.14, the heterogeneous free energy barrier is always lower than the homogeneous free energy barrier, such that nucleation is always promoted by the presence of foreign bodies (surface, dust, etc.).

The expression for the free energy of ice embryo formation on a surface can be expressed as [35]:

$$\Delta G^*_{het} = f(\theta)\Delta G^*_{hom}, \tag{2.18}$$

where $f(m,x)$ indicates how much the nucleation barrier is reduced with the effect of the foreign body. $f(m,x)$ is dependent on the parameter $m = cos\theta_{IW} = (\gamma_{SW} - \gamma_{SI})/\gamma_{WI}$ where θ_{WI} is the contact angle of the ice-embryo, and γ_{SW}, γ_{SI}, and γ_{WI} denotes energy of solid-water, solid-ice and water-ice respectively. Also, $f(m,x)$ is dependent on the parameter $x = R/r_c$ where R is the surface roughness radius and the critical ice embryo radius (r_c).

Fletcher et al. [36] derived $f(m,x)$ for convex surfaces:

$$f(m,x) = \frac{1}{2}\left\{1 + (\frac{1-mx}{w_v})^3 + x^3\left[2 - 3(\frac{x-m}{w_v}) + (\frac{x-m}{w_v})^3\right] + 3mx^2(\frac{x-m}{w_v} - 1)\right\} \tag{2.19}$$
$$w_v = (1 + x^2 - 2xm)^{1/2}$$

and for concave surfaces,

$$f(m,x) = \frac{1}{2}\left\{1 - (\frac{1+mx}{w_c})^3 + x^3\left[2 - 3(\frac{x+m}{w_c}) + (\frac{x+m}{w_c})^3\right] + 3mx^2(\frac{x+m}{w_c} - 1)\right\} \tag{2.20}$$
$$w_c = (1 + x^2 + 2xm)^{1/2}$$

Hence, there are mainly two factors that affect the correlation factor $f(m,x)$; namely m related to interfacial energy (the contact angle θ) and x related to the substrate roughness (R).

2.3.3 Surface Roughness and Quasi-Liquid Effect

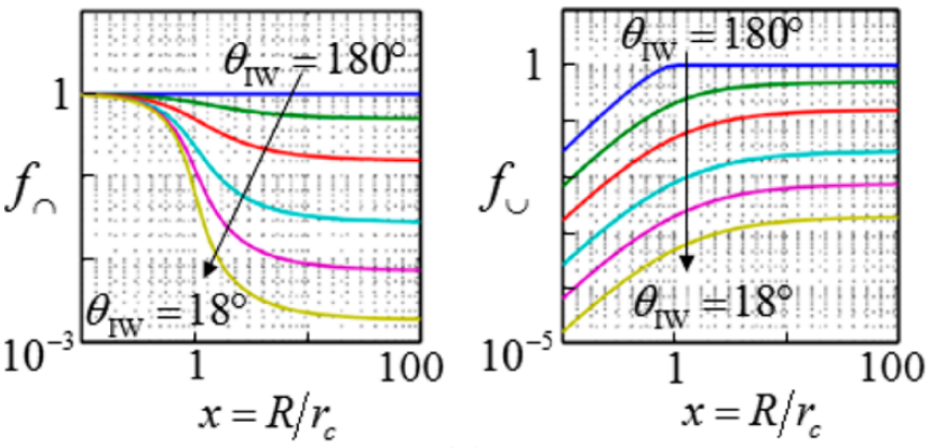

Figure 2.9: The geometrical factor f is plotted against the ratio $x = R/r_c$ for a) convex roughness and b) concave roughness for varying values of θ (180, 90, 60, 36.9, 25.8 and 18.2°). Plot copied from [9] and modified by [31].

In figure 2.9, $f(m,x)$ is plotted versus x = R/r_c for convex (nanobumps) and concave (nanopits) surfaces, where each curve represent different contact angles of the ice embryo. It is evident that f is only affected when x < 10, that is when $R < 10r_c$. Furthermore, equation 2.18 shows that ΔG^*_{het} is proportional to the geometric factor f. Hence, when $R < 10r_c$, convex nanobumps increase ΔG and thereby suppress ice nucleation, whereas concave nanopits decrease ΔG and thereby promote ice nucleation. Since concave nanobumps is an inevitable byproduct of making nanobumps, all nanotextured surface would, according to classical nucleation theory, promote ice nucleation.

Experimental observations, however, have shown the opposite: that nanotextured surfaces suppress ice nucleation [9]. The previous work on the icephobic properties of fluorinated graphene presented by the Bergen group is another example of this [37]. As will be shown in chapter 6, this thesis work also shows that nanotexture does not necessarily promote ice nucleation. To understand the discrepancy between the theoretical prediction and the experimental results, one can look at the liquid-surface interaction.

Recent theory suggests that anti-icing surfaces have a liquid layer on the ice-solid and ice-vapor interface at temperatures lower than the freezing temperature [38, 9]. This layer is often referred to as a quasi-liquid layer and is illustrated in figure 2.10. The height of the quasi-liquid layer is predicted to be a few atomic layers [31]. In the existence of such quasi-liquid layer between an ice nucleus and the surface, both the thickness of the quasi-liquid layer and θ_{IW} will increase with decreasing R [9], directly affecting the nucleation rate. Additionally, the entropy is suggested to be reduced in the presence of a water layer [10]. It has been demonstrated that the viscosity of the interfacial liquid layer might dominate the nucleation rate [39], and that the viscosity on hydrophilic surfaces is shown to be several orders of magnitude higher than on hydrophobic surfaces [40]. Hence, the existence of a quasi-liquid layer may counteract the theoretical enhanced nucleation effect of nanopits.

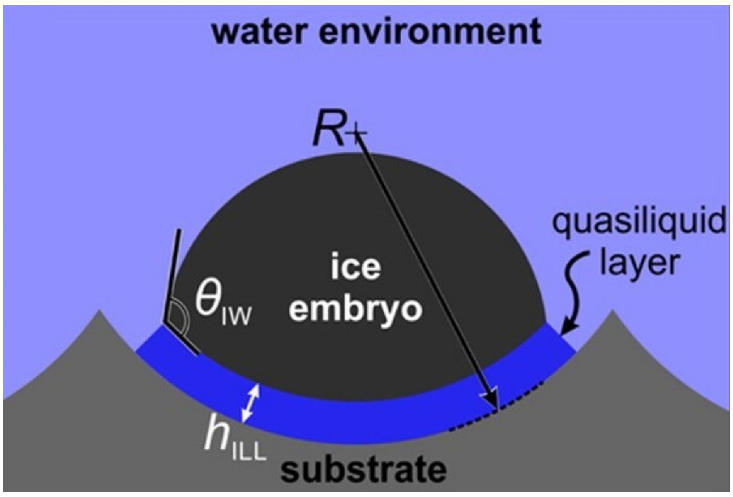

Figure 2.10: Showing the quasi-liquid effect at a curved surface. Image copied from [31].

2.3.4 Freezing Process of a Water Droplet

The freezing process is reported to occur in two stages [10]. In the first stage, after the very first ice embryo is formed, the droplet heats up adiabatically, resulting in a mixed liquid/ice phase. This is evident as a loss of water clarity (visible in the middle panel of figure 2.11) and is the *freezing onset*, that is, the start of the freezing process. This stage is rapid and only lasts a couple of milliseconds. In the second stage of freezing, the ice front moves upwards and forms a

pointy-tip-shaped ice droplet (right panel of figure 2.11). The process occurs isothermally, and heat is now released to the substrate by conduction.

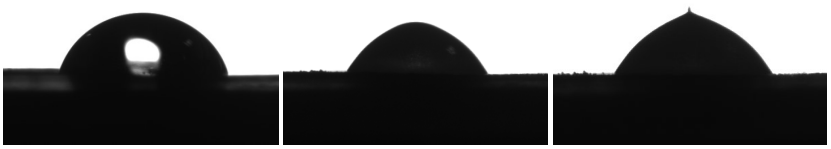

Figure 2.11: Water droplet at room temperature (left), at the freezing onset (middle) and the droplet in frozen state (right).

2.4 The Relation of Icephobicity to Wettability

Superhydrophobic surfaces exhibit some surface properties that might be desirable to delay ice formation. A droplet sitting in the Cassie-Baxter state will have reduced solid-contact area and therefore fewer heterogeneous nucleation sites (N_S) and increase the free energy barrier (ΔG) because of high contact angle (θ), directly leading to lower nucleation rate (J) from equation 2.11. During the last decade, an extensive amount of research has been done in order to study the relation of icephobic surfaces to superhydrophobific surfaces. The results are conflicting. Superhydrophobic surfaces are under certain conditions considered to have icephobic properties for three reasons, which will be discussed separately in the following.

2.4.1 The Bouncing Effect

Superhydrophobic surfaces have the ability to shed of impacting droplets, because of their extremely low contact angle hysteresis [41]. Impacting droplets might bead up an bounce off the surface before ice nucleation takes place. Mishchenko et al. found that highly ordered superhydrophobic surfaces were able to repel impinging water droplets before freezing at temperatures down to $-25°C$, whereas ice nucleation was observed for both hydrophilic and hydrophobic surfaces at low humidity ($< 5\%$) [42].

However, there are several challenges of using the bouncing-droplet method alone to prevent ice formation on a surface. Bahadur et al. developed a theoretical ice-formation model that suggests that impacting droplets create an ice embryo at the tips of the bumps of the superhydrophobic surface, which will increase the hydrophilicity of the surface [43]. The surface ability to repel water droplets decreases with time under freezing conditions. If the droplet-surface contact time

is long enough, droplets will contract, pin, and freeze at their positions, eventually leading to ice formation.

If impacting droplets have enough kinetic energies, they might displace the air pockets of the superhydrophobic surface, which will lead to transit from the Cassie state to the Wenzel state. In the Wenzel state, the surface-droplet contact area increases and the droplet exhibit lower mobility, which ultimately favors ice to nucleate according to the nucleation theory. Some researchers have focused on methods to make the Cassie state more robust in order to prevent transition to the Wenzel state or to engineer surfaces where the reversible transition is possible [44], but this is in general proven to be challenging.

Although the bouncing hypothesis is shown to work in relatively dry environments, superhydrophobic surfaces are not believed to have the same properties in harsh environmental circumstances. The bouncing effect is vulnerable at high humidities, where condensation and frost will be other unavoidable factors to account for. In high humidity, the wettability of superhydrophobic surfaces are observed to increase [45, 46], lowering the probability of bouncing droplets. Hence, one can conclude that in environments with high humidity, or at surface temperatures below the dew point, the droplet-bouncing approach alone will be ineffective [47]. The surfaces used in this thesis were not found to be superhydrophobic, and thus the bouncing effect is not of relevance here.

2.4.2 Nucleation Temperature and Freezing Delay

Alizadeh et al. [48] reported that microstructured superhydrophobic surfaces showed two orders of magnitude longer freezing delays than hydrophilic surfaces with surface temperatures of $-20°C$. They argued that a combination of reduced heat transfer efficiency, smaller droplet-surface contact area, and increased energy barrier leads to the observed icephobic benefits. In their study, once reaching the freezing onset temperature, the droplet froze within seconds. It was suggested that the dominant factor beneath the freezing onset temperature was the homogeneous (droplet-bulk and droplet-air) nucleation rate that dominated [48]. Moreover, Shen et al., found that freezing delay time increased with contact angle independent of the cooling temperature down to $-30°C$ [49].

In contrast, Jung et al. reported that the hydrophilic surface with low roughness (1.4 nm - 6 nm) exhibited the highest freezing delay, followed by hydrophobic surfaces with similar roughness, microstructured superhydrophobic surfaces and finally hydrophilic microstructured surfaces [10]. Other studies were done by Heydari et al. and Yin et al., using 40% and 80% humidity respectively, showed no or limited correlation between wettability and ice formation [45, 50].

Li et al. showed that hydrophilic surfaces can exhibit longer freezing delay than hydrophobic

surfaces [39], owing to the enhanced viscosity of the interfacial layer, leading to a higher energy barrier ΔG. Moreover, it was reported that the viscosity of the interfacial water is orders of magnitude higher than on interfacial water on hydrophobic surfaces [40]. This finding has later been supported by studying functionalized groups on graphene using molecular dynamic simulations [51]. In general, several studies have shown that ice nucleation may be dictated more strongly of surface roughness than wettability itself [51].

The discrepancy observed in literature can be explained mainly for two reasons. First, it is suggested that nucleation is more influenced by surface roughness than wettability properties. Second, long freezing delays on superhydrophobic surfaces have only been observed in low humidity conditions (5%). At higher humidities, surfaces are more susceptible to condensation and frost formation, and droplets will more readily transit from the Cassie-Baxter state to the Wenzel state. In fact, Varansi et al. verified in 2010 that superhydrophobic surfaces susceptible to frost formation become significantly more ice friendly [52], explained by the Cassie-Baxter to Wenzel transition of the water-ice droplet.

2.4.3 Ice Adhesion Strength

The interaction of ice with solids can be attributed to van der Waals forces and electrostatic interactions. To investigate ice adhesion on different surfaces, again one looks to the Cassie-Baxter and Wenzel droplet state. Because of the lower mobility of the droplet in the Wenzel state, the droplet obtains higher ice adhesion when frozen.

Two different ice growth modes of ice crystals were recently reported to depend on the wettability of a surface [53]. Along-surface growth mode was observed for hydrophilic surfaces, whereas an off-surface growth mode was observed for hydrophobic surfaces, both visible in figure 2.12. The paper attributed this finding to a bilayer that can form on hydrophilic surfaces, which can dictate the along-surface growth mode. In detail, they located the critical contact angle, $\theta = 38.5^\circ \pm 1.6^\circ$, of where this bilayer formed. They proved that off-surface growth had lower ice adhesion, as it could be removed by wind (velocity = 5.8 m$\cdot$ s^{-1}, temperature = -3°C), while the along-side surface growth was not removed. Ice adhesion was not investigated in this thesis work.

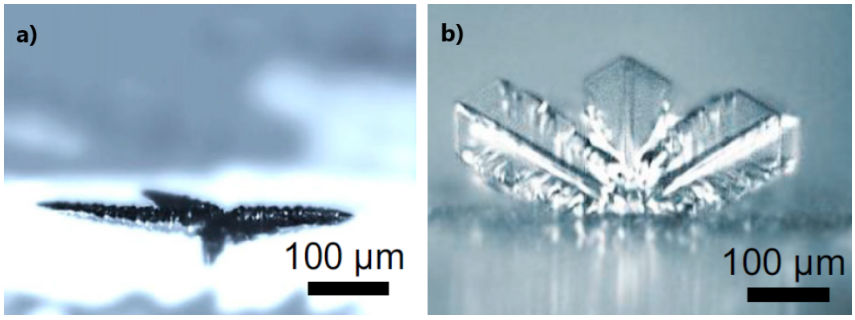

Figure 2.12: Images of ice crystals showing a) along-side growth mode and b) off-side growth mode. Copied from [53].

2.5 Summary

The contact angle is a macroscopic measurement of the microscopic properties of a surface and provides inverse information on the wettability of a surface. Micrometer and possibly even nanometre surface features might pin the water droplet, thus creating metastable contact angles of the system. In this thesis work, the static water contact angle (WCA) is measured, which is the stable or metastable contact angle of the system.

From the classical nucleation theory, it is seen that to prevent ice formation, one should minimize the droplet-surface contact area to minimize available nucleation sites (N_S) and maximize the free energy barrier (ΔG^*_{het}) by applying surface roughness. It has been suggested that there exists an interfacial water layer between the droplet and the surface, which enhances the icephobic properties.

Superhydrophobic surfaces have many of the desired qualities (minimized contact area and surface roughness). Experimentally, they have shown superior icephobic properties in specific laboratory conditions, that is low humidity ($< 5\%$), but they have not yet shown to keep their icephobic behaviors in higher humidities [45, 50], which is crucial in order to use surfaces under outdoor conditions. Several studies indicate that superhydrophobic surfaces are not always icephobic, and that icephobicity is rather dominated by the roughness of the surface [51].

Chapter 3

The wetting and icing properties of functionalized graphene; a brief overview

The extreme lightweight and transparency of graphene make it an ideal material for coatings. Oxidized graphene is predicted to have superior icephobic properties. This chapter starts by presenting a brief overview of the growth procedures used and the resulting structures of graphene on metals, before looking at oxygen-functionalized graphene. The chapter ends with discussing the wetting and icephobic properties of graphene and functionalized graphene.

3.1 Structure

Graphene (or "2D graphite") has been studied theoretically for seventy years [54], although it was long believed that a 2D layer of graphite would be physically unstable. However, in 2004, the academic model turned into reality when Geim and Novoselov managed to isolate, characterize, and identify single-layer graphene from graphite with regular adhesive tape [55]. Since then, the exceptional physical properties of graphene, such as high electric conductivity [56], excellent mechanical strength [57], optical transparency [58] and more have been exploited, leading Geim and Novoselov to win the Nobel Prize in Physics in 2010.

Graphene is a two-dimensional layer of carbon atoms arranged in a hexagonal pattern as shown in figure 3.1. The graphene unit cell consists of two carbon atoms, each atom contributes four valence electrons, which gives a total of eight valence electrons per unit cell. The carbon atoms are bonded in the plane of graphene layer, where each carbon atom has three sp^2 bonds to neighboring carbon atoms with 120° between each band. The remaining p_z orbital is oriented perpendicular to the sp^2-plane and contributes one electron to a delocalized bonding orbital distributed over the entire graphene sheet [59]. The length of the carbon bonds is δ = 1.42 Å

[60]. The two primitive unit vectors, a_1 and a_2, illustrated in figure 3.1, are described by:

$$a_1 = \frac{\delta}{2}(3, -\sqrt{3}), a_2 = \frac{\delta}{2}(3, \sqrt{3}) \tag{3.1}$$

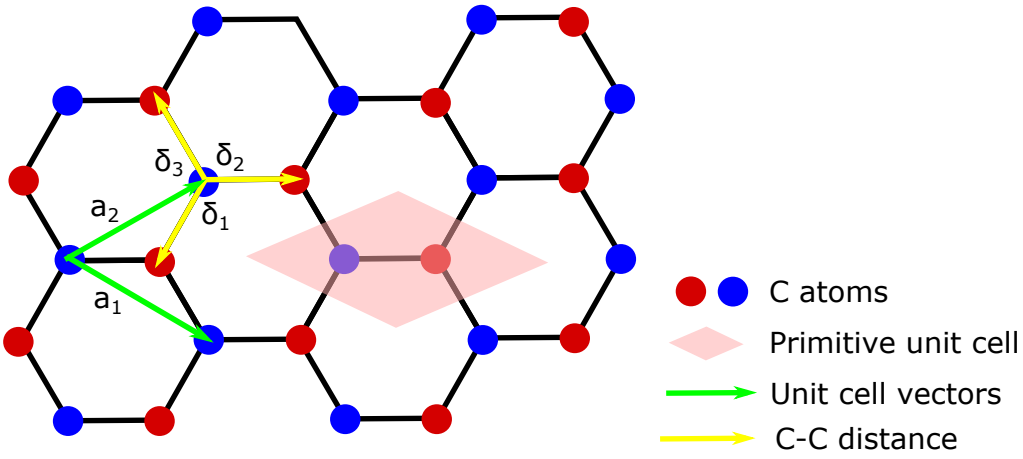

Figure 3.1: Atomic structure of graphene, where the lattice vectors a_1, a_2 as well as the nearest-neighbor vectors, δ_1, δ_2, and δ_3 are shown.

A scanning tunneling microscopy image of graphene on Ir(111) (technique discussed in section 4.1) is shown in figure 3.2. Here, the small hexagonal so-called honeycomb pattern is the graphene. The unit cell of graphene is marked by the white rhombus. The bigger hexagonal pattern shows a moiré superstructure and will be discussed in section 3.2.1.

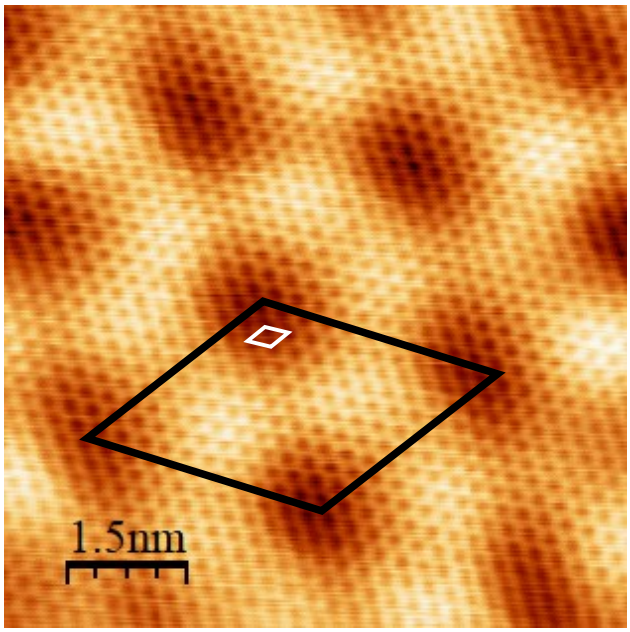

Figure 3.2: STM image of Gr/Ir(111). White rhombus: graphene unit cell. Black rhombus: moiré unit cell. Scanning parameters: It: 940 pA, Vt: 7.6 mV.

3.2 Graphene Growth

The method used by Geim and Novoselov for isolating graphene was to exfoliate a single graphene layer from highly oriented pyrolytic graphite (HOPG) using regular adhesive tape (shown in figure 3.3). However, Geim and Noveselov only managed to separate micrometer flakes of graphene. Due to their small size and the uncontrollable preparation procedure, the mechanical exfoliation of graphite into graphene is not suitable for use in many technological processes where the properties of graphene are desirable, such as for solar cells [61], corrosion coatings [62] and icephobic coatings [37].

Chemical vapor deposition (CVD) is a popular method to prepare graphene, because it allows for the production of high-quality, large areas of single-layer graphene. In the CVD process, a heated metal surface gets exposed to a gas of hydrocarbons, as shown in figure 3.4. The decomposition of hydrocarbons takes place immediately upon adsorption on the hot metal, so the C atoms migrate towards other C atoms to form graphene islands. Typically, several grains of graphene are formed and areas where these grains merge, are called grain boundaries [73]. The orientation of each grain strongly depends on the hot metal temperature [64]. During cooling of the substrate, the metal contracts more than graphene leading to excess areas of graphene, and thereby wrinkles are formed [65]. Wrinkles are typically present in graphene on Ir(111) with spacing in the order of micrometers and with amplitudes in the order of nanometers [66]. The

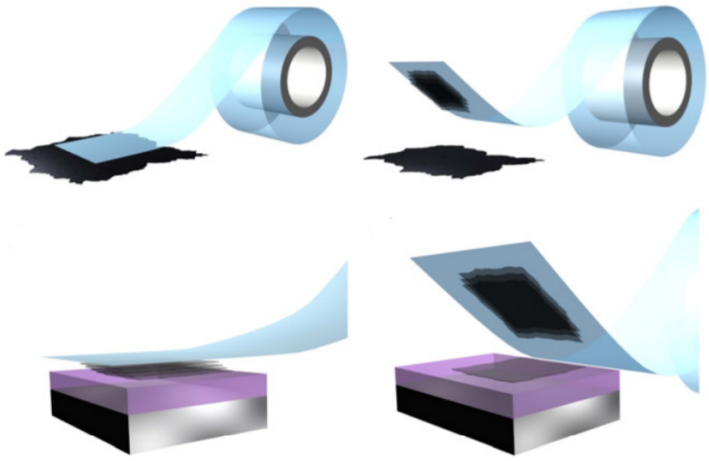

Figure 3.3: a) Mechanical exfoliation of graphene using regular scotch tape. Copied from [63].

corrugation (convolution between geometrical roughness and electronic structure) of wrinkled areas are calculated in section 6.3.

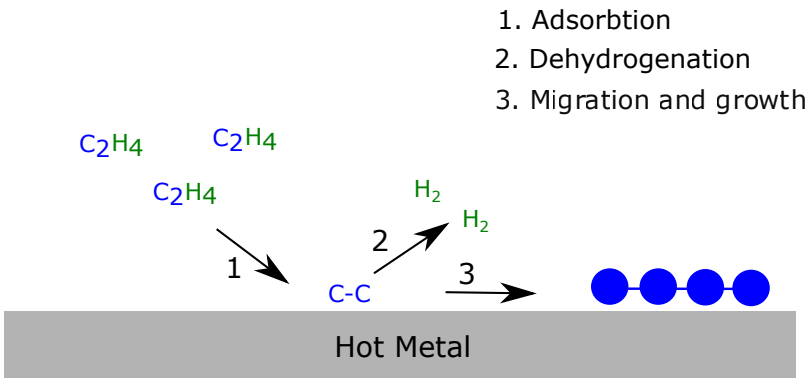

Figure 3.4: Schematic illustration of graphene growth on hot metal.

The CVD method can be combined with transfer methods to allow for graphene transfer up to meter sizes. The roll-to-roll method, shown in figure 3.5, has shown huge potential for this purpose [67, 68]. There are three main steps in this procedure: i) the adhesion of polymer supports to the graphene on the metal foil, ii) etching of the metal layers so that graphene gets supported by the polymer, and finally; iii) release of the polymer support so that the graphene

is now supported by the target [67]. Hence, large-scale areas of CVD grown graphene can be transferred to the desired substrate via the roll-to-roll method, which is necessary for several industrial purposes.

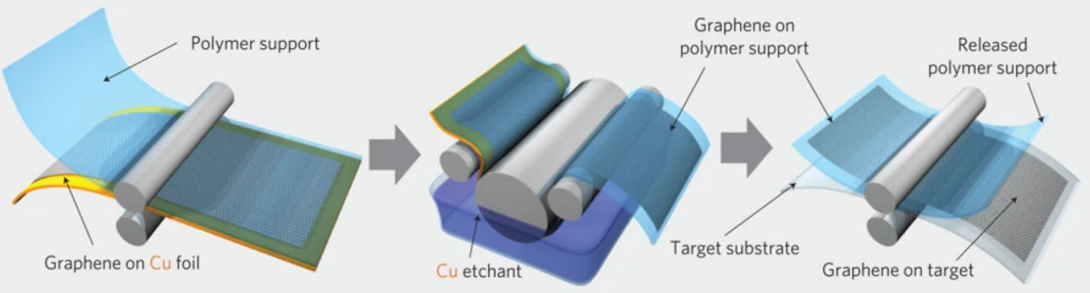

Figure 3.5: A schematic illustration of the roll-to-roll process. Here copper foil is used as the metal substrate before transfer. Copied from [67].

3.2.1 Moiré Superstructure

When a layer of graphene is grown on top of a metal surface, the underlying metal and the graphene monolayer do not have identical lattice parameters. This gives rise to a moiré superstructure, an example of which is visible in figure 3.2. The periodicity of the superstructure depends on the angle of rotation between the metal and graphene unit cells and on the difference in lattice constants between graphene and the surface atoms in the metal. In the simplest case, where the lattice vectors of both sublattices are parallel to each other, carbon atoms can sit on three different types of distinct locations relative to the underlying lattice and on intermediate positions in between. This is illustrated figure 3.6, where a cell of 10x10 graphene lattice (yellow balls) on top 9x9 Ir(111) (green balls) atoms is shown. In the corners of the supercell, the top Ir(111) surface atom sits directly underneath the center of the hexagon of the graphene. Two carbon atoms sit directly above the second and third layers of Ir atoms respectively. These sites are marked (2-3) in the figure and are referred to as ATOP sites in literature. Other environments occur where two carbon atoms sit above the first and third layer of the Ir surface atoms (1,3) referred to as HCP sites, or first and second layer of Ir surface atoms (1,2) referred to as FCC sites.

These different environments may give rise to maxima and minima in the tunneling current, leading to the superstructure observed in STM images. The image parameters used and the state of the tip will dictate the image contrast [69]. In figure 3.2, dark areas can be assigned to ATOP sites whereas bright areas can be assigned to FCC/HCP sites [69]. The different environments also change the chemistry of the carbon atom. HCP and FCC carbon atoms have shown to be more reactive [70, 71, 8].

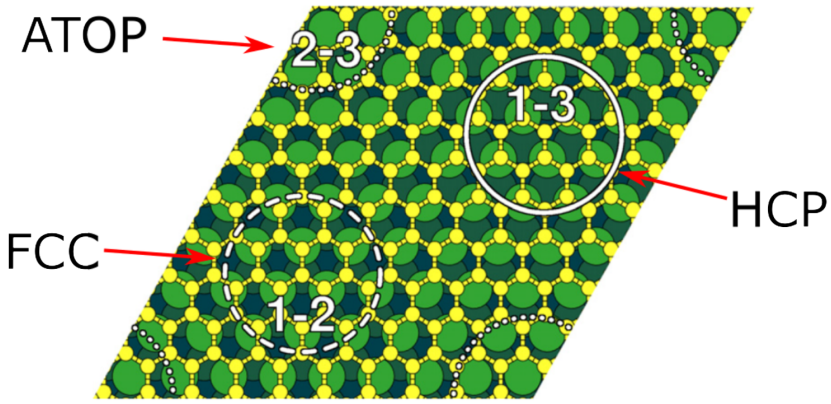

Figure 3.6: A 10x10 graphene lattice (yeelow balls) on top of 9x9 Ir(111) (green balls). Different chemical environments in the supercell are marked: ATOP, FCC and HCP sites. Copied and modified from [72].

3.2.2 Structural Defects in Graphene

Structural defects and impurities in graphene may appear during growth a processes (oxidation, exposure to air, etc.) [73]. Defects will increase its chemical reactivity [74], and can alter the electronic [75] and mechanical [76] properties of the surface significantly. Impurities are therefore important to consider and can be grouped into so-called point defects and line defects.

Point defects arise if there are missing or existing additional atoms in the hexagonal structure. When atoms are missing, the defects are called vacancies [73]. Figure 3.7a) shows an example of where one atom is missing, resulting in the formation of pent- and nontagonal rings. Another type of point defect is adatoms, where a foreign atom binds out-of-plane. The atom may sit in a bridge-like configuration, as shown in figure 3.7b. Other adatoms configurations are also possible and will be discussed in section 3.3.

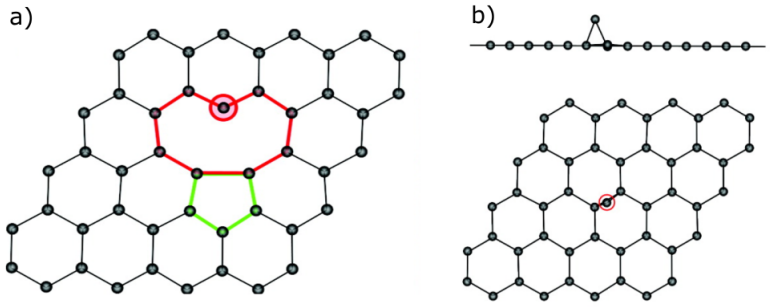

Figure 3.7: Two examples of point defects. a) Vacancy: one atom is missing, so that non-hexagonal rings are formed. b) Adatom in the epoxy configuration is shown. Illustration from [73].

Furthermore, defects can be found along lines in samples. The most common type is called grain boundaries and exists where two domains of graphene merge [73]. Due to the small differences

in orientation of the domains, lines of pent- and heptagonal carbon rings are formed. Two examples are shown in figure 3.8. In particular, this type of defect is common when using the CVD method to grow graphene.

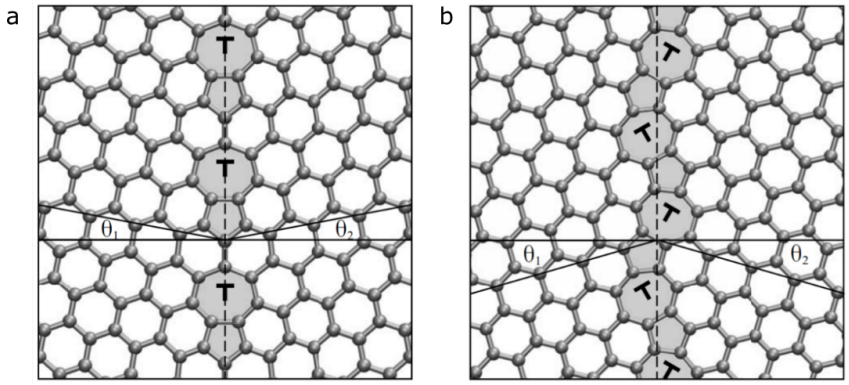

Figure 3.8: (a,b) Line defects arised because two graphene domain merge, called grain boundaries. Dashed lines denote the grain boundary line. Illustration from [77]

3.3 Functionalization of Graphene with Oxygen

Oxygen-functionalized graphene is one of the most common graphene derivatives and was synthesized for the first time by exposing graphite to strong acids by Brodie in 1859 [78]. Currently, graphene oxide is usually chemically produced by the Hummers method. Graphene oxide has been successfully made into fibers [79], membranes [80], papers [81] and free-standing multilayered films [82], and it can be drop-casted onto various substrates [83]. The potential applications of graphene oxide include energy storage[3], water treatment [4], sensors[5] and protective coatings[6].

Another route to oxygen-functionalized graphene is the exposure of CVD grown graphene supported by a metal substrate to oxygen atoms in ultra-high vacuum [8, 84]. In this thesis, the therm *graphene oxide* refers to as materials prepared in solution, and the therm *oxidized graphene* refers to supported graphene exposed to oxygen atoms under controlled conditions.

An overview of different functional groups to expect on graphene exposed to atomic oxygen is shown in figure 3.9. Until recently, it was generally agreed that atomic oxygen would form epoxy groups on the basal plane of graphene on metals [84, 85]. Epoxy groups are oxygen atoms that interact with two adjacent carbon atoms (1,2-ether) in the form of a bridge configuration. However, a more stable functional group has recently been investigated; namely the enolate group. Enolate groups are formed when oxygen atoms become polarized upon adsorption and binds on-top of carbon atoms, where the adjacent carbon atom bind to an underlying metal atom. This mechanism was first proposed theoretically [86], followed by experimental evidences using

a Ru(0001) [87] and Ir(111) [8] as metal substrates.

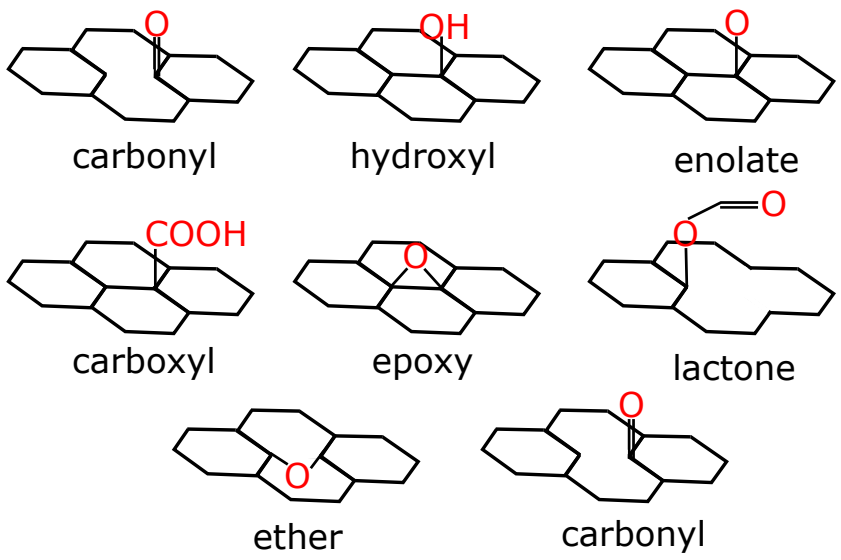

Figure 3.9: Various functional groups in oxygen-functionalized graphene. Illustration assisted by Ranveig Flatabø and Andrew Cassidy. Used with permission.

3.3.1 Functionalization of Graphene with Oxygen on Ir(111)

Graphene can be grown on Ir(111) by the CVD method (see section 3.2 for details) producing highly oriented domains and a low concentration of defects [69]. Graphene interacts weakly with the Ir(111) surface atoms [72] compared to other metals (such as Ru, Ni) making such graphene quasi-free-standing [88].

The lattice constant for graphene is 2.46 Å, while the lattice constant for the surface atoms on the Ir(111) surface it is 2.73 Å, leading to a lattice mismatch of 10%. This gives rise to a moiré superstructure with a periodicity of 2.53 nm [69] as described in section 3.2.1. Figure 3.2 shows an area of defect-free graphene grown on Ir(111). The graphene atoms are visible and the unit cell is shown as a white rhombus. The larger pattern is the moiré superstructure that arises from the lattice mismatch between graphene and Ir(111), and the moiré unit cell is shown with a black rhombus. The dark areas correspond to ATOP sites of the moiré superstructure, whereas the brighter areas correspond to FCC/HCP sites. The main reactive sites in the Gr/Ir(111) moiré superstructure are at the FCC/HCP regions. This was first shown by Ir clusters [70], then hydrogen atoms [71] and finally enolate groups [8].

The main functional group expected on oxidized graphene on Ir(111) is the enolate group [8], which the configuration is only possible in FCC/HCP regions. This is because FCC/HCP sites are areas where every second carbon atom sits above an Ir(111) surface atom. As such, when an oxygen atom binds to a carbon atom, the adjacent carbon atom can bind to the underlying

Ir(111) metal. In ATOP sites, where no carbon atom sits directly above Ir(111) atom (of the top layer), the configuration of enolate groups is not possible.

When exposing Gr/Ir(111) to O2, intercalation of oxygen atoms (Gr/O/Ir(111)) in an ultra-high vacuum has been observed, both for an incomplete monolayer of graphene [84] and for a full monolayer of graphene with a substrate temperature of 500 K [89]. Little research has been done on i) possible intercalation of O-Gr/Ir(111) surface in air and ii) the stability of functional groups of oxygen in the air.

3.4 Wettability of Graphene

The wetting properties of a surface are directly dependent on the surface energy and can be measured through the WCA of a droplet deposited on the surface. The definition of surface energy (see section 2.2) does not apply for graphene because it, as a 2D material, does not have a bulk phase. Thus, the surface energy of graphene is strongly dependent on what it is supported by (often a substrate). Even when the graphene is so-called free-standing, whatever is on the other side of graphene (air, vacuum, etc.) will still affect the surface energy [90].

A large spread of WCA is reported in the literature, ranging from 10° when supported on water, to 33° when supported by silicon [91], to 86° on copper, and 127° for isolated graphene (free-standing) [92, 93]. To explain these discrepancies, Belyaeva and Schneider argued in a recent review [90] that three main factors dictate the wetting properties of graphene: i) intrinsic properties of graphene (dictated solely by pristine and isolated graphene) ii) substrate and iii) environmental effects (production and transfer, air, humidity, etc.) of graphene, as briefly illustrated in figure 3.10.

There is an ongoing discussion to what degree the substrate dictates the wetting properties of graphene. The wetting properties of graphene have been proposed to be fully transparent to silicon, copper, and silicon but not silicon dioxide [91], partially transparent to silicon, silicon dioxide and aluminium oxide [94], as well as fully opaque on copper, silica and silicon dioxide [95].

Environmental factors such as the growth conditions and adsorption are important to consider. Small differences in temperatures and pressures used during growth or transfer will result in unavoidable different densities of point and line defects and wrinkles on the sample, which can further influence the wettability of the surface. Le et al. recently showed that intentionally wrinkled and defected graphene have slightly higher WCA than CVD grown graphene [96]. Furthermore, adsorption of different airborne hydrocarbons is reported to increase the WCA of graphene significantly after only 15 minutes of air exposure [97]. The WCA on graphene under

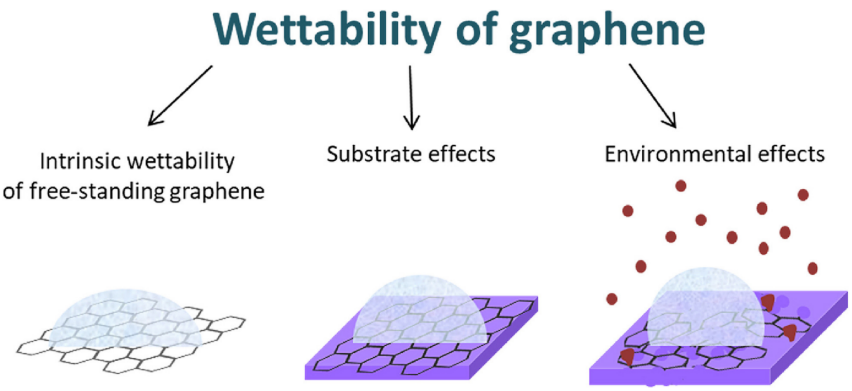

Figure 3.10: An illustration of three main factors that dictate the wetting properties of graphene. Reprinted from [90].

air exposure is observed to increase until a maximum of 92° - 98° is reached [98].

The study of the intrinsic properties of graphene has proven to be complicated for two reasons; one is that current methods can only produce few square micrometers of free-standing graphene, which is too small for any microlitre droplet, and the other is that graphene will be prone to air contaminants immediately after air exposure which in turn will increase the measured WCA. Theoretical molecular dynamic simulations have predicted to be highly dependent on the choice of graphene and water interaction model, as WCA ranging from 45.7° ± 1.3° [99] to 127° [93] have been reported. Recently, Prydatko et al. used a so-called captive bubble method, to find that graphene is hydrophilic and obtained a WCA of 42° [100]. The captive bubble method is the WCA of an air bubble underneath graphene immersed in water, as shown in figure 3.11, and allows the measurement of almost free-standing graphene without the presence of hydrocarbons.

In summary, the wettability of graphene is a sum of the contribution of the intrinsic properties of graphene and the two media on each side; namely substrate effects and environmental effects. The simplified model of WCA (discussed in section 2.2) seems to not be adequate to describe the phenomena occurring when depositing a droplet on graphene (and other 2D materials.)

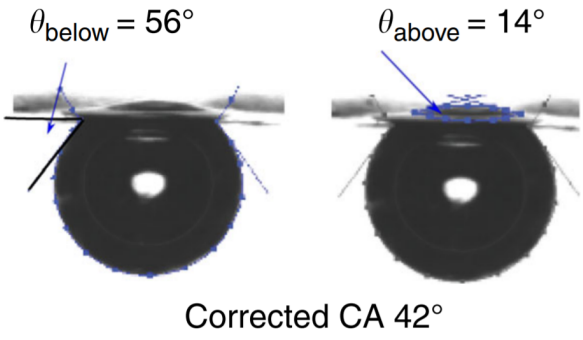

Figure 3.11: Illustration of the captive bubble method. Copied from [100].

3.5 Wettability of Functionalized Graphene

The functionalization of graphene can alter the chemical potential of the surface, which will influence the wetting properties of the surface. Zhang and Chen [51] predicted that graphene functionalized with sodium ions, chloride ions, or methane molecules should have higher wettability than pure graphene. Functionalization with methane molecules was predicted to produce lower wettability than functionalization with sodium or chloride ions, and the wettability decreased with increasing concentration of methane molecules. The results were achieved using molecular dynamics simulations. Recently, functionalization with fluorine was reported experimentally to increase the hydrophobicity of graphene [37]. The result was explained by a reduction in the surface energy after fluorination. Thus, the change of wettability strongly depends on the functional groups.

Graphene oxide is hydrophilic with a reported WCA in the range $\sim 25^\circ$ - 55° [101, 102, 103, 104], with carboxyl- and hydroxyl groups considered to be the main hydrophilic groups. Rasuli et al. [105] showed experimentally that by removing carboxyl groups (by the use of non-thermal effects of microwave radiation) the WCA of graphene oxide increased from 29° to 70°. Zhang et al.,[103] found that UV irradiation of graphene oxide thin films induced an increase in the WCA from 27.3° to 57.6°. They attributed this change to the removal of hydroxyl- and carbonyl groups. Wei et al. [101] used molecular simulations to theoretically predict that graphene oxide is hydrophilic, and the hydrophilicity increases with an increased oxygen concentration. They found that with an oxygen concentration (the number of oxygen atoms over the number of carbon atoms) of 20 %, the WCA could be as low as 26.8°. Little research has been done on the wetting properties of CVD grown graphene with exposure to atomic oxygen, ie. oxidized graphene, which is the topic of this project.

3.6 Graphene as an Icephobic Coating

Recently, Li et al. [96] showed experimentally that intentionally wrinkled graphene had remarkable anti-icing properties. They reported a freezing delay of 1.25 h at -15°C or 2.8 h at -10°C. Wrinkles are an unavoidable product of CVD-grown graphene (discussed in more detail in section 3.2) and might contribute positively to the icephobic properties of any CVD-grown graphene-based coating.

Akthar et al. reported that the freezing onset temperature of graphene supported by sapphire was -18°C $\pm$ 1°C [37], lower than the -15°C $\pm$ 1°C reported from the bare sapphire substrate. However, as in another study [51], the icing properties of graphene are shadowed by the reported extraordinary icephobic properties of functionalized graphene.

3.7 Functionalized Graphene as an Icephobic Coating

Functionalized graphene has been predicted to have outstanding icephobic properties [37]. Among others, Zokaie and Foroutan calculated the freezing onset temperature for water confined between two sheets of graphene oxide to be -37°C [106]. The graphene sheets contained hydroxyl and epoxide groups, and the functional groups were found to force the water molecules near the sheets to remain in a liquid state due to confinement effects [7].

Bai et al. [107] demonstrated that the mean ice nucleation temperature of water containing graphene oxide sheets (average sheet size 8 nm or smaller) was demonstrated to be -27.6°. For graphene oxide sheets (8 nm in size) anchored to a silicon wafer, the ice nucleation temperature was found to be -24.6°C or higher depending upon the contact area between the water droplets and the surface. Geng et al. [108] demonstrated experimentally that a graphene oxide dispersion can suppress the growth of an ice crystal, and concluded that graphene oxide behaves as an antifreeze protein. Specifically, they found that the hydroxyl group on the graphene basal plane binds more efficiently to ice crystals than to liquid water which gives rise to a curved ice crystal surface that inhibits the further growth of an ice embryo.

Zhang et al. used molecular dynamics simulations to study the icephobicity of pristine graphene and graphene functionalized with sodium ions, chloride ions, and methane molecules [51]. Ice nucleation was more inhibited on functionalized graphene compared to pristine graphene. It was found that water molecules near the surface interacted weakly with the carbon atoms in the bare graphene, and more strongly with the functional groups in the graphene derivative substrates. Thus, the viscosity of the water molecules are higher in functionalized graphene compared to bare graphene, leading to a lower nucleation rate (and longer freezing time delay, see section 2.3.1 for details).

Akthar et al. [37] reported that fluorinated graphene produced by exposing graphene on Ru(0001) to XeF_2 molecules, can be used as a robust and lightweight anti-icing coating. Their coating was reported to have an average freezing onset temperature of -23 $\pm$ 1°C, as well as to delay ice formation for 90 minutes at $-15°C$ and 6 hours and 45 minutes at -5°C, with all data collected in high humidity conditions ($50\% - 55\%$). These icephobic properties of fluorinated graphene were attributed to higher hydrophobicity and higher viscosity of water on the surface. They suggested that the high electronegativity of fluorine makes the C-F bond highly polar, which changes the properties of the interfacial water layer. Moreover, both freezing onset temperatures and freezing delays were shown similar after multiple icing/deicing cycles over 90 days, proving a long durability of the coating.

3.8 Summary

The extreme lightweight and transparency of graphene make it an ideal material for coatings. The wettability of graphene depends on the intrinsic properties and its surroundings; the supporting material and environmental effects (substrate, air contamination, etc.). Graphene oxide is a common derivative of graphene and has many industrial applications, which makes its wetting properties of high interest. It is commonly agreed upon that graphene oxide exhibits hydrophilic properties, with carboxyl and hydroxyl being the most hydrophilic groups.

Graphene-based materials have shown to exhibit great icephobic properties [37, 96, 107]. Recently, graphene oxide was theoretically predicted to exhibit superior icephobic properties, with confined water freezing temperature as low as -37°C. This was supported experimentally, where the freezing temperature of water containing graphene oxide sheets (8 nm in size) was found to be -27.6°C. These promising results deserve attention in order to develop an icephobic coating with industrial applications.

Chapter 4

Experimental Techniques

This chapter provides an introduction to the experimental techniques used to study graphene and oxidized graphene on the atomic scale. It starts with an introduction to STM, followed by the basic principles of XPS and fitting procedures. The chapter finishes with a brief description of ultra-high vacuum and why it is used for the surface science techniques used in this thesis work.

4.1 Scanning Tunneling Microscopy

Scanning tunneling microscopy (STM) is a technique capable of imaging the electronic structure of surfaces with atomic-scale resolution. The principle is based on the quantum mechanical effect of tunneling.

4.1.1 Basic Principle

The instrument consists of an atomically sharp tip moved to within a few angstroms of the surface to be studied, as shown in figure 4.1. The tip is then moved with high precision across the surface, using three mutually orthogonal piezoelectric transducers (PET). A small bias voltage, ranging from a couple of mV to several V, is applied to maintain a tunneling current between the tip and the sample. The measured tunneling current depends exponentially on the distance between the tip and the substrate, and the density of states on both the surface and the tip (see section 4.1.2) [59].

Most STM operates in the so-called constant current mode. While the tip scans across the surface by the X and Y PET, the Z PET is in a feedback loop that applies a correction to the Z voltage to maintain a constant tunneling current. The correction voltage is a direct measure of the change in Z the tip has to perform in order to follow the contours of the sample. The correction is a

function of X and Y voltages, and therefore it is used to create a contour map of the sample surface [109, 110].

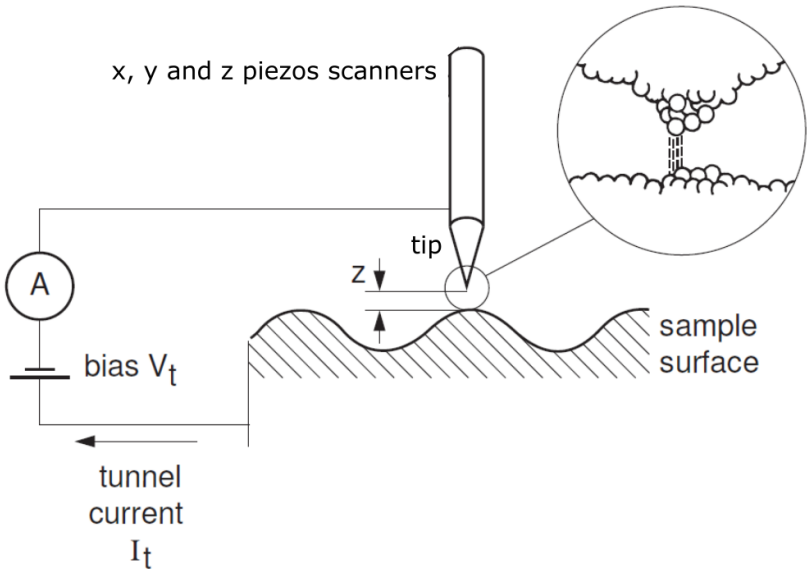

Figure 4.1: Schematic diagram of the principles of a typical STM instrument, copied and modified from [59].

There are several challenges related to the practical use of STM. One is that the tip has to be stable at an Angstrom distance from the surface under external factors such as mechanical vibration and thermal drift. In the instrument used for this thesis work, vibrational damping was done by applying external springs [110]. The thermal drift, however, will always be present in room temperature STM, but can in some cases be removed afterward by editing and filtering the images [59].

Another key challenge is that the tip has to be atomically sharp. Ideally, there should always one single atom at the edge of the tip apex at all times to scan with atomic resolution. Techniques such as cutting and etching exist and can be implemented on the tip, in general, it is impossible to control the chemical environment of the outermost atom. Hence, the tip apex is always unknown and can even change during scanning (e.g. by adsorption of adatoms) [109].

4.1.2 Tunneling Physics

A tunneling current, as a quantum mechanical effect, occurs between any two electrically distinct objects that come sufficiently close together. As the tip approaches the surface, electrons will flow between the two junctions until the Fermi levels are in equilibrium. Once in equilibrium, there is no driving force for a current to flow. To restore and maintain the current, a bias is applied to one of the junctions. If the bias voltage is applied to the tip, electrons are pumped into the tip to make it negative and to push the Fermi level up in the energy diagram. These

high energy electrons will flow into empty states of equal or lower energies in the sample. Thus, the STM image is dominated by the energy levels with the highest density of states, but all available energy levels are imaged simultaneously. Alternatively, a bias voltage can be applied to the sample allowing the opposite electron route. Hence, STM can be used to investigate both occupied and unoccupied states of the sample [59]. One should note the surface and the tip must both be conductors or semiconductors for tunneling to happen, meaning that STM can not be used on insulating surfaces.

If the potential-energy barrier is considered as a simplified trapezoid, the probability of an electron on the tip, at energy E with respect the fermi energy E_F', to tunnel to the sample, is approximately [109]:

$$T(d,E,eV) \approx exp(-2d[\frac{2m}{\hbar^2}(\phi - E - \frac{eV}{2})]^{\frac{1}{2}}) \tag{4.1}$$

where ϕ is the average work function (energy needed to displace an electron from a solid to a point in the vacuum outside the solid surface), d is the distance between surface and the tip, m is the electron mass, e is the electron charge, V is the applied voltage and $\hbar$ is Planck's constant.

For small bias voltages, equation 4.1.2 can be simplified to [109]:

$$T(d) \approx exp(-2\kappa d) \tag{4.2}$$

where κ is the vacuum decay constant $(2m\phi\hbar^2)^{1/2}$. The vacuum decay constant has a value of $10\ \mathrm{nm}_{-1}$ for typical work functions [109]. Hence, the measured tunneling current depends exponentially on the distance between the tip and the substrate. A change of 1 Å will cause a change in tunneling current of a factor of 10 [59].

Furthermore, the net current is proportional to [59]:

$$I \propto \int_{-eV}^{0} \rho_t(E)\rho_s(eV+E)T(E,eV)dE \tag{4.3}$$

where ρ_s and ρ_t are local densities of states of the surface and tip. Thus, the STM image is not only a contour map, it also show the density of states at the fermi energy of the surface.

4.2 X-ray Photoelectron Spectroscopy

X-ray photoelectron spectroscopy, XPS, provides chemical information on which elements are present at the surface of the sample.

4.2.1 Basic prinsiple

The main principle is based on the photoelectric effect. An XPS system consists of a source of ionizing x-ray radiation and an electron detector that can determine the kinetic energy of the incoming electrons, as shown in figure 4.2 [111].

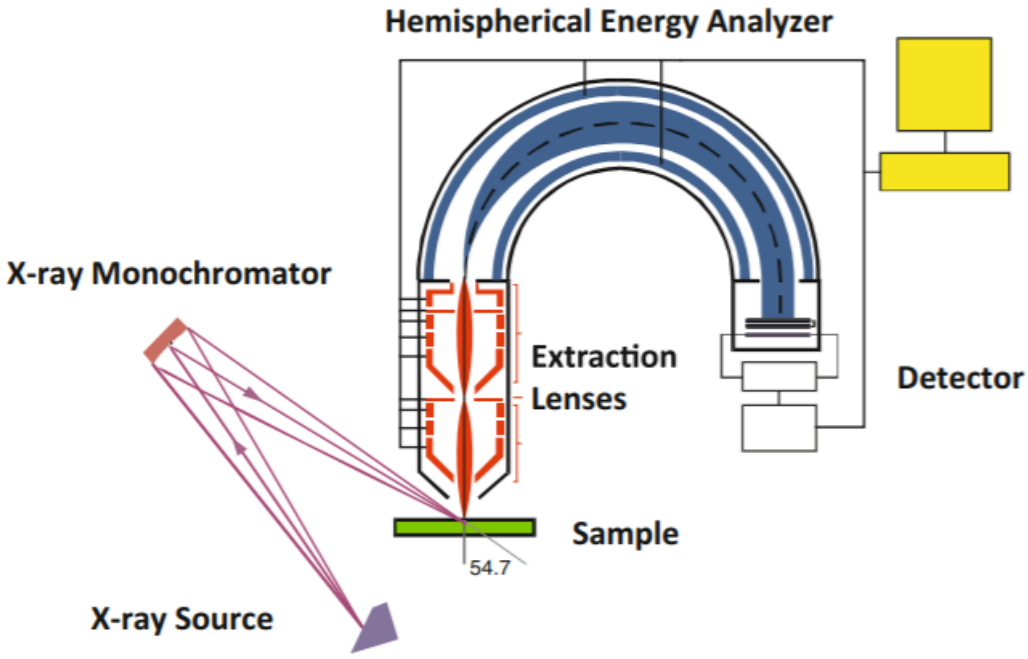

Figure 4.2: Schematic model of a typical x-ray photoelectron spectrometer similar to the one used for this thesis work. Copied from [111].

A laboratory x-ray source typically consists of a water-cooled anode bombarded by electrons arriving from a heated cathode. The electrons knock out electrons from the inner shell of atoms in the anode, creating atomic holes. There are two ways of filling these holes: i) x-ray emission or ii) Auger decay. Auger-decay is important for low energy and light elements, while x-ray emission is important for higher energy end heavier elements [59].

Alternatively, synchrotron radiation can be used as an x-ray source. Synchrotron radiation is generated when charged particles are accelerated radially in storage rings by magnetic fields. Such radiation has many advantages. The most important one related to surface science is that the synchrotron i) provides radiation that is much more intense giving better signal and ii) provides tunable radiation so one can choose the x-ray wavelength of most relevance for the experiment. Additionally, energy bandwidth passing the monochromator can be quite small (numbers), improving the energy resolution in the XPS measurement [59].

The x-rays generated by either the laboratory source or synchrotron radiation are directed towards the surface to be investigated. Through the photoelectric effect, ionizing photons result in the

emission of electrons from the sample. An electron analyzer is used to measure the E_{kin} of the emitted electrons. Theoretically, this is given by [59]:

$$E_{kin} = hv - E_{bin} - \Phi \tag{4.4}$$

where E_{bin} is binding energy, hv is the photon energy and Φ is the work function, defined as the energy required to remove an electron from the solid to an infinite distance away in vacuum, which depends on both the sample surface and the detector. However, the fermi levels of both the sample and the detector are typically aligned by grounding both. In practice, only the work function for the detector needs to be considered and can be accounted for [112].

A typical analyzer has a fixed energy window, referred to as the pass energy. Thus, only electrons having energy within a certain range are accepted. The electrons emitted at different kinetic energies are counted discretely, giving rise to the XPS spectrum. An XPS spectrum is usually a plot of the intensity of electrons versus their binding energies [111].

The binding energy can be defined as the energy difference between the initial and final states after the photoelectron has left the atom [113]. Each atom has a characteristic set of binding energies for electrons sitting in different orbitals in that element. The exact binding energy between an electron and the atom strongly depends on the chemical environment (i.e. chemical component of the atom itself and the neighboring atoms) of the element [59]. As the photon energy and the work function are fixed parameters within an experiment, the binding energy can easily be calculated from equation 4.4.

The mean free path, i.e. the distance an electron can travel before being scattered in-elastically, is directly dependent on the kinetic energy of the electrons as illustrated in figure 4.3. One can engineer the mean free path by changing the energies of the photons irradiating the surface. Electrons scattered further deep in the surface suffers from energy losses before they reach the electron analyzer, and will contribute to the background signal visible in the XPS spectrum [114].

Furthermore, geometric methods can be implemented to tune the surface sensitivity. One can measure with grazing emission instead of normal emission, as shown in figure 4.4. This way, electrons are forced to travel close to the surface, even if the mean free path is relatively long [59].

4.2.2 Fitting Procedures and Peak Shapes

In this project, the binding energy of the atoms on the surface is the most important information to get from the XPS spectrum. The binding energy gives valuable information on what kind of

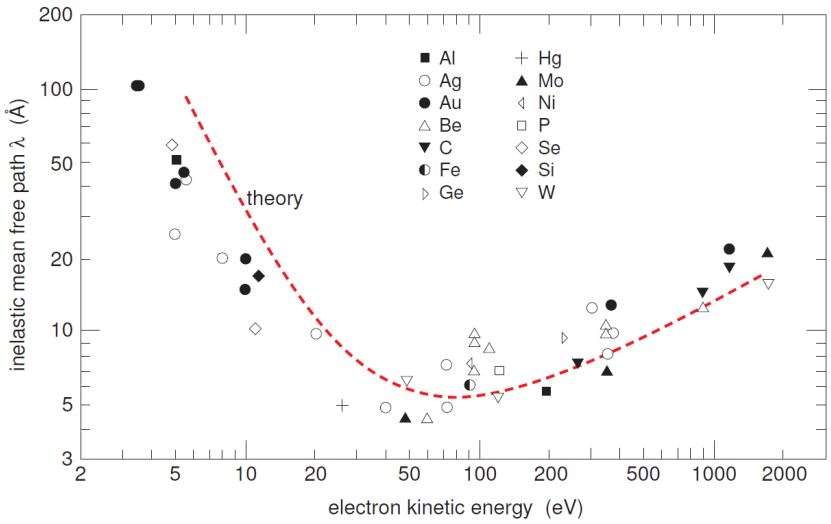

Figure 4.3: The inelastic mean free path of the electrons in solid as a function of kinetic energy. Figure copied from [114].

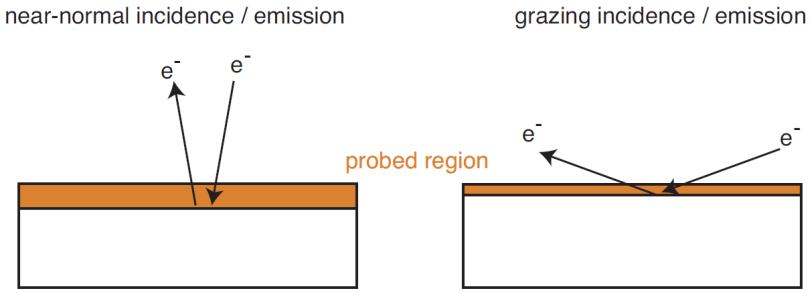

Figure 4.4: The grazing emission geometry in the right is significantly more surface sensitive than that in left. Figure copied from [59].

elements are present on the surface and what chemical environments they are in.

A detailed analysis of the binding energies in an XPS spectrum can be done by a peak fitting procedure, where each peak represents atoms in particular types of chemical environments [111]. Mainly, Gaussian and Lorentzian line shapes are used as fitting functions. The broadening of Gaussian lines occurs from the photon source, the analyzer, and the heterogeneous environments of the multiple different atoms on the sample surface. The broadening of Lorentzian shaped lines, however, is dependent on the lifetime of the transition between initial and final states.

Additionally, metallic atoms give asymmetric peaks in the photoelectric spectrum. This is because the Fermi level sits in contact with the conduction band, thus an electron can be excited from just below the Fermi energy to just above it where the net excitation energy is zero [59]. This property leads to the distribution of charges. When one electron is removed by an incoming photon, all of the surrounding atoms contribute a small amount of charge to fill the newly formed hole. Hence, it becomes more difficult to extract electrons as more photons arrive, therefore electrons gradually shift to higher binding energies, resulting in an observed asymmetric tail

called a Doniach-Šunjić line in the XPS spectrum [115]. Additionally, this peak has a Lorentzian contribution, where the width is dependent on the lifetime of the excited states.

The Doniach-Šunjić tail does not occur for insulating atoms because they cannot redistribute charge. It should be mentioned that XPS is not suitable on insulating surfaces because the loss of photoelectrons induces a rapid charging of the surface. Thus, all peaks will move in energy, and spectroscopy gradually becomes useless [59].

In this thesis, the peaks of O1s and C1s environments are studied. Carbon in graphene has metallic behavior, hence the peak should be fitted with the asymmetric Doniach-Šunjić function. Additionally, it should be fitted with a convolution of both Gaussian and Lorentzian shaped functions. On the other hand, oxygen in O1s is insulating and is therefore symmetric. The O1s peak is usually so broad Gaussian-shaped that the intrinsic Lorentzian-shape is not visible.

4.3 Ultra High Vacuum

Ultra-high vacuum (UHV) is the pressure of 10^{-9} mbar and below. UHV conditions can be obtained and maintained by pumping out gas inside a vessel made of stainless steel.

UHV conditions are necessary to keep a sample chemically clean over time and to avoid any unwanted adsorbates [59]. Some surface science techniques, such as XPS, strictly require UHV conditions because of the transmission of photoelectrons. If XPS is performed in air, photoelectrons emitted from the sample will quickly collide with any air contaminant and will thereby suffer from energy loss before reaching the detector. UHV conditions are advantageous for STM to avoid oxidation or contamination of both the tip and the sample during scanning, but it is possible to perform STM measurements in ambient conditions. Nevertheless, one can more easily collect high-resolution STM images in UHV than in air [59].

Chapter 5

Experimental Procedure

The present chapter describes the experimental procedure for this thesis work. Two samples with different oxygen coverage, namely the low- and high-coverage sample, were prepared and characterized in the surface dynamic laboratory at Aarhus University. Subsequently, the samples were transported to the nanophysics laboratory at the University of Bergen for the macroscopic wetting and icing experiments. Finally, the sample with the highest coverage was transported back to Aarhus for post-ice analysis with scanning tunneling microscopy and both laboratory and synchrotron x-ray photoelectron spectroscopy.

5.1 Surface Science Characterization - Pre Icing Experiments

The surface science experiments conducted before wetting and icing experiments were completed at the surface dynamics laboratory at Aarhus University (Aarhus, Denmark). Three ultra-high vacuum chambers were used in this project, named the "Blue", "Green" and "Coal" chamber, as shown in figure 5.1. The Blue chamber can obtain the best pressure for graphene growth, the Green chamber is equipped with a laboratory XPS instrument (described in 4.2) and the Coal chamber is equipped with an oxygen doser. All three chambers are equipped with an Aarhus STM type (described in section 4.1), however the Coal chamber STM was not working throughout this project. To utilize different instruments, transportation between chambers was necessary and this was performed by a vacuum suitcase. The base pressure of the vacuum suitcase is estimated to be 10^{-5} mbar.

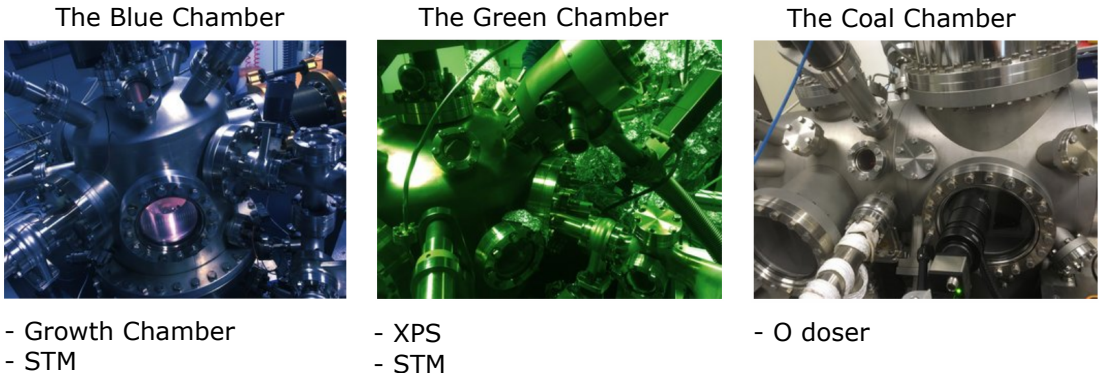

Figure 5.1: The UHV chambers used in the project, named the Blue, Green, and Coal chamber. Reprinted from [116].

5.1.1 Material Preperation

A circular (111) iridium crystal was mounted on a sample holder made of Tantalum, as shown in figure 5.2. On the backside, a K-type thermocouple was mounted close to the crystal, protected with a Tantalum foil, to measure the crystal temperature. This is shown in the right panel of figure 5.2, where the wires mounted are in direct contact with the backside of the crystal and thermocouple legs.

Two samples with different coverage were prepared and investigated. For the first sample, the goal was to reproduce a similar sample to that reported in ref. [8]. This sample will be referred to as the low-coverage sample. For the second sample, the goal was to achieve a saturated oxygen sample, and this sample will be referred to as the high-coverage sample.

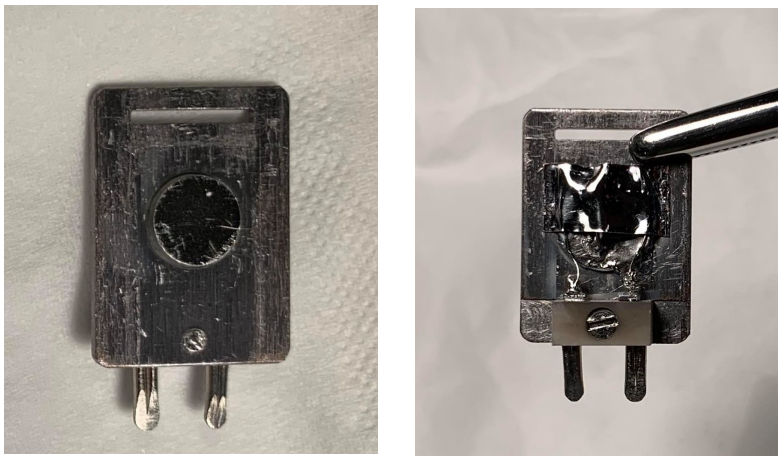

Figure 5.2: Left: the circular metal is the Ir(111) crystal mounted on a sample holder made of Tantalum. Right: The back-side of the sample holder. The thermocouple of type K is connected on the backside of the sample and protected with Tantalum foil. The wires are in touch with the thermocouple legs, where the temperature can be measured.

Preperation of the Low-Coverage Sample

The crystal was cleaned in the Green UHV chamber by several cycles of sputtering and annealing, followed by annealing in low oxygen pressure. Sputtering is the bombardment of ions towards the surface in order to remove chemisorbed species. After sputtering, the sample is usually left in a heavily damaged state which can often be repaired by annealing the sample close to its melting point [59]. During the anneal, impurities might migrate to the surface such that several of cycles of sputtering and annealing is needed. Annealing the sample in low oxygen pressure can remove any carbon contamination by creating a desorbing CO gas [59]. Sputtering was done with Ar^+ ions at 2 keV followed by annealing at progressively higher temperatures up to 1150°C. Finally, the sample was annealed in O_2 at a partial pressure of $3 \cdot 10^{-7}$ mbar between 300-900°C three times. The crystal was judged clean via STM and XPS.

Graphene was thereafter grown in the same UHV chamber (the Green chamber) by chemical vapor deposition (described in 3.2), using ethylene as the carbon source. The clean Ir(111) crystal was exposed to ethylene at $5 \cdot 10^{-7}$ mbar for 10 minutes at room temperature. The crystal was flashed in vacuum to 1015°C, before cooling to 900°C. At this temperature, the sample was again exposed to ethylene at a pressure of $3 \cdot 10^{-7}$ mbar for 10 minutes. The gas was stopped and the sample was cooled slowly (roughly ~ 0.5°C/s). The cooling was completed manually. Finally, the sample was annealed to 400°C for 10 minutes to get rid of any impurities that might have arisen during graphene growth, before STM and XPS characterization that were conducted

in the same chamber.

Next, the sample was transported to the Coal chamber where oxygen dose was performed. A schematic of the set-up is presented in figure 5.3. The low-coverage sample was not annealed before the oxygen dose. If one was to re-do the experiments annealing is highly recommended to remove any impurities introduced during transportation. The sample was exposed to a flux of oxygen atoms for 30 seconds, produced by thermally cracking O_2 in an Ir capillary heated to 1560°C. The sample was placed 6.0 cm from the doser, and the flux of atoms reaching the sample was estimated to be $4{\cdot}10^{11}$ atoms/s. The sample temperature was kept at room temperature, and background pressure in the chamber was fixed to $1.8 \cdot 10^{-7}$ mbar. The oxygen atoms were normal incident on the sample to maximize the kinetic energy of the oxygen atoms normal to the surface, which aids in overcoming the reaction barrier and thus results in a high cross-section for the reaction. After the oxygen dose, the O-Gr/Ir sample was transported to the Green chamber to do STM and XPS analysis. Before the analysis, the sample was annealed to 120°C for 30 minutes to remove any air contamination during transportation. Finally, the sample was exposed to air for $\sim$1 hour before being transported to the Blue chamber to collect more STM images.

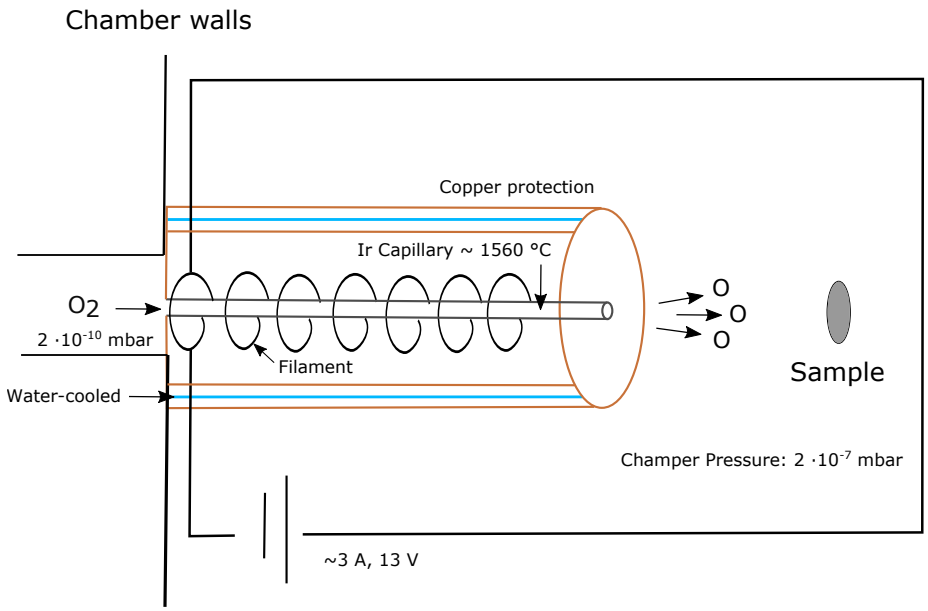

Figure 5.3: Schematic illustration of the oxygen doser used.

Preperation of the High-Coverage Sample

The crystal was cleaned in the Blue UHV chamber by several cycles of sputtering and annealing, followed by annealing in low oxygen pressure (see section 5.1.1 for an explanation of why this is necessary). Again, sputtering was done with Ar^+ atoms at 2 keV and was followed by annealing

at progressively higher temperatures up to 1000°C. The sample was subsequently annealed in O_2 at a partial pressure of $3 \cdot 10^{-7}$ mbar between 300-900°C three times. The crystal was judged clean via STM (and not XPS since that instrument was not available in the Blue chamber).

Graphene was grown in the same UHV chamber (the Blue chamber) by chemical vapor deposition, using ethylene as the carbon source. At a temperature below 300°C, the clean Ir(111) crystal was exposed to ethylene with a chamber pressure of $3 \cdot 10^{-7}$ mbar for 18 minutes. The crystal was then flashed in vacuum to 1150°C, before cooling to 900°C. At this temperature, the sample was again exposed to ethylene at a pressure of $3 \cdot 10^{-7}$ mbar for 15 minutes. The gas was stopped and the sample was cooled in the vacuum at a rate of 0.2°C/s (by a temperature-controlled program). The Gr/Ir(111) sample was characterized by STM before transported to the Green chamber for XPS characterization (since the XPS instrument was not available in the Blue chamber). Before XPS measurements, the sample was annealed to 120°C for 20 minutes.

The sample was transported to the Coal chamber where it was annealed to 120°C before oxygen dose (see figure 5.3 for schematic illustration). Next, the sample was exposed to a flux of oxygen atoms for 4 minutes, produced by thermally cracking O_2 in an Ir capillary heated to 1560°C. The sample was kept at room temperature and placed 10.0 cm from the doser, so the flux of O atoms reaching the sample was estimated to be $1.5 \cdot 10^{11}$ atoms/s. The background pressure was $1.8 \cdot 10^{-7}$ mbar and oxygen atoms were normal incident on the sample. Finally, the O-Gr/Ir sample was transported to the Blue and Green chamber to do STM and XPS analysis, respectively.

5.1.2 STM Characterization

STM images were recorded at room temperature using an Aarhus STM type [110]. All STM images collected and used in this thesis were analyzed and edited using WSxM analysis software [117]. The images were flattened and corrected for thermal drift.

For the low-coverage sample, scanning was done on Gr/Ir(111) at three random areas with micrometers spacing, whereas scanning on O-Gr/Ir(111) was performed on three random areas with millimeters spacing. For the high-coverage sample, scanning was done on two random areas with micrometers spacing, both on Gr/Ir(111) and on O-Gr/Ir(111). For future reference, one should be consistent with scanning on at least three random areas on the surface, preferably with millimeters spacing to ensure the surface is uniform across the sample.

The STM images were calibrated by using a fast Fourier transform (FFT), an example of which is shown in figure 5.4. First, the graphene atoms line spacing was found by measuring the distances between the opposing maxima the FFT (figure 5.4b)). The line spacing measurements were re-calculated to lattice constants using geometry. The lattice constants were used to calibrate

the STM images with respect to the theoretical lattice constant for graphene (2.46 Å) using the WSxM [117] software. This procedure is not applicable for images without atomic resolution. For such images, a calculated calibration factor for an image obtained in the same data set was used.

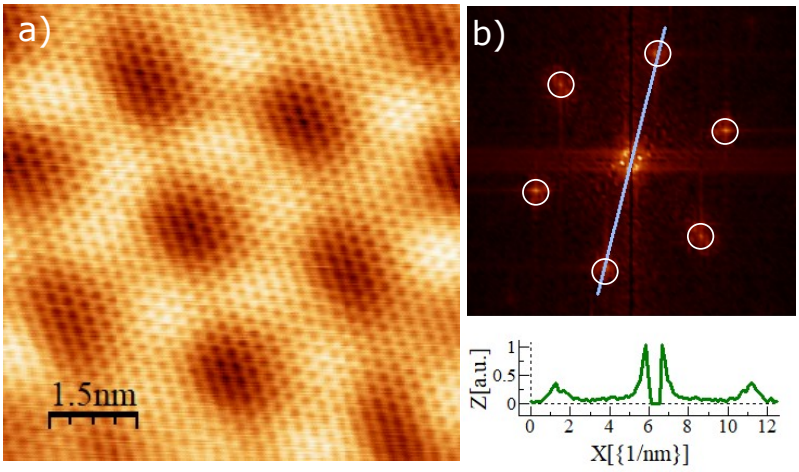

Figure 5.4: a) Scanning tunneling microscopy. b) Fast Fourier transform (FFT) of the STM image in a). The outer maxima indicated with white circles denote the graphene carbon atoms. The line spacing was measured and used to calibrate the image with respect to the theoretical lattice constant for graphene.

5.1.3 XPS Characterization

Data were collected from the laboratory XPS, consisting of an mg x-ray source of 300 W power (XR 50) and a hemispherical energy analyzer (Phobios 150) (Specs, Germany). Photons with an energy of 1250 eV were generated by the source, and irradiated an elliptical spot with area 1-2 cm^2 on the surface. For both samples, the data collected with normal emissions are averaged over 50 scans. The step width between two data points was 0.05 eV (except for O1s Gr/Ir(111) which was 0.1 eV), the pass energy was set to 10 eV, the dwell time was 0.5 seconds and the diameter of the detector iris was set to 25 mm. XPS fitting procedure was completed using the KolXPD software [118]. A Gaussian function with a linear background was used to fit all O1s data, whereas a gaussian Doniach-Sunjic function convoluted with a Gaussian using linear background was used to fit C1s data. Details behind the fitting procedure can be found in section 4.2.2.

5.2 Wetting and Icing Experiments

In this thesis, the term "wetting and icing experiments" includes investigating wetting properties by the measurement of water contact angles (WCA), freezing onset temperature, and freezing onset delay times. All icing experiments were conducted at the University of Bergen (Bergen, Norway) following the method described in [37].

Care was taken to transport the sample in the least invasive way. The crystal sample holder was placed upside down in the copper block where it could sit firmly as shown in figure 5.5. The sample in the copper block was protected by aluminum foil and placed in a container. No damage was observed to the sample after transportation.

Figure 5.5: Sample placed upside-down in the copper block.

A DataPhysics OCA 20 instrument (DataPhysics, GmbG, Germany), schematically shown in figure 5.6, was used for the wetting icing experiments investigation. The system is equipped with a high-speed camera (red part), a computer software able to control the droplet-dispensing unit (blue part), and a temperature-controlled Peltier stage along with a water cooling device (green part). Data analysis was performed using the SCA 20 software which comes with the instrument.

A special copper block, where the crystal sample holder could fit, was designed to ensure thermal transfer from the cooling plate to the crystal. The copper block, along with the crystal sample holder, is shown in figure 5.7. Furthermore, a K-type thermocouple was mounted on the back of the crystal to get an exact measurement of the crystal temperature during experiments. The measurements were don in ambient air at room temperature $23° \pm 1°$ and relative humidity of $29\ \% \pm 3\ \%$.

A 2 µL droplet of deionized water was deposited on the crystal, and the WCA was measured using the optics along with the computer software. Three cycles for the low-coverage sample and four cycles for the high-coverage samples were collected over five days, each cycle consisted of 5 WCA measurements. After each WCA measurement, the Peltier plate was cooled at a

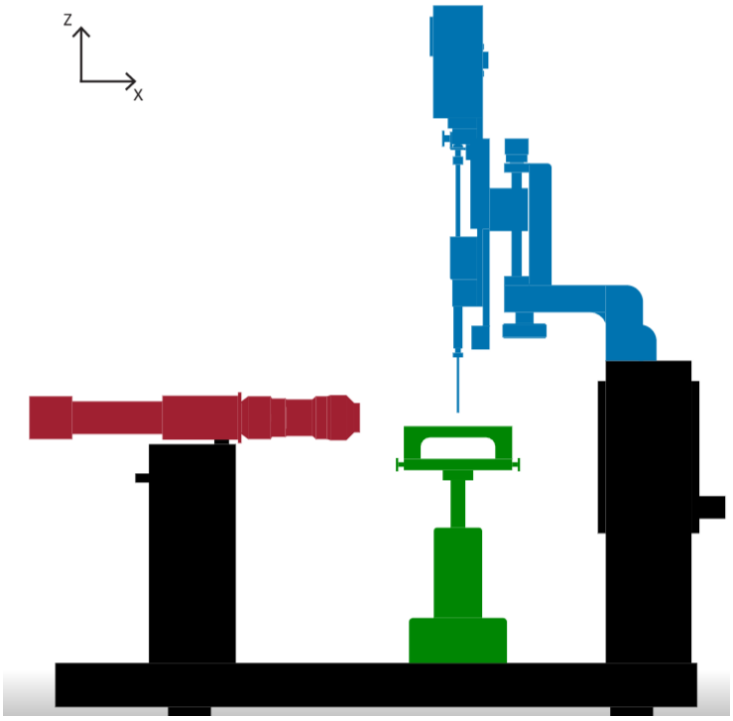

Figure 5.6: Schematic overview of the optical WCA system used, copied from [119].

rate of 0.16°C/s until the droplet froze. The freezing onset temperature, discussed in 6.4.2, was observed and measured. For the freezing delay measurements, the temperature was lowered to three subzero temperatures (-5°C, -10°C, and -15°C) at which the time before the freezing onset was measured. The exact temperature of the crystal was allowed to fluctuate ±0.3°C from the set temperature for the freezing delay measurements. After the droplet froze, the stage was heated to room temperature. The droplet was gently removed by non-hairy tissue. Any remaining droplets were given time to evaporate before repeating the icing experiment.

5.3 Surface Science Characterization - Post Icing Experiments

The O-Gr/Ir(111) high-coverage sample was brought back to Aarhus University for characterization in the surface dynamics lab after icing experiments. Only the high-coverage sample was investigated due to time limitations. The sample was transported upside down in the copper block, where it could sit firmly, back to Aarhus University. The sample was analyzed in the blue chamber with STM and the green chamber with XPS. Transportation between chambers was done in air.

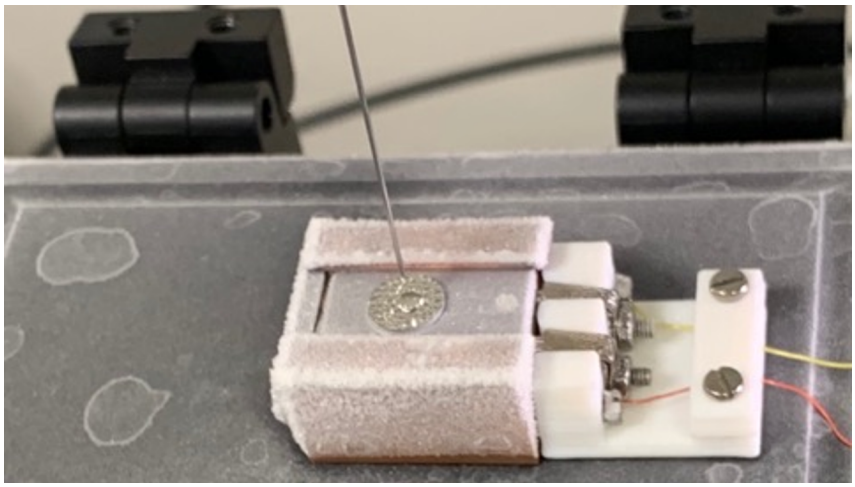

Figure 5.7: The special copper block designed to ensure thermal transfer between the Peltier cooling stage and the Ir crystal. The crystal is the circular metal in the middle. Red and yellow wires are connected to the thermocouple.

5.3.1 STM Characterization

STM characterization of the high-coverage sample after icing experiments are collected and analyzed in accordance with that described before icing experiments in section 5.1.2.

5.3.2 XPS Characterization

The laboratory XPS characterization of the high-coverage sample after icing experiments was collected and analyzed in accordance with that described prior to icing experiments in section 5.1.3. However, when measuring with grazing emission, more scans were needed (because the x-ray source does not get as close to the sample as when measuring with normal emission). Therefore, O1s data was the average of 100 scans and C1s data was the average of 150 scans with the grazing emission, and the detector iris was set to 15 mm. The step width between two data points was 0.05 eV, the pass energy was set to 10 eV, the dwell time was 0.5 seconds and the detector iris was set to 25 mm for all experiments.

In addition to using the laboratory XPS, the sample was investigated using synchrotron radiation generated by ASTRID2 in the MatLine beamline, since it is a more surface-sensitive technique (see section 4.2 for details). The photons generated was tuned to have energies of 340 eV and 650 eV to collect data for C1s and O1s, respectively. An elliptical spot with an area of 0.5-1.5 mm^2 was irradiated onto the sample. The O1s 650 eV data are averaged over 8 scans with normal emission and 20 scans with grazing emission. The C1s 340 eV data was the average of 3 scans with normal emission and 10 scans with grazing emission. For all datasets collected with the synchrotron XPS, the step width between two data points was 0.05 eV, the pass energy was 10 eV and the dwell time was 0.5 seconds.

The synchrotron XPS system was calibrated to the exact position of the Ir4f peak. The exact position was found as follows: first, the fermi edge was measured at a photon energy of 120 eV. Subsequently, the kinetic energy in the spectrum was shifted with respect to the fermi edge offset. Thereafter, the first and second-order of the Ir4f peaks at a photon energy of 120 eV were fitted with Doniach Šunjić functions convoluted with a Gaussian using Shirley backgrounds. The real (calibrated) photon energy hv^* was now found by the kinetic energy peak difference, that is $hv^* = KE_{2nd} - KE_{1st}$. After the photon energy had been corrected for, the exact binding energy for the Ir4f peaks was found. Then, the binding energy was shifted in all photon energies spectra, so that the Ir4f peak position at the respective photon energy matched the true position measured.

Chapter 6

Result and Analysis

Two O-Gr/Ir(111) samples with different oxygen coverage were prepared in ultra-high vacuum and investigated with STM and XPS. For the first sample, the goal was to reproduce a similar sample to that reported in [8]. This sample is referred to as the low-coverage sample. For the second sample, the goal was to achieve a saturated oxygen sample, referred to as the high-coverage sample. A third sample of bare graphene on Ir(111) was prepared and preliminarly analysis were preformed. However, due to the covid-19 situation, this could not be implemented as part of this thesis work.

After sample preparation and characterization, the two samples were brought to Bergen for wetting and icing experiments, where a thorough investigation of their wetting and icephobic properties were completed by measuring contact angles, freezing onset temperatures, and freezing delays. Micro-litre droplets can be considered rough to the angstrom-scale surface, and any changes on the surface on the atomic scale is of importance because it can give information about the durability of the coating. Therefore, an atomic-scale characterization (XPS and STM) of the high-coverage sample after the icing experiments were conducted.

This chapter is structured in the following way, section 6.1 I present the atomic characterization measurements on the low-coverage sample, starting with the STM images followed by the XPS spectra. In section 6.2, I do the same for the high-coverage sample. Section 6.3 presents a corrugation analysis of the two samples conducted by the STM. Then follows section 6.4 where the measurements of wetting and icephobic properties are presented. In section 6.5 I present the atomic scale characterization measurements of the samples after macroscopic wetting and icephobic properties measurements. Finally, based on the findings from the post-ice STM and XPS measurements, I investigate the wetting and icephobic measurements with respect to where on the sample they were deposited in section 6.6.

6.1 Surface Science Investigation of the Low-Coverage Sample

6.1.1 Characterization of Graphene on Ir(111)

Graphene growth, STM, and XPS characterization of Gr/Ir(111) was completed in the same UHV chamber. Oxygen dosing was performed in a different chamber and the vacuum suitcase (base pressure 10^{-5} mbar) was used to transport the sample. The sample was not annealed before the oxygen dose in the dosing chamber. See section 5.1.1 for experimental details.

STM Analysis

STM images of graphene on Gr/Ir(111) are shown in figure 6.1. The image in figure 6.1a) shows an area of defect-free graphene with atomic resolution. The graphene unit cell is shown with a white rhombus. The larger pattern, which is more obvious on b) but visible on all images, is the moiré superstructure. It arises from the mismatch between the lattice constant for graphene and Ir(111) surface atoms (see section 3.2.1 for details).

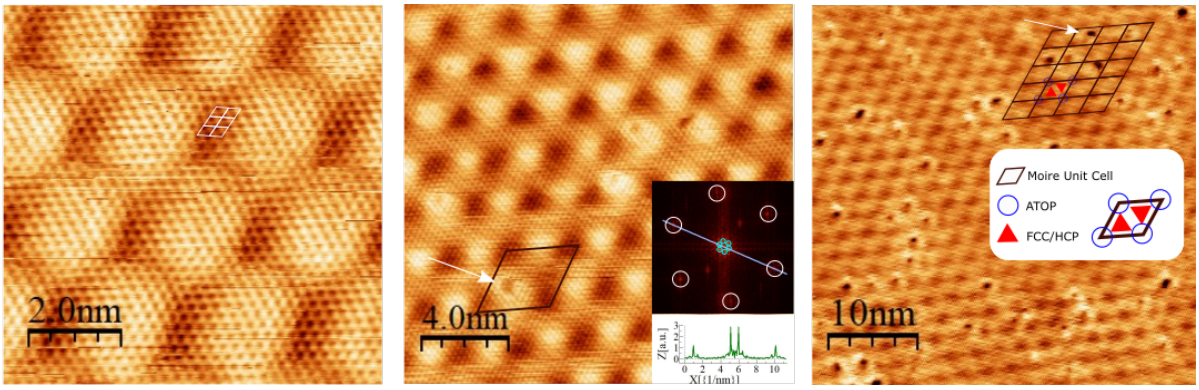

Figure 6.1: STM images of graphene on Ir(111) (low-coverage sample). a) White rhombus denotes the graphene unit cell. Scanning parameters: It: -530 pA, Vt: -9.8 mV. b) On larger scale areas, some defects (shown with white arrow) are visible. Moiré unit cell shown with black rhombus. Scanning parameters: It: -570 pA Vt: -11.9 mV. Inset: FFT of the image. c) Here, typical defects, referred to as "ring-like" structure in literature [8] are clearly visible as dark spots. Scanning parameters: It: 550 pA Vt: 24.1 mV.

The graphene and moiré periodicities were studied by fast fourier transformation (FFT), shown as the inset in figure 6.1b). A larger image of the FFT can be found in Appendix A.1.1. The graphene atom line spacing was found by measuring the distance between the outer opposing maxima, indicated with white circles. These values were used to calibrate the image with respect to the theoretical value of 0.246 nm (see section 5.1.2 for details). Next, the moiré line spacing was found by measuring the inner opposing maxima, indicated with light blue circles. The line

spacing values were re-calculated to lattice constants with geometry. The spread was calculated from the three measurements. The moire lattice constant was found to be 2.4 ± 0.2 nm, in good agreement with literature [69].

Figure 6.1b) and c) show STM images of larger areas, which reveal the presence of defects on the sample (shown with white an arrow). These defects appear as bright rings with dark centers, referred to as the ring-like structure in literature [8, 71]. It is widely accepted that the main reactive sites in the Gr/Ir(111) moiré superstructure are at the FCC/HCP regions [8, 71, 70]. Since the defects in image b) and c) are observed to sit on bright regions only, these regions are labeled as FCC/HCP, whereas the darker regions are labeled as ATOP sites. The schematic inset in figure 6.1c) further illustrates the labelling used.

XPS analysis

The XPS O1s and C1s spectra prior to oxygen exposure are shown in the lower parts of figure 6.2a) and b), respectively. The purple dots are the raw data, the green curve is the fit and the grey line is the background. Each peak represents carbon or oxygen atoms in a particular type of chemical environment. All peaks and the fitting procedure are summarized in table 6.1 and 6.2.

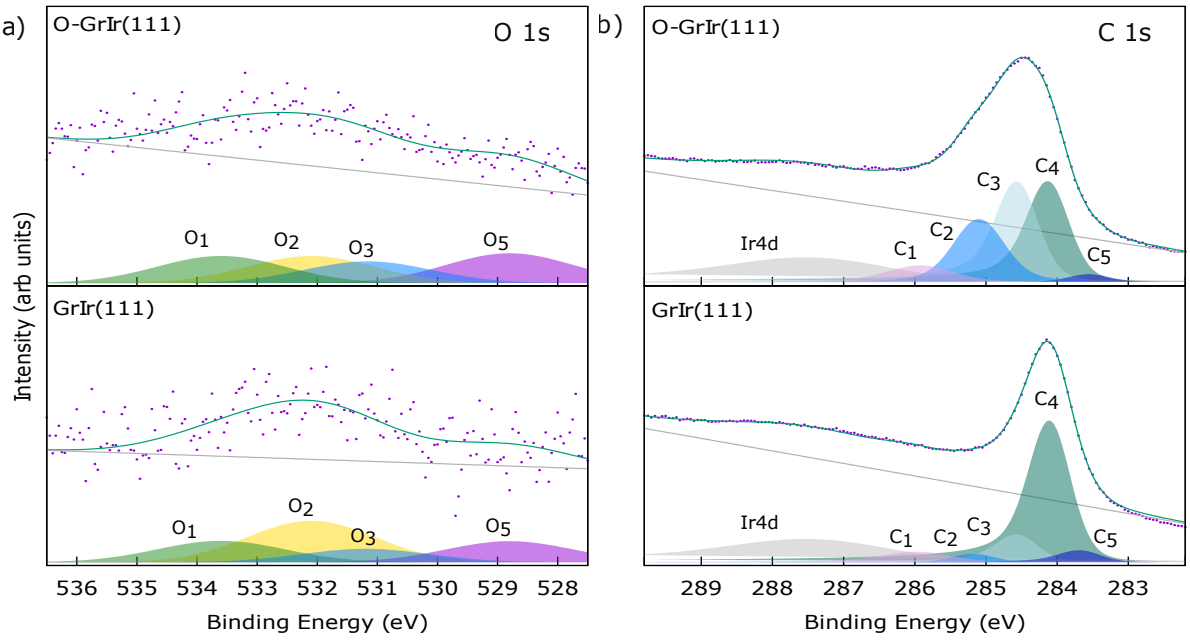

Figure 6.2: Low-coverage sample. XPS a) O1s and b) C1s spectra for samples prior (lower) and after (upper) low atomic oxygen exposure.

The O1s spectrum shows that there are oxygen components present on the sample prior to oxygen exposure, likely due to defects introduced during growth, which may occur if impurities are

present in the carbon gas. This observation is in agreement with the STM images shown in section 6.1.1. Three peaks: O_2 (532.10 eV), O_3 (531.20 eV), and O_5 (528.80 eV), can be fitted and were attributed to ethers, enolate groups, and epoxy and carbonyl groups respectively [8, 85]. Additionally, a peak at higher binding energy O_1 (533.60 eV) is seen. Some publications suggest that this peak can be assigned to hydroxyl (C-OH) groups [120, 121, 122].

In the C1s spectrum, the sp^2 carbon component, C_4, is prominent before oxidation and positioned at 284.08 eV in agreement with literature [8]. The Ir4d peak originates from the diffraction of the photons coming from the x-ray source. Additionally, a contribution from sp^3 peaks are observed, namely C_1 (285.90 eV), C_2 (285.20 eV), C_3 (284.60 eV) and can be attributed to carbonyl groups or a small amount of epoxy groups, ethers and enolate groups, respectively [8, 85]. The sp^3/sp^2 peak ratio, where sp^3 is the amplitude of all peaks besides Ir4d and C_4, is 0.30. This ratio gives an indication of the quality of graphene. On an ideal, clean graphene sample, the sp^3/sp^2-ratio is 0. Finally, the C_5 peak arises at 283.65 and can be attributed to graphene decoupled from the Ir(111) substrate due to intercalation of oxygen.

Table 6.1: XPS O1s peaks and fitting parameters summarized for the low-coverage sample. The peaks are fitted using Gaussian function with linear background. See section 4.2.2 for explanation behind fitting procedure. BE stands for binding energy and GFWHM Gaussian full width half maximum.

Component	**BE (eV)**	**GFWHM (eV)**	**Assignment**
		O-Gr/Ir(111)	
O_1	533.60	2.50	C-OH [120]
O_2	532.10	2.50	C-O-C [85]
O_3	531.16	2.50	C-O [8]
O_4	530.20	2.50	O-Ir(111) [84]
O_5	528.80	2.50	C=O [8]
		Gr/Ir(111)	
O_1	533.60	2.50	C-OH [120]
O_2	532.10	2.50	C-O-C [85]
O_3	531.20	2.50	C-O [8]
O_4	530.20	2.50	O-Ir(111) [84]
O_5	528.80	2.50	C=O [8]

Table 6.2: XPS C1s peaks and fitting parameters summarized for the low-coverage sample. The peaks are fitted using Doniach-Šunjić function convoluted with a Gaussian, and a linear background. See section 4.2.2 for explanation behind fitting procedure. BE stands for binding energy, GFWHM and LFWHM for Gaussian and Lorenzian full width half maximum respectively and asym for the asymmetric fraction allowed.

Component	**BE (eV)**	**GFWHM (eV)**	**LFWHM (eV)**	**Asym**	**Assignment**
			O-GrIr(111)		
Ir4d	287.30	2.30	0.50	0.12	Ir4d
C_1	285.88	0.9	0.26	0.00	C=O [8]
C_2	285.10	0.67	0.28	0.00	C-O-C [85]
C_3	284.53	0.60	0.14	0.11	C-O [8, 85]
C_4	284.10	0.60	0.14	0.10	C-C [8]
C_5	283.54	0.60	0.14	0.0	Decoupled graphene [84]
			GrIr(111)		
Ir4d	287.36	2.3	0.50	0.12	Ir4d
C_1	285.84	0.74	0.28	0.08	C=O [8]
C_2	285.18	0.34	0.30	0.00	C-O-C [85]
C_3	284.53	0.60	0.14	0.10	C-O [8, 85]
C_4	284.05	0.60	0.14	0.10	C-C [8]
C_5	283.50	0.60	0.14	0.01	Decoupled graphene [84]

6.1.2 Oxidized Graphene on Ir(111)

STM analysis

STM images of O-Gr/Ir(111) are shown in figure 6.3. Defects appear again as ring-like structures. A comparison of image 6.3a) to 6.1a) shows that the density of defects has increased slightly after oxygen exposure, likely induced by the oxygen cluster formed during the atomic oxygen dose [8]. The level of chemisorbed oxygen atoms is expected to be very low based on the low density of defects observed.

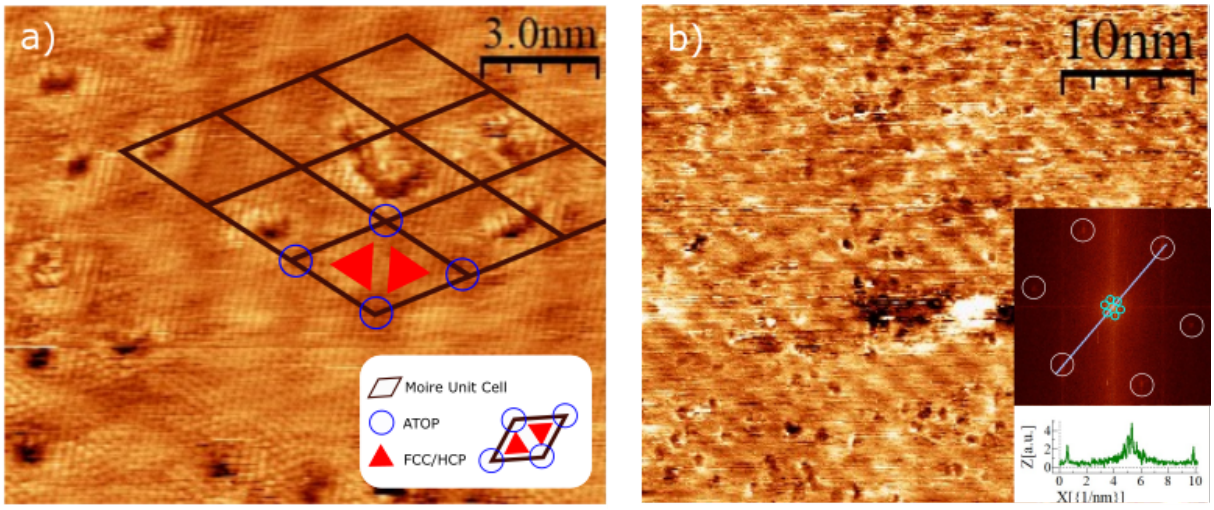

Figure 6.3: STM images of the Gr-Ir(111) sample after 30 seconds of oxygen exposure. a) The unit cells of the repeated moiré pattern is shown with black rhombus. Blue circle denote the ATOP areas, whereas red triangled denote FCC/HCP sites. Scanning parameters: It: 960 pA, Vt: 11 mV. b) Scanning parameters: It: 1490 pA, Vt: 5.5 mV. Inset: Fast fourier transform (FFT) of the image.

In figure 6.3b), the FFT of the STM image is shown as the inset. A larger image of the FFT can be found in Appendix A.1.1. By using the same line spacing analysis of FFT image as for Gr/Ir(111), the moiré lattice constant was found to be 2.5 ± 0.1 nm, confirming that the moiré structure is intact after oxidation (see section 3.2.1 for details about the moiré structure). The defects are only observed to bind to the bright regions, hence the brighter regions are labeled FCC/HCP sites whereas the darker regions are labeled ATOP sites. In figure 6.3a), the unit cells of the moiré structure are shown with a black rhombus. The labeling is further illustrated by the schematic inset.

The FCC sites in the moiré structure have been reported to be slightly more reactive than the HCP sites [8, 87]. Cassidy et al. showed that if all FCC sites of the sample were covered, the oxygen coverage would correspond to 18 % $\pm$ 1 % [8]. An estimate of the oxygen coverage (i.e. number of oxygen atoms over the number of carbon atoms) can be calculated from the

STM images with the assumption that for the low-coverage sample, only the FCC sites were covered by oxygen clusters. Three distinct STM images (included in Appendix A.1.2) were used to calculate the ratio of FCC occupied sites over the total number of FCC sites. This ratio was subsequently multiplied with 0.18 to find the coverage for the whole sample. Following this method, the oxygen coverage was found to be 7.7 % $\pm$ 0.4%.

The STM image in figure 6.3b) was collected after air exposure ($\sim$1 hour). Thus, the density of defects and the moiré structure are intact after introducing the sample to ambient air for a limited period of time.

XPS analysis

The XPS O1s and C1s spectra after oxygen exposure are shown in the upper parts of figure 6.2a) and b), respectively. The purple dots are the raw data, the green curve is the fit and the grey line is the background. Each peak represents carbon or oxygen atoms in a particular type of chemical environment. All peaks and the fitting procedure are summarized in table 6.1 and 6.2.

After oxidation, the signal-to-noise ratio increased slightly in the O1s spectra, indicating that oxygen absorbed on the surface has increased on the sample. However, the O1s signal is low compared to literature [8]. In contrast, the C1s spectrum witness a huge increase in all sp^3 components. The sp^3/sp^2 ratio has increased to 1.33. If the increase in the sp^3 peaks was due to the oxidation alone, one would expect a similar increase in O1s spectra, which was not observed. Thus, other processes are believed to have induced the sp^3 peaks in carbon spectra. Since no other components were visible on the XPS survey, this was attributed to hydrocarbon contaminants.

Any hydrogen contaminants adsorbed may have blocked the oxygen atoms coming from the doser and prevent enolate groups to form, which could be a possible explanation of why the signal of the O1s components remained low, and why the enolate groups in the O1s spectra were not further increased with respect to the other components. If the experiments were to be re-done, one should be consistent with annealing the sample after transportation in the vacuum suitcase.

6.1.3 Summary

After graphene growth, three random areas with micrometer spacing were scanned on with STM. A high density of defects was observed, most likely induced by impurities in the growth gas. XPS data showed that some oxygen contaminants were present on the surface. Thus, the defects are attributed to either C-O or C-OH, so they were considered not to damage the sample. Besides the defects, graphene was judged to be of good quality.

After oxygen exposure, three random areas with millimeter spacing were scanned on. The

density of defects was observed to have increased. From three separate STM images, the oxygen (and/or possibly hydrocarbon) coverage was estimated to 7.7 % $\pm$ 0.4 %. This was estimated under the assumption that oxygen clusters have only bonded to FCC sites (as they are slightly more reactive than HCP sites).

The XPS O1s signal was low whereas the C1s spectrum had a high sp^3/sp^2 ratio. No other contaminants could be observed in the XPS survey. As such, hydrocarbons are believed to have induced the high signal of sp^3 peaks observed in the C1s spectra. Since the sample was not annealed prior to oxygen dose, any hydrocarbons may have blocked enolate groups to form during oxidation.

6.2 Surface Science Investigation of the High-Coverage Sample

Graphene growth and STM data were collected in the same chamber for the high-coverage sample. XPS and oxygen dosing were performed in different chambers and the vacuum suitcase was used to transport the sample. The base pressure in the vacuum suitcase is estimated to be 10^{-5} mbar. See section 5.1.1 for experimental details.

6.2.1 Characterization of Graphene on Ir(111)

STM analysis

STM images of graphene on Ir(111) prior to oxygen exposure are shown in figure 6.1. This surface was found to have a low concentration of defects, which is likely due to better growth conditions.

The moiré structure (discussed in more detail in section 3.2.1) is visible in all images. The dark regions are assumed to correspond to ATOP sites and the brighter regions are assumed to correspond to FCC/HCP sites, in agreement with literature [69]. The moiré unit cells are indicated with a black rhombus in all images. A fast fourier transform of 6.4b) is shown as the inset (the full image can be found in Appendix A.1.1). The outer maxima correspond to graphene atoms, while the inner maxima correspond to moiré structure. Similar FFT analysis procedure described in section 6.1.1 was used to find the moire lattice constant from the FFT to be 2.5 nm $\pm$0.1 nm, in agreement with literature [69].

A small area in the lower part of figure 6.4c) marked with "Ir(111)", is not covered with the moiré structure. Therefore, this area is believed to be a clean Ir(111) patch. However, by analyzing

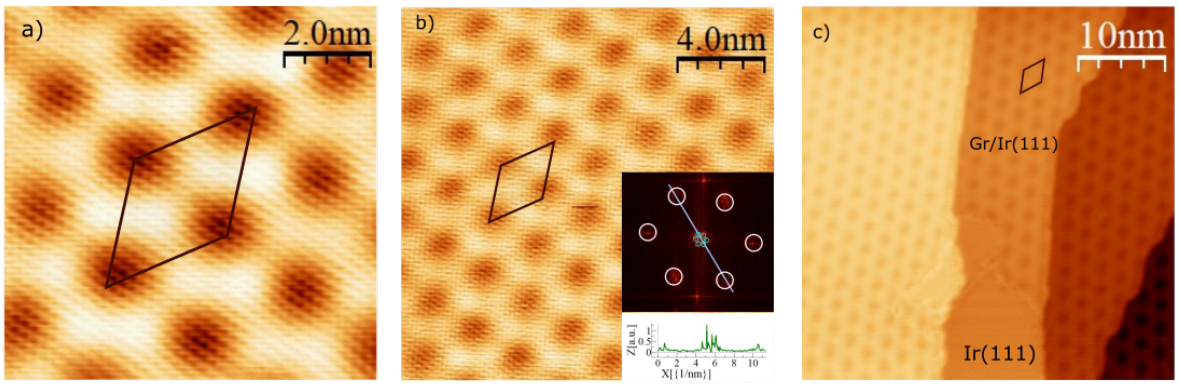

Figure 6.4: STM images of graphene on Ir(111) (the high-coverage sample). Black rhombus denote the moiré unit cell. a) Moiré structure and atoms are visible. Scanning parameters: It: -0.920 nA, Vt:-2.4 mV. b) Moiré structure and atoms again visible. Inset show fast fourier transform. Scanning parameters: It: -0.350 nA, Vt: -2.4 mV. c) The moiré structure, step edges, and a small patch of bare Ir(111) are visible. Scanning parameters: It: 0.350 nA, Vt: 57.1 mV.

larger-area images, which are presented in Appendix A.x, one can assume that only small areas of the surface could consist of bare Ir(111) patches. The different color-scale areas observed in figure 6.4a) correspond to the step edges of the Ir(111) substrate.

XPS analysis

The XPS O1s and C1s spectra prior to oxygen exposure are shown in the lower parts of figure 6.5a) and b), respectively. The purple dots are the raw data, the green curve is the fit and the grey line is the background. Each peak represents carbon or oxygen atoms in a particular type of chemical environment. All peaks and the fitting procedure are summarized in table 6.3 and 6.4.

In the O1s spectra, the following contaminants was be observed: O_1 (533.60), O_2 (532.10 eV), O_3 (531.20 eV) and O_5 (528.80 eV) and was be attributed to hydroxyl (O_1), ethers (O_2), enolate groups (O_3), and epoxy and carbonyl groups (O_5), respectively [8, 85]. These peaks were also observed for the low-coverage sample prior to the oxygen dose.

In the C1s spectra, the sp^2 carbon component, C_4, was prominent before oxidation and positioned at 284.08 eV in agreement with literature [8]. The Ir4d peak originates from diffraction of the photons coming from the x-ray source. Smaller sp^3 components, namely C_1 (285.90 eV), C_2 (285.20 eV), and C_3 (284.60 eV) are present on the sample, and can be attributed to carbonyl groups or a small amount of epoxy groups, ethers and enolate groups, respectively [8, 85]. The sp^3/sp^2 ratio is 0.52 prior to oxygen exposure. The C_5 peak is attributed to the graphene sheet becoming decoupled from Ir(111) substrate due to oxygen intercalation [84].

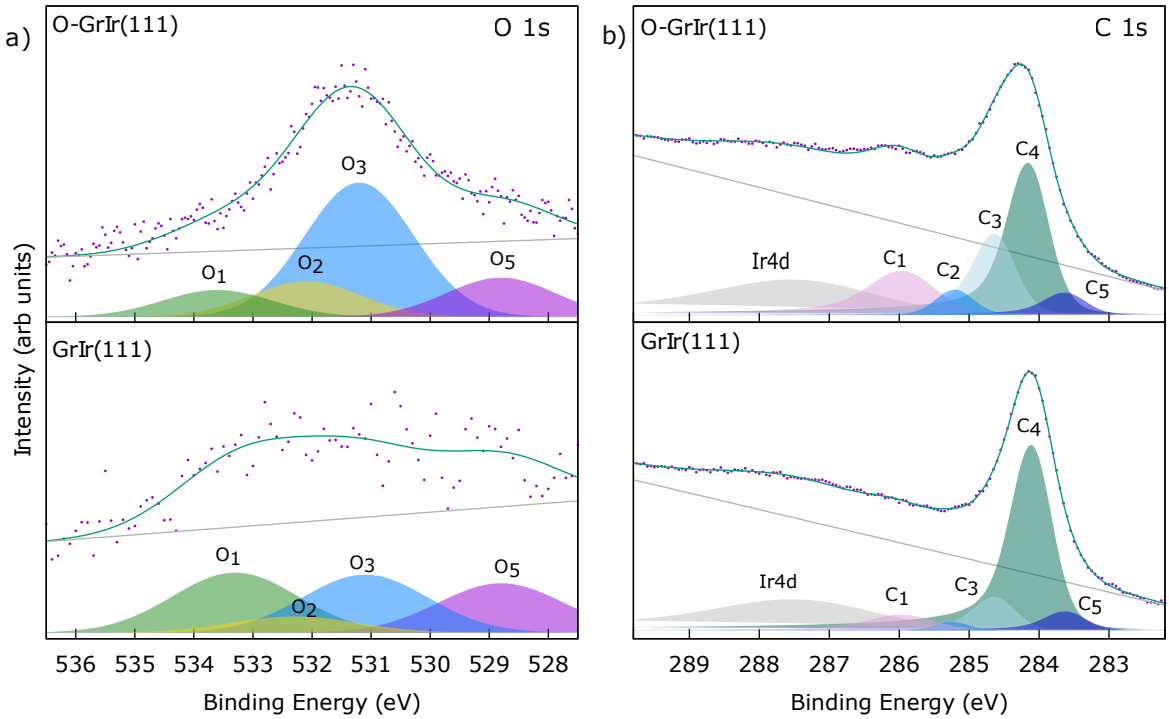

Figure 6.5: XPS a) O1s and b) C1s spectra for samples prior (lower) and after (upper) low atomic oxygen exposure.

Table 6.3: XPS O1s peaks and fitting parameters summarized for the high-coverage sample. The peaks are fitted using Gaussian function with a linear background. See section 4.2.2 for explanation behind fitting procedure. BE stands for binding energy and GFWHM Gaussian full width half maximum.

Component	**BE (eV)**	**GFWHM (eV)**	**Assignment**
	O-Gr/Ir(111)		
O_1	533.60	2.17	C-OH [120]
O_2	532.10	2.17	C-O-C [85]
O_3	531.20	2.17	C-O [8]
O_5	528.80	2.17	C=O [8]
	Gr/Ir(111)		
O_1	533.30	2.50	C-OH [120]
O_2	532.20	2.50	C-O-C [85]
O_3	531.10	2.50	C-O [8]
O_5	528.80	2.50	C=O [8]

Table 6.4: XPS C1s peaks and fitting parameters summarized for the high-coverage sample. The peaks are fitted using Doniach-Šunjić function convoluted with a Gaussian, and a linear background. See section 4.2.2 for explanation behind fitting procedure. BE stands for binding energy, GFWHM and LFWHM for Gaussian and Lorenzian full width half maximum respectively and asym for the asymmetric fraction allowed.

Component	**BE (eV)**	**GFWHM (eV)**	**LFWHM (eV)**	**Asym**	**Assignment**
			O-GrIr(111)		
Ir4d	287.36	2.30	0.50	0.12	Ir4d
C_1	285.90	0.90	0.28	0.12	C=O [8]
C_2	285.20	0.70	0.07	0.00	C-O-C [85]
C_3	284.60	0.60	0.14	0.07	C-O [8, 85]
C_4	284.12	0.60	0.14	0.10	C-C [8]
C_5	283.58	0.60	0.14	0.05	Decoupled graphene [84]
			GrIr(111)		
Ir4d	287.30	2.30	0.50	0.12	Ir4d
C_1	285.90	0.90	0.08	0.04	C=O [8]
C_2	285.25	0.58	0.01	0.00	C-O-C [85]
C_3	284.60	0.60	0.14	0.11	C-O [8, 85]
C_4	284.08	0.60	0.14	0.10	C-C [8]
C_5	283.59	0.60	0.14	0.00	Decoupled graphene[84]

6.2.2 Oxidized Graphene on Ir(111)

STM analysis

STM images of O-Gr/Ir(111) are shown in figure 6.6. A high density of defects is observed in all images. An FFT of the image in figure 6.6c) is shown as the inset (the full FFT image can be found in Appendix A.1.1). Since graphene atoms are not visible in the STM image, only the hexagonal arising from the moiré structure is visible in the FFT image. Measurement of the hexagonal reveals a lattice constant of 2.50 ± 0.05 nm, in agreement with the moiré lattice constant measured prior to oxygen dose. Hence, the moiré structure is intact after the oxygen dose.

The enolate group is the dominant functional group after atomic oxygen exposure and can only be configured at FCC/HCP sites [8] (see section 3.2.1 for details). Therefore, the darker circular holes are believed to be unreacted ATOP sites (i.e. bare graphene) arising from the moiré structure of graphene on Ir(111) surface. The moiré unit cell is shown as a black rhombus in figure 6.6b). As such, the ring-like defects/oxygen clusters observed for the low-coverage sample, have now have merged to form bright, elongated structures [71, 123]. The STM images suggest a coverage close to saturation [123].

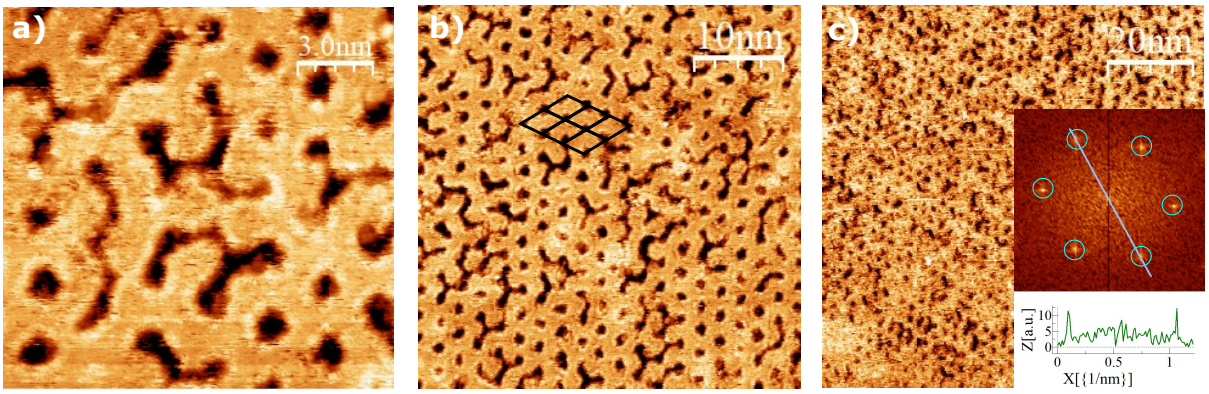

Figure 6.6: STM images of sample after oxygen dose for 4 minutes. a) Scanning parameters: It: 0.150 nA, Vt: 475.8 mV, b) Scanning parameters: It: 0.150 nA, Vt: 475.8 mV. c) Scanning parameters: It: 0.420 nA, Vt: 396.4 mV.

XPS analysis

The XPS O1s and C1s spectra after oxygen exposure are shown in the upper parts of figure 6.5a) and b), respectively. The purple dots are the raw data, the green curve is the fit and the grey line is the background. Each peak represents carbon or oxygen atoms in a particular type of chemical environment. All peaks and the fitting procedure are summarized in table 6.3 and 6.4.

After oxidation, a main component of the O1s spectrum arises at 531.2 eV (O_3). This peak is in good agreement with previous studies [85], and can be assigned to enolate groups [8]. Other components, O_1 (533.60), O_2 (532.10 eV), and O_5 (528.80 eV), are present on the surface and can be attributed to hydroxyl, ethers, epoxy and carbonyl groups respectively [8, 85].

C_4 is still prominent whereas other components have grown. The sp^3/sp^2 ratio is now 0.91. It should be noted, that from the literature the enolate peak (C_3) is expected to be shifted +0.24 eV - 0.46 eV with respect to the sp^2-peak [8, 85]. However, the laboratory XPS can not resolve two different peaks in this range. Thus, parts of the enolate peak might be unresolvedly embedded in the sp^2-peak, and any exact estimation of coverage is therefore challenging. The binding energy of the C-Ir bond, which arises when enolate groups are formed, is assumed to have exactly the same binding energy as the C-O enolate bond [8, 123], and is thus is not visible in the C1s spectrum.

6.2.3 Summary

After graphene growth, the sample was scanned on two random regions on the surface with micrometers spacing. With a very small amount of defects, the sample was judged of good quality. Notably, evidence of a small patch of bare Ir(111) was observed on the sample. As this was not observed on large-area images, this was believed to only exist on a small percentage of the surface.

After oxygen exposure, two different areas on the sample with micrometer spacing were scanned on. The STM images suggest a coverage close to saturation. It is a possibility that the removal of hydrogen contaminants in the dosing chamber prior to oxygen dose (by annealing) makes the surface more receptive to enolate groups forming on the graphene surface (in comparison to the low-coverage sample, which was not annealed prior to oxygen dose). As such, if the experiments were to be re-done, annealing prior to oxygen dose after transportation is highly recommended.

6.3 Corrugation Analysis of the Samples

The wetting and icing properties of a coating have shown to be dependent on the surface roughness (see section 2.2.3 and section 2.3.3 for details). The recorded signal of an STM image is a function of the electronic properties and the geometric properties of the sample surface. The therm *corrugation* will here be used as a convolution between the electronic structure and the geometric roughness.

On a functionalized graphene surface, mainly three factors contribute to the corrugation of a

surace; i) oxygen clusters, ii) step-edges of the Ir(111) crystal, and iii) wrinkles of graphene occurring during growth (see 3.2 for details). STM images for the Gr/Ir(111) samples are used to measure the global RMS corrugation, C_{RMS}, of wrinkles and step edges. The C_{RMS} of the locally rough O-Gr is measured on images collected after oxidation and do not include step edges or wrinkles. The function called "roughness analysis" in WsXM [117] was used to calculate the root mean square corrugation of the STM images. The results are presented in table 6.5. The images used for the roughness analysis are included in Appendix A.1.4.

Table 6.5: STM measured corrugation of the surface.

	O-Gr/Ir(111) Low-Coverage	O-Gr/Ir(111) High-Coverage	Gr/Ir(111) Step Edges	Gr/Ir(111) Wrinkles
C_{RMS}	0.13 Å $\pm$ 0.08 Å	0.49 $\pm$ 0.01 Å	0.19 nm $\pm$ 0.07 nm	0.8 nm $\pm$ 0.5 nm

The results presented in table 6.5 show that the sample corrugation is rather smooth. The wrinkles contribute the most to the global corrugation of the surface, and the local corrugation increase with oxygen coverage. Surface features in the nanometer range have been reported to affect the macroscopic WCA [26] by the so-called "pinning" effect, which results in metastable WCA (see section 2.2.3 for details). Other studies suggest that the wetting properties of smooth surfaces are mainly dictated by the chemical properties of the surface rather than rough surface features in the nanometer range [124, 29]. Assuming that a critical ice embryo has radius $\sim$1.7 nm at -25°C [9], the corrugation is $C_{RMS} < 10r_c$ and thereby the free nucleation energy barrier is to be affected by the classical nucleation theory (see section 2.3.2 for details). However, Eberle et al. [9], studied icing as a function of surface texturing, and found that the freezing onset temperature of surfaces with an RMS roughness size of 0.1 - 100 nm is constant (-24°C) regardless of surface chemistry. Due to the contradictions in literature, it is unclear if and to what degree the surface roughness affects the wetting and icephobic properties.

Note that STM images used for these calculations have a surface area of maximum 300 nm^2, such that features rougher than this will not be detected. Additionally, the electronic structure varies with the scanning parameters used. Hence, STM is not the best-applied tool to analyze the geometrical roughness of a surface. For future reference, techniques such as atomic force microscopy (AFM) is more applied for geometrical roughness analysis and should be considered used [125]. Lastly, note that these images were collected in ultra-high vacuum prior to air exposure, so that dust and air contaminants that might sit on the samples during the icing experiments were not detected here.

6.4 Wetting and Icing Experiments

WCA and freezing temperature onset measurements were collected using droplets deposited i) at the center of the sample, and ii) at the edges of the sample. The freezing delay measurements were done in the center of the sample. Prior to the wetting and icing experiments, the sample was characterized by STM and XPS. This analysis focused on characterizing the center of the sample, which is standard with STM/XPS. Therefore, the wetting and icing experiments mainly focus on the center of the sample. However, XPS spectra recorded after the icing experiments (discussed in section 6.5.2) included analysis of an edge and revealed that the chemistry environment looks different at the edge versus at the center of the sample. An analysis of the wetting and icing experiments with respect to the chemical environment the droplets where deposited are discussed in section 6.6

6.4.1 Water Contact Angle (WCA)

Images of a sessile water droplet (2 μl) on the O-Gr/Ir(111) samples in liquid and solid phase are presented in figure 6.7. As evident from the left panel, both the low-coverage and the high-coverage sample O-Gr/Ir(111) was found to be close to hydrophobic at room temperature. The WCA of droplets deposited at the center was $71^\circ \pm 5^\circ$ (three cycles, five measurements each) for the low coverage sample and $77^\circ \pm 6^\circ$ (four cycles, five measurements each) for the high-coverage sample. The results are presented and summarized in table 6.6. Notably, the WCA of droplets deposited at the center do not differ from what is measured at the edge of the sample. The WCA for both samples are significantly larger than that experimentally reported on graphene oxide (25° - 55°) [101, 102, 103, 104], except from when carboxyl groups have been removed (70°) [105]. The wetting transparency of a graphene coating is highly debated in literature [90] (see section 3.4 for details). However, possible wetting transparency of functionalized graphene has so far not been discussed. Göbbels et al. found that the WCA of iridium increases with oxygen content starting at $\sim 82^\circ$ for bare iridium with an RMS roughness of 1.2 nm [126]. The WCA of bare iridium overlap with the WCA measurements on O-Gr/Ir(111) high-coverage sample. Thus, the possibility that the wetting properties of oxidized graphene are fully or partially transparent to the substrate should be considered.

Another possible explanation of the low wettability is i) airborne contamination and ii) vacancies defects. Firstly, airborne hydrocarbons have been reported to increase the WCA of pristine graphene after only 15 minutes [97, 98]. Secondly, line and point defects have been theoretically demonstrated to increase the WCA of graphene oxide [127]. Surface analysis (STM and XPS) of the sample conducted after the icing experiments, reveals both an increase in the number of vacancies defects on the sample (damaged graphene) and the presence of organic dust (including

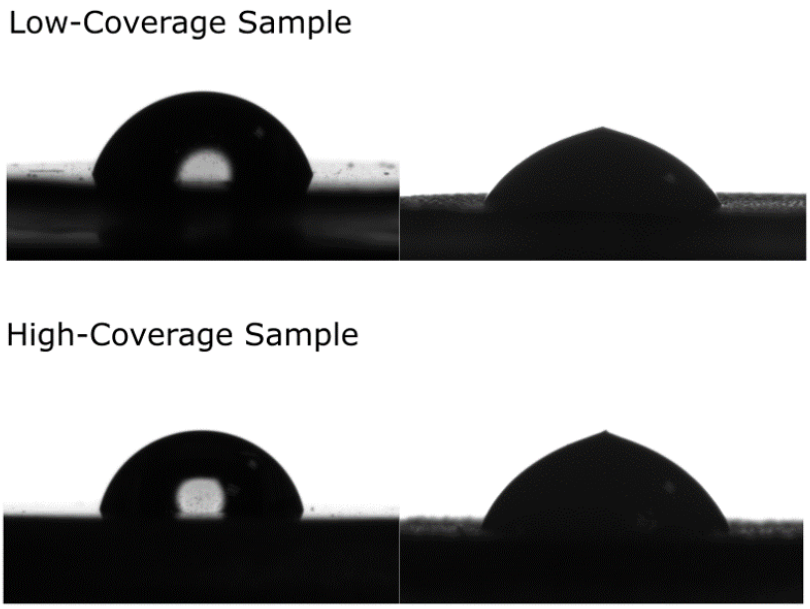

Figure 6.7: Snapshots of a sessile water droplet (2 μL) at room temperature (left) and the droplet in a frozen state (right).

hydrocarbons) which could explain the observed wettability. These findings will be discussed in section 6.5.

6.4.2 Freezing Onset Temperature

The freezing onset is assumed to mark the start of the freezing process (see section 6.4.2 for details). In this thesis work, the freezing onset temperature was identified by a sudden change in the droplet appearance (it turns hazy) and a subsequent $\sim$ 0.5°C temperature rise of the crystal.

The freezing onset temperature (T_O) results are presented in table 6.6. The raw data collected at the center of the sample are plotted in figure 6.8. At the center of the sample, T_O was found to be -18°C $\pm$ 1°C for the low-coverage sample and -21°C $\pm$ 1°C for the high-coverage sample. Thus, T_O decreases with increasing oxygen coverage, which is the same trend observed for fluorinated graphene [37].

The freezing onset temperature is quite close to that of graphene oxide on silicon (down to -24.6°C) [107] and to that of fluorinated graphene on Ru(0001) on sapphire [37], where Akhtar et al. [37], reported a freezing onset temperature of -23 °C $\pm$ 1°C (estimated 25 % fluorine coverage on graphene on Ru(0001) on sapphire), -20 °C $\pm$ 1°C (estimated 10 % fluorine coverage on graphene on Ru(0001) on sapphire) and -18 °C $\pm$ 1°C (graphene on Ru(0001) on sapphire). A theoretical study predicted that functionalization (Na^+-, Cl^--ions, and CH_4) of graphene lowers the freezing onset temperature due to the formation of a viscous water layer on the surface [51].

The observed freezing onset temperature indicates that enolate-functionalized graphene exhibits similar properties, although not as efficiently as water confined between graphene oxide sheets has been predicted to be [7].

Hence, in comparison to the WCA results, it is possible that O-Gr is transparent to wetting, but not to icing. In other words, enolate and other functional groups of O-Gr inhibit the freezing of water through the formation of a viscous water layer, but the wettability is determined by the underlying Ir(111) substrate.

Table 6.6: Freezing onset temperatures measured on the low-coverage sample and the high-coverage sample, respectively.

	Low-Coverage				High Coverage			
	T_O	No.	WCA	No.	T_O	No.	WCA	No.
Center	-18°C ± 1°C	9	71° ± 5°	23	-21°C ± 1°C	26	77° ± 6°	36
Edge	-16°C ± 2°C	5	72° ± 5°	16	-18°C ± 1°C	5	79° ± 3°	5

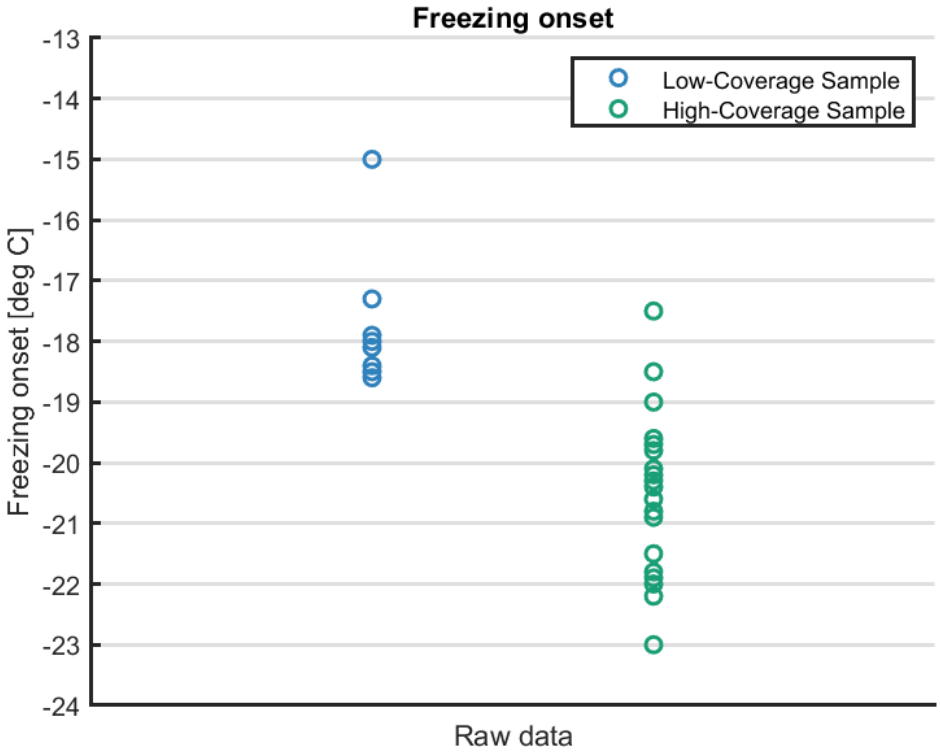

Figure 6.8: Freezing onset temperatures for the low-coverage sample (blue) and the high-coverage sample (green). All measurements are collected in at the center of the sample

6.4.3 Freezing Delay

The freezing delay measurements for the low-coverage sample (blue) and the high-coverage sample (green) are plotted in figure 6.9. For both samples, the freezing delay measurements were measured in the center of the sample by cooling a sessile water droplet (volume of droplet) down to a certain subzero temperature (-5°, -10°, -15°). The results show freezing delays up to 90 minutes at -5°C, 86 minutes at -10°C and 11 minutes at -15°C.

However, as seen in figure 6.9, there is a large spread in the measured data. For example, for the high-coverage sample, the freezing delay at -10°C is reported to be 83 minutes as the longest and 6 minutes as the shortest. A similar spread was not observed for the freezing onset temperature data.

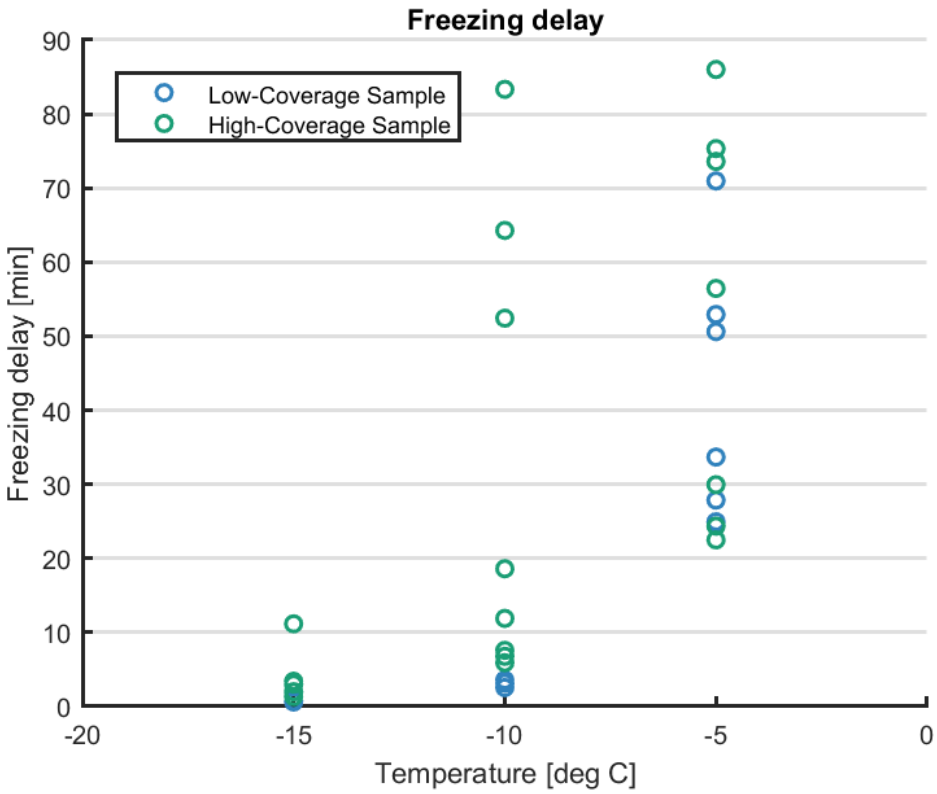

Figure 6.9: The freezing delay measurements for the low-coverage sample (blue) and the high-coverage sample (green). All measurements are conducted in the center of the sample.

During the experiments for both samples, dust and small hairs were noticed on the sample via the optics as shown in figure 6.10. The concentration of dust seemed to increase with time. Any foreign body can act as possible nucleation sites for the droplet and can thereby dictate the heterogeneous freezing process. For the ending freezing delay measurements on the high-coverage sample, hair and particles were attempted removed by i) blowing with an air gun, ii) depositing and picking up large droplets on the sample (in order to suck up any dust particles), and iii) increasing the temperature of the crystal to 50°C to ensure evaporation of the droplet and

to avoid using the non-hairy tissues. When employed together, the methods seemed to help to some degree to keep the sample clean over time, but no decrease in the measurement spread was observed.

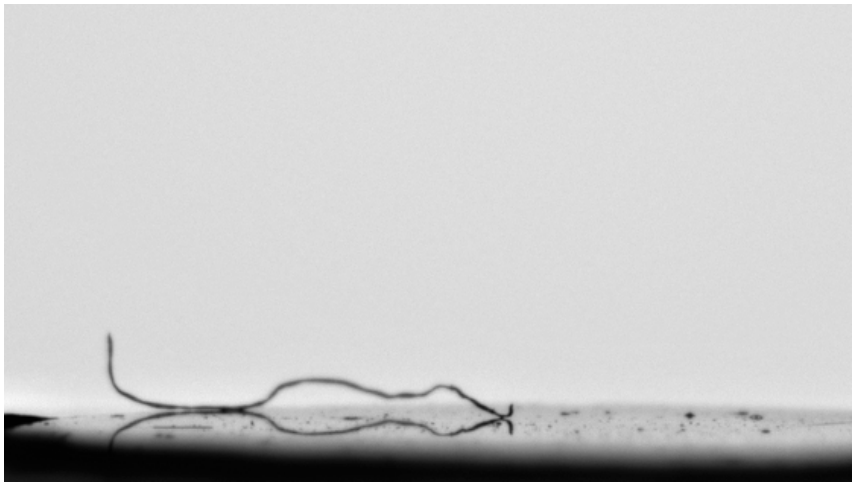

Figure 6.10: Dust and hair was observed on the sample surface that was not detected by the bare eye, but detected via the optics.

6.4.4 Summary

Both samples are close to hydrophobic at room temperature with a WCA of $71^\circ \pm 5^\circ$ (low-coverage sample) and $77^\circ \pm 6^\circ$ (high-coverage sample). The observed WCA is significantly larger than what is reported on untreated graphene oxide. The observed wettability is discussed in relation to the possibility of wetting transparency, adsorption of airborne contamination, and concentration of vacancy defects.

The freezing onset temperature is measured and showed to be -18°C $\pm$ 1°C for the low-coverage sample and -21°C $\pm$ 1°C for the high-coverage sample, thus the freezing onset decrease with increasing oxygen coverage. O-Gr may be transparent to wetting properties, but not to icephobic properties.

Dust and foreign particles seemed to be disturbing to the freezing delay measurements, but not influence the freezing onset measurements. These bodies are possible nucleation sites and could expedite the freezing nucleation process, thus leading to a large spread of the measurement data.

6.5 Surface Science Characterization Post Icing Experiments

Based on the results from the wetting and icing experiments and due to time limitation, it was decided to only conduct post icing atomic level experiments on the high-coverage sample.

6.5.1 STM investigation

STM images of the high-coverage sample collected after the icing experiments are shown in figure 6.11. In figure 6.11a), a bright, elongated pattern can be observed and is shown with a blue arrow. The shape of this pattern is comparable to the darker elongated structure observed prior to the icing experiments (figure 6.6). The change in color contrast is due to the different scanning parameters used. Additionally, ring-like defects (as discussed in section 6.1.1) are observed, highlighted with a white arrow. These may correspond to defects, likely induced by the exposure to air or water droplets during the icing experiments as they were not observed prior to wetting and icing experiments. The FFT image is shown as the inset (the full image can be found in appendix A.1.1), where the opposing maxima (shown with light blue circles) correspond to the moiré superstructure (discussed in more detail in section 3.2.1). The moiré lattice constant was found to be 2.53 nm $\pm$ 0.03 nm. Hence, on this area of the surface, the moiré structure remains intact after ice experiments.

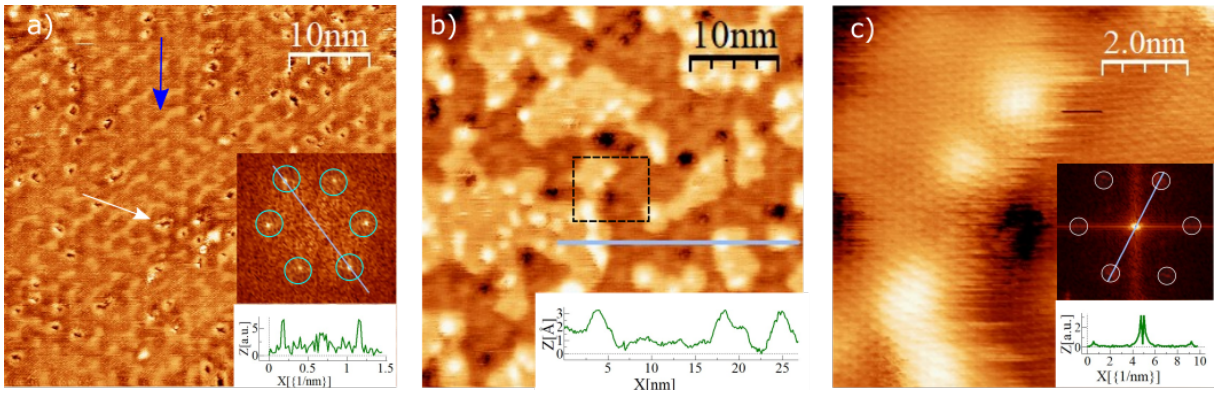

Figure 6.11: STM images collected after icing experiments. a) A bright, elongated pattern is observed and shown with a blue arrow. The white arrow highlights defects. Scanning parameters: -440 pA, Vt: -38.8 mV. Inset: FFT and height profile which shows the line spacing of the moiré structure. b) An STM image collected on a different area than a), showing white elevated areas. The inset shows the height scan of the line drawn across the image. Scanning parameters: 470 pA, Vt: 38.8 mV c) An atomically resolved scan of the area marked with black rectangle in b). Scanning parameters: It: -440 pA, Vt: 38.8 mV. Inset: FFT of the image and height profile to show the distance between maxima.

Figure 6.11b) shows a different area of the surface with an interesting structure of white elevated areas, not seen prior to icing experiments. On top of the elevated areas, brighter dot-like structures

are visible. A line is drawn across the surface where the height profile is shown as the inset, revealing a height difference of $\sim$1 Å for the elevated areas and further $\sim$1 Å increase for the dot-like structure on top of the elevated islands.

An atomically-resolved image collected from the area inside the black rectangle in b) is shown in c). The FFT is shown as the inset (the full image can be found in Appendix A.1.1). This image reveals a hexagonal pattern of graphene atoms that lie on top of the white elevated areas. The STM images seen in 6.11b) and c) look strikingly similar to STM images reported in literature for water intercalated beneath graphene sheets on Ru(0001) [128], Pt(111) [129] and Au [130]. It is suggested that water is not uniformly distributed underneath graphene, and the brighter dot-like structure corresponds to a second layer of water intercalated beneath the graphene sheets [128, 130]. The height difference (visible as the inset in 6.11b) between elevated areas and elsewhere, agrees to that reported for intercalated and non-intercalated areas ($\sim$1 Å for one layer of water) [128].

The dark circular holes in figure 6.11b) and c) can be attributed to defects, corresponding to the ring-like defects observed in 6.11a). These defects are likely induced during the wetting and icing experiments. The fact that graphene is visible in figure 6.11c) implies that oxygen-containing functional groups are lost in intercalated regions following air, water, and ice exposure.

It is important to consider how potential intercalation can occur. Recently, He et al. predicted theoretically that graphene edges could easily be saturated by hydrogen through the decomposition of H_2O [131]. When the graphene edge is saturated, the graphene sheet is decoupled from the Cu substrate and H_2O can migrate toward the interface (by overcoming a barrier of 0.49 eV). Because of the relatively low energy barrier, these reactions can be completed at room temperature. Figure 6.6c) in section 6.1.2 evidenced an area of a bare Ir(111) patch. Thus, it is likely that graphene edges on bare Ir(111) areas have provided routes to intercalation with relatively low energy barriers under air exposure and/or icing experiments. Along with graphene edges, line defects such as grain boundaries or vacancies are also suggested to be an entrance for intercalation. Grain boundaries are reported to be sites susceptible to water splitting [128], but the effect has only been studied/observed in a high vacuum. Generally, little research has been done on intercalation due to water and air exposure under ambient conditions with a realistic level of humidity, and this could be a topic for future research.

6.5.2 XPS investigation

The sample was investigated with XPS first using the laboratory source and then by using a synchrotron as the x-ray source. In the laboratory source, the photons access energy of 1250 eV and the spot size (elliptical) is 1-2 cm^2. The laboratory source was used to collect data i) with

normal emission, ii) grazing emission (a more surface-sensitive method) and finally iii) with normal emission from the edge of the sample to see if there is any difference of the chemical environments of the atoms on the edge versus the center.

The synchrotron generates photons with photon energy ranging from 20 eV to 700 eV and is therefore a more surface-sensitive technique. Moreover, the synchrotron generates a 0.5-1.5 mm^2 elliptical spot on the sample. The synchrotron was used to first measure the sample i) with normal emission and then ii) with grazing emission.

Laboratory Source XPS

XPS O1s and C1s spectra were collected after icing experiments to investigate if there have been any chemical changes to the sample, and are shown in the three upper parts of figure 6.12a) and b), respectively. The two spectra conducted prior to ice experiments are included for comparison and have been discussed in detail in section 6.2.2. The purple dots denote the data, the green curves denote the fit and the gray lines denote the background. Each peak represents carbon or oxygen atoms in a particular type of chemical environment. All peaks and their fitting parameters are summarized in table 6.7 and 6.8.

In the O1s spectra prior to icing experiments, the O_3 component dominates and is assigned to enolate functional groups [8]. Other components, namely O_1, O_2 and O_5 are also present and can be assigned to hydroxyl, ehters, epoxy and carbonyl groups, respectively [8, 85] (see section 6.2.1 and 6.2.2 for details).

In the O1s spectrum collected after icing experiments with normal emission, the enolate O_3 component is suppressed. In contrast, the ether component (O_2) and the O-Ir component (O_4) dominate the signal. The component assigned to ether can originate from either i) heavily damaged graphene or ii) organic dust sitting on top of the graphene in the center of the sample. The O-Ir component indicates oxygen species (for example O, OH or H_2O) interacting with Ir(111) [84], either intercalated ($Gr/H_2O/Ir(111)$) which would agree with STM images collected (see section 6.5.1), or on bare Ir(111) patches which also agrees with STM images collected after graphene growth (see section 6.2). It is possible that the signal from enolate groups gets buried in the signal from the two more intense peaks (O_2 and O_3).

The grazing angle measurement is more surface-sensitive and does not show ether group to dominate. In contrast, the enolate peak (O_3) becomes prominent whereas O_4 (O-Ir) peak almost completely disappear. One possible explanation is that the grazing angle takes the signal from more of the sample surface, including edges. The O1s spectrum collected from the edge of the sample differs from the spectrum collected from the center of the sample, proving that the chemical environment is not uniform across the surface. On the edge, O_3 and O_4 are more

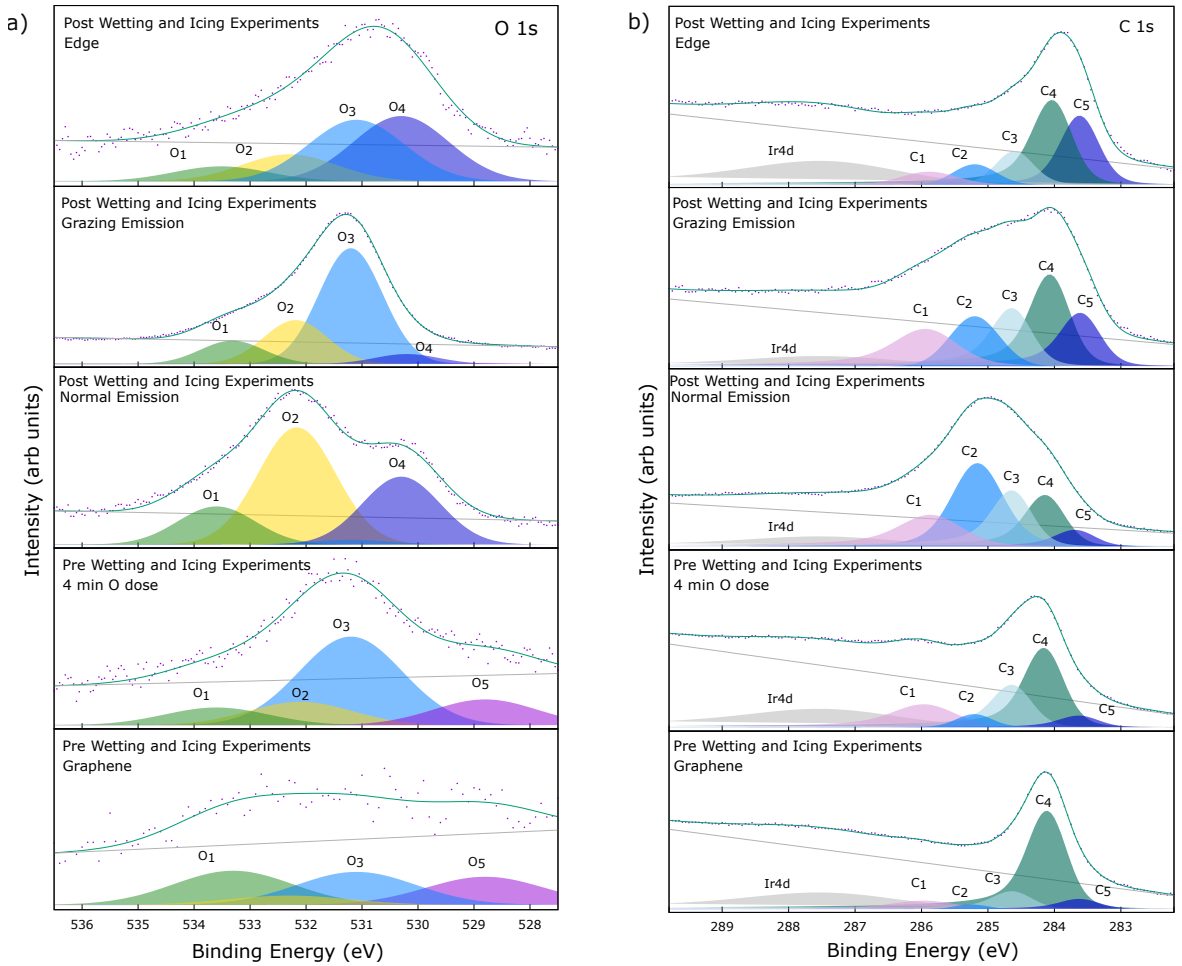

Figure 6.12: XPS a) O1s and b) C1s spectra. From the lower: sample after graphene growth, after oxygen exposure, after icing experiment, after icing experiments measured with grazing emission and after icing experiments measured on the edge of the sample.

prominent peaks showing the presence of C-O (enolate) and O-Ir(111) environments.

In the C1s spectra prior to icing experiments, C_4 is prominent. The other peaks, Ir4d, C_1, C_2 and C_3 can be attributed to Ir4d diffraction, carbonyl (C=O), ether (C-C) and enolate (C-O) groups, respectively [8, 85]. Finally, C_5 can be attributed to areas of graphene that have been intercalated and so are further removed from the Ir surface (decoupled) [84]. See section 6.1.2 for more details.

The C1s spectrum collected with normal emission, shows that most of the signal after icing experiments have shifted by 1 eV to higher binding energy (∼285 eV), indicating the shift from an abundance of sp^2 carbon atoms, prior to ice experiments, to an abundance of sp^3 carbon, after ice experiments. The sp^3/sp^2 peak ratio, where sp^3 is the amplitude of all peaks besides Ir4d and C_4, has now increased to 2.55 (from 0.91). The ether component (C_2) dominates the spectrum. The sudden growth of the ether component agrees with what was observed in the O1s spectrum, and supports the hypothesis of either i) heavily damaged graphene or ii) organic dust sitting on

top of graphene at the center of the sample.

In the spectrum measured with grazing emission, the broad data collection reveals that sp^3 peaks are still dominant, with the sp^3/sp^2 ratio being 3.53. However, the sp^2 peak (C_4) is to some degree recovered. This can again be explained by that grazing emission collects data from a larger area of the sample surface, including the edges. Thus, it looks like there is more intercalated graphene (C_5) on the edges and less sp^3 carbon.

The spectrum collected from the edge supports this hypothesis. First, it shows that the chemical environments of the surface atoms are not uniform across the sample in agreement to what observed for the O1s signal. Second, the presence of the graphene peak and the Gr/O/Ir(111) peak (C_5) agrees well with what observed for the O1s edge spectrum. The sp^3 peaks are less prominent in this spectrum compared to the grazing emission spectrum, implying that there are less organic dust and less damage to graphene on the edge of the sample compared to what was observed at the center of the sample. Additionally, it shows less sp^3 carbon compared to the spectrum from before icing experiments. Hence, there is believed to be less functional groups on the edge after icing experiments and more intercalation. This agrees well with STM images, where intercalation was only visible in less functionalized areas.

Table 6.7: XPS O1s peaks and fitting parameters summarized for the high-coverage sample post ice experiments. The peaks are fitted using Gaussian function with a linear background. See section 4.2.2 for explanation behind fitting procedure. BE stands for binding energy and GFWHM Gaussian full width half maximum.

Component	**BE (eV)**	**GFWHM (eV)**	**Assignment**
O-GrIr(111) Post Ice Experiments Edge			
O_1	533.52	2.00	C-OH [120]
O_2	532.30	2.00	C-O-C [85]
O_3	531.10 (eV)	2.00	C-O [8]
O_4	530.30 (eV)	2.00	O-Ir(111) [84]
O_5	528.80 (eV)	2.00	C=O [8]
O-GrIr(111) Post Ice Experiments Grazing Emission			
O_1	533.32	1.34	C-OH [120]
O_2	532.19 (eV)	1.34	C-O-C [85]
O_3	531.20 (eV)	1.34	C-O [8]
O_4	530.20 (eV)	1.34	O-Ir(111) [84]
O_5	528.80 (eV)	1.34	C=O [8]
O-GrIr(111) Post Ice Experiments Normal Emission			
O_1	533.60	1.64	C-OH [120]
O_2	532.16 (eV)	1.64	C-O-C [85]
O_3	531.20 (eV)	1.64	C-O [8]
O_4	530.30 (eV)	1.64	O-Ir(111) [84]
O_5	528.80 (eV)	1.64	C=O [8]

Table 6.8: XPS C1s peaks and fitting parameters summarized for the high-coverage sample post ice experiments. The peaks are fitted using Doniach-Šunjić function convoluted with a Gaussian, and a linear background. See section 4.2.2 for explanation behind fitting procedure. BE stands for binding energy, GFWHM and LFWHM for Gaussian and Lorenzian full width half maximum respectively and asym for the asymmetric fraction allowed.

Component	**BE (eV)**	**GFWHM (eV)**	**LFWHM (eV)**	**Asym**	**Assignment**
O-GrIr(111) Post Ice Experiments Edge					
Ir4d	287.30	2.30	0.50	0.12	Ir4d
C_1	285.90	0.85	0.03	0.05	C=O [8]
C_2	285.20	0.90	0.04	0.00	C-O-C [85]
C_3	284.60	0.65	0.15	0.00	C-O [8, 85]
C_4	284.00	0.65	0.15	0.10	C-C [8]
C_5	283.63	0.65	0.15	0.07	Decoupled graphene [84]
O-GrIr(111) Post Ice Experiments Grazing Emission					
Ir4d	287.36	2.30	0.12	0.50	Ir4d
C_1	285.87	0.88	0.09	0.11	C=O [8]
C_2	285.21	0.90	0.04	0.00	C-O-C [85]
C_3	284.56	0.65	0.11	0.15	C-O [8, 85]
C_4	284.00	0.65	0.15		C-C [8]
C_5	283.56	0.65	0.15	0.11	Decoupled Graphene [84]
O-GrIr(111) Post Ice Experiments Normal Emission)					
Ir4d	287.36	2.30	0.50	0.10	Ir4d
C_1	285.90	0.74	0.29	0.12	C=O [8]
C_2	285.20	0.80	0.00	0.30	C-O-C [85]
C_3	284.60	0.65	0.15	0.12	C-O [8, 85]
C_4	284.07	0.65	0.15	0.10	C-C [8]
C_5	283.60	0.65	0.15	0.12	Decoupled Graphene [84]

Synchrotron XPS

To get a deeper understanding of the laboratory XPS results, synchrotron radiation was used to produce tunable x-rays. Using x-rays produced by synchrotron radiation are a more surface-sensitive technique mainly for two reasons. First, photon energies (and thereby the mean free path of the photons) can easily be tuned. Second, the energy band that passes the monochromator can be quite small, thus improving the energy resolution in XPS experiments by increasing the monochromaticity of the incoming photon beam.

The XPS O1s and C1s spectra are shown in 6.13a) and b), respectively. The two spectra collected with laboratory XPS are included for comparison. The purple dots denote the data, the green curves denote the fit and the gray lines denote the background. Each peak represents carbon or oxygen atoms in a particular type of chemical environment. All peaks and their fitting parameters are summarized in table 6.9 and 6.10.

The O1s spectrum collected with synchrotron normal emission shows that ether groups (O_2) are dominating at the center of the sample.

The O1s spectrum collected with synchrotron grazing emission looks comparable to that collected with synchrotron normal emission. However, there is a large discrepancy between the synchrotron grazing emission and the laboratory grazing emission. This can be explained by the fact that the laboratory XPS grazing emission probe a larger area of the sample, including the edges, whereas the synchrotron radiation XPS only probe the center of the sample.

In the C1s spectrum collected with synchrotron normal emission, most of the signal occurs at lower binding energy than the signal from laboratory normal emission. It is likely that C_5 arises due to graphene become decoupled from Ir(111) in intercalated areas. The photons produced by the synchrotron XPS is tuned to have lower energy (340 eV for C1s) than the laboratory XPS (1250 eV), and thus the mean free path of the electrons are shorter (see figure 4.3 in section 4.2 for details). Therefore, the synchrotron radiation is more surface-sensitive technique than laboratory XPS, and as such, the C_5 peak becomes more visible. This is further seen in the C1s measurement with synchrotron grazing emission, where C_5 becomes even more prominent because of grazing emission is even more of a surface-sensitive technique.

Thus, a discrepancy between the laboratory XPS and synchrotron XPS is observed and is explained by i) the XPS collected with synchrotron radiation is more surface-sensitive and provides better resolution, ii) the synchrotron XPS collects data from a smaller part of the surface whereas the laboratory grazing emission XPS collects data form the whole sample surface, including the edges.

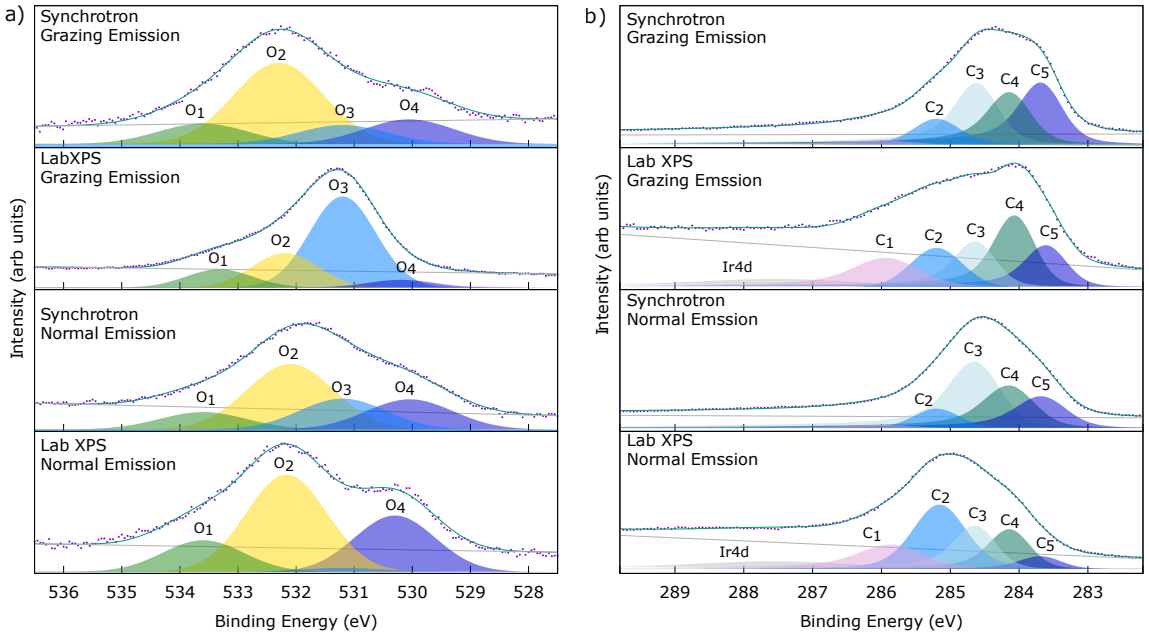

Figure 6.13: XPS O1s (left) and C1s (right) data from synchrotron and laboratory XPS.

Table 6.9: XPS O1s synchrotron peaks and fitting parameters summarized. The peaks are fitted using Gaussian with linear background. See section 4.2.2 for explanation behind fitting procedure. BE stands for binding energy and GFWHM Gaussian full width half maximum.

Component	**BE (eV)**	**GFWHM (eV)**	**Assignment**
Post Ice O-Gr/Ir(111) high-coverage - Grazing Emission			
O_1	533.60	1.82	C - OH [120]
O_2	532.30 (eV)	1.82	C-O-C [85]
O_3	531.20 (eV)	1.82	C-O [8]
O_4	530.06 (eV)	1.82	O-Ir [84]
O_5	528.80 (eV)	1.82	C=O [8]
Post Ice O-Gr/Ir(111) high-coverage - Normal Emission			
O_1	533.60	1.76	C-OH [120]
O_2	532.10 (eV)	1.76	C-O-C [85]
O_3	531.20 (eV)	1.76	C-O [8]
O_4	530.04 (eV)	1.76	Decoupled graphene [84]
O_5	528.80 (eV)	1.76	C=O [8]

Table 6.10: XPS C1s synchrotron peaks and fitting parameters summarized. The peaks are fitted using Doniach-Šunjić function convoluted with a Gaussian, and a linear background. See section 4.2.2 for explanation behind fitting procedure. BE stands for binding energy, GFWHM and LFWHM for Gaussian and Lorenzian full width half maximum respectively and asym for the asymmetric fraction allowed.

Component	**BE (eV)**	**GFWHM (eV)**	**LFWHM (eV)**	**Asym**	**Assignment**
Post Ice O-Gr/Ir(111) high-coverage - Grazing Emission)					
C_1	285.86	0.50	0.01	0.12	C=O [8]
C_2	285.10 - 285.20	0.65	0.29	0.00	C-O-C [85]
C_3	284.57	0.55	0.26	0.12	C-O [8, 85]
C_4	284.10	0.55	0.26	0.12	C-C [8]
C_5	283.64	0.55	0.26	0.12	Decoupled graphene [84]
Post Ice O-Gr/Ir(111) high-coverage - Normal Emission					
C_1	285.80	0.55	0.00	0.12	C=O [8]
C_2	285.20	0.69	0.15	0.00	C-O-C [85]
C_3	284.60	0.68	0.23	0.12	C-O [8, 85]
C_4	284.1	0.68	0.23	0.12	C-C [8]
C_5	283.62	0.68	0.23	0.12	Decoupled graphene [84]

6.5.3 Summary

Mainly, one can argue for three occurrences: i) the graphene is heavily damaged at the center of the sample where the majority of icing experiments were preformed on the high-coverage STM sample, ii) there are organic dust on the sample contributing a lot of sp^3 carbon to the XPS signal and iii) oxygen species interacting with Ir surface atoms, either intercalated or on bare Ir(111) patches. The latter show significant more signal on the edges of the sample (edge and grazing emission with the laboratory XPS).

STM images were only recorded on the center of the sample but show at least two different types of regions i) intercalated or ii) heavily defected. This demonstrates the heterogeneity of the sample.

Notably, intercalated areas were observed to have less functional groups, hence less sp^3 carbon which was further observed with the XPS data.

6.6 The Icing Results in the light of Post-Ice Sample Characterization

Before the icing experiments, both samples were only characterized at the center of the sample because of the experimental set-up. It was assumed that the samples were more or less uniform across the surface.

However, the surface science analysis of the high-coverage sample collected after icing experiments reveals that the sample does not look uniform across the surface. At the center of the sample, highly functionalized areas with presumably damaged graphene and hydrocarbons seem to dominate. The majority of the wetting and icing measurements on the high-coverage samples were completed at the center and might have damaged the sample. Contrary, bare Ir(111) patches and intercalated areas with less functional groups seem to dominate at the edges. Bare Ir(111) patches likely occurred during growth. It is unknown when intercalation occurred, and whether it is a result of air, water, and/or ice exposure.

The wetting and icing measurements can be studied in relation to the heterogeneity of the sample. The nucleation temperature was found to be significantly lower at the center of the sample versus at the edges of the sample. This finding indicates that highly-functionalized areas with damaged graphene (e.g. vacancies) and organic dust (e.g. hydrocarbons) lower the ice nucleation temperature compared to areas where both intercalated graphene (with fewer functional groups) and bare Ir(111) patches dominate. In contrast, no difference could be found for the WCA, which reinforces the hypothesis of O-Gr being transparent to wetting but can prevent ice nucleation.

These findings are summarized in figure 6.14.

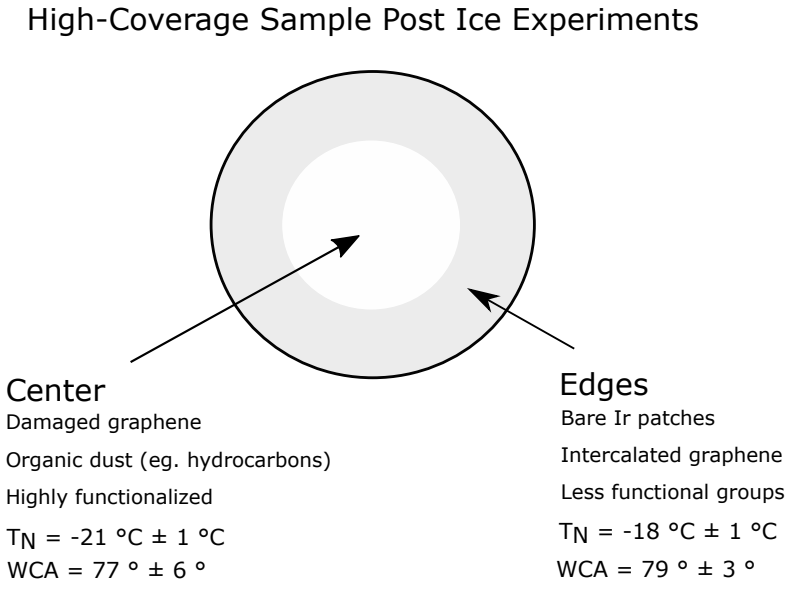

Figure 6.14: A schematic illustration of the high-coverage sample post icing experiments together with the icing results.

Chapter 7

Conclusion and Outlook

The objective of this thesis work has been to perform the first investigation of wetting and icing properties of oxidized graphene on Ir(111). Two samples with low ($\sim$ 8 %) and high (saturated) oxygen coverage were prepared and characterized in ultra-high vacuum by scanning tunneling microscopy and x-ray photoelectron spectroscopy. The wetting and icing properties were studied by measuring the WCA, freezing onset temperatures, and freezing delay times. Finally, the high-coverage sample was investigated by STM and XPS to see if the sample deteriorate during air, water, and ice exposure.

The surface is found to be almost hydrophobic at room temperature with WCA $71^\circ \pm 5^\circ$ for the low-coverage sample and WCA $77^\circ \pm 6^\circ$ for the high-coverage sample. The observed WCA is similar to that reported for iridium, and significantly larger than what is reported on untreated, standard graphene oxide with hydroxyl- and epoxy groups, which is hydrophilic. As such, the observed WCA is argued to be caused by wetting transparency but is also discussed with respect to adsorption of airborne contaminants, and intercalation of water and/or oxygen. The WCA did not change significantly over a period of five days.

The freezing onset temperature is found to be -18°C $\pm$ 1°C for the low-coverage sample and -21°C $\pm$ 1°C for the high-coverage sample and thus, the freezing onset temperature decrease with increasing oxygen coverage. The results indicate that enolate-functionalized graphene exhibits the icephobic properties theoretically predicted for functionalized graphene and experimentally demonstrated for fluorinated graphene, namely a lowering of the freezing onset temperature compared to that of bare graphene. This lowering can be contributed to the formation of a viscous water layer on the surface, which directly inhibits ice nucleation in accordance with heterogeneous ice nucleation theory. This suggests that O-Gr on Ir(111) is transparent to wetting, but not to icing properties.

The freezing delay measurements showed a large spread in the data, possibly explained by dust

and other contaminants present on the sample. It is clear from the nucleation theory that foreign bodies (such as the observed dust particles) can act as possible nucleation sites for the droplet and can thereby dictate the heterogeneous freezing process.

After the icing experiments, the STM images and the XPS spectra of the high-coverage sample demonstrate that the chemical environment of the surface changes after exposure to air, water, and ice. The edges of the sample were found to consist mainly of O, OH and H_2O intercalated areas, accompanied by the loss of oxygen-containing functional groups. Bare Ir(111) patches and grain boundaries has been discussed to be possible intercalation routes. Organic dust (e.g. hydrocarbons) and damaged graphene (e.g. ether, vacancies) were found to dominate at the center of the sample, where the majority of the icing experiments were committed. Here, oxygen functionalized graphene areas were also found to be intact. Throughout the sample, some defects were observed to have been induced during the icing experiments.

Interestingly, the freezing nucleation temperature showed a dependency on where the droplet was deposited; the freezing onset temperature was found to be significantly lower at the center of the sample versus the edges. In contrast, the WCA did not depend on the droplet position. This finding reinforces the hypothesis that the O-Gr coating is transparent to wetting properties but suppresses ice nucleation. Additionally, this finding indicates that highly-functionalized areas with damaged graphene with organic dust lower the ice nucleation temperature compared to areas where both intercalated graphene (with fewer functional groups) and bare Ir(111) patches dominate.

The results from this thesis work suggest that oxygen graphene coatings can act as icephobic coatings. However, before applying these findings to industrial applications, more research must be done. It would be of high interest to do similar experiments on Gr/Ir(111) and on bare Ir(111) to verify the wetting transparency of an O-Gr coating. The same wetting and icing measurements should also be considered done in controlled environments (e.g. low pressure) to avoid dust and air-contamination present on the sample. Furthermore, the effect of air, water, and ice exposure on the samples should be studied further. This can be implemented by preparing a similar sample and characterizee before and after the exposure to i) air, ii) cold environment, and iii) water droplet. This would allow for a detailed investigation of when the changes of the sample occur. In particular, it would be of interest to study the stability of enolate groups in these environments. For future reference, if one were to prepare enolate-oxidized graphene, one should be consisted with annealing in the oxygen chamber to remove air contaminants before oxygen dose. Finally, the study of the wetting and icephobic measurement should be considered completed in more detail. This can be done by measuring the WCA hysteresis, ice adhesion, and the long-term durability of a similar sample.

References

[1] J. Laforte, M. Allaire, and J. Laflamme, "State-of-the-art on power line de-icing," *Atmospheric Research*, vol. 46, no. 1-2, p. 143–158, 1998.

[2] P. Irajizad, S. Nazifi, and H. Ghasemi, "Icephobic surfaces: Definition and figures of merit," *Advances in Colloid and Interface Science*, vol. 269, p. 203–218, 2019.

[3] F. Li, X. Jiang, J. Zhao, and S. Zhang, "Graphene oxide: a promising nanomaterial for energy and environmental applications," *Nano energy*, vol. 16, pp. 488–515, 2015.

[4] Y. Wei, Y. Zhang, X. Gao, Z. Ma, X. Wang, and C. Gao, "Multilayered graphene oxide membranes for water treatment: A review," *Carbon*, vol. 139, pp. 964–981, 2018.

[5] S. Basu and P. Bhattacharyya, "Recent developments on graphene and graphene oxide based solid state gas sensors," *Sensors and Actuators B: Chemical*, vol. 173, pp. 1–21, 2012.

[6] J. Hu, Y. Ji, Y. Shi, F. Hui, H. Duan, and M. Lanza, "A review on the use of graphene as a protective coating against corrosion," *Ann. J. Mater. Sci. Eng*, vol. 1, p. 16, 2014.

[7] M. Zokaie and M. Foroutan, "Comparative study on confinement effects of graphene and graphene oxide on structure and dynamics of water," *RSC Advances*, vol. 5, no. 49, p. 39330–39341, 2015.

[8] A. Cassidy, S. Pedersen, H. Bluhm, V. Calisti, T. Angot, E. Salomon, R. Bisson, and L. Hornekær, "Patterned formation of enolate functional groups on the graphene basal plane," *Physical Chemistry Chemical Physics*, vol. 20, no. 45, p. 28370–28374, 2018.

[9] P. Eberle, M. K. Tiwari, T. Maitra, and D. Poulikakos, "Rational nanostructuring of surfaces for extraordinary icephobicity," *Nanoscale*, vol. 6, no. 9, p. 4874–4881, 2014.

[10] S. Jung, M. Dorrestijn, D. Raps, A. Das, C. M. Megaridis, and D. Poulikakos, "Are superhydrophobic surfaces best for icephobicity?," *Langmuir*, vol. 27, no. 6, p. 3059–3066, 2011.

[11] V. Hejazi, K. Sobolev, and M. Nosonovsky, "From superhydrophobicity to icephobicity: forces and interaction analysis," *Scientific Reports*, vol. 3, Dec 2013.

[12] P. Irajizad, A. Al-Bayati, B. Eslami, T. Shafquat, M. Nazari, P. Jafari, V. Kashyap, A. Masoudi, D. Araya, H. Ghasemi, and et al., "Stress-localized durable icephobic surfaces," *Materials Horizons*, vol. 6, no. 4, p. 758–766, 2019.

[13] J. Zhang, *Interfacial Energy*, pp. 1840–1840. Boston, MA: Springer US, 2013.

[14] S. J. Marshall, S. C. Bayne, R. Baier, A. P. Tomsia, and G. W. Marshall, "A review of adhesion science," *Dental Materials*, vol. 26, no. 2, 2010.

[15] D. Quéré, "Non-sticking drops," *Reports on Progress in Physics*, vol. 68, no. 11, p. 2495–2532, 2005.

[16] T. Young, "Iii. an essay on the cohesion of fluids," *Philosophical Transactions of the Royal Society of London*, vol. 95, p. 65–87, 1805.

[17] A. Nakajima, "Design of hydrophobic surfaces for liquid droplet control," *NPG Asia Materials*, vol. 3, no. 5, p. 49–56, 2011.

[18] R. N. Wenzel, "Resistance of solid surfaces to wetting by water," *Industrial & Engineering Chemistry*, vol. 28, no. 8, pp. 988–994, 1936.

[19] A. B. D. Cassie and S. Baxter, "Wettability of porous surfaces," *Transactions of the Faraday Society*, vol. 40, p. 546, 1944.

[20] A. B. D. Cassie, "Contact angles," *Discussions of the Faraday Society*, vol. 3, p. 11, 1948.

[21] A. Marmur, "Wetting on hydrophobic rough surfaces: To be heterogeneous or not to be?," *Langmuir*, vol. 19, no. 20, p. 8343–8348, 2003.

[22] T. Huhtamäki, X. Tian, J. T. Korhonen, and R. H. A. Ras, "Surface-wetting characterization using contact-angle measurements," *Nature Protocols*, vol. 13, no. 7, p. 1521–1538, 2018.

[23] M. Ramiasa, J. Ralston, R. Fetzer, and R. Sedev, "The influence of topography on dynamic wetting," *Advances in Colloid and Interface Science*, vol. 206, pp. 275 – 293, 2014. Manuel G. Velarde.

[24] A. Marmur, C. D. Volpe, S. Siboni, A. Amirfazli, and J. W. Drelich, "Contact angles and wettability: towards common and accurate terminology," *Surface Innovations*, vol. 5, no. 1, p. 3–8, 2017.

[25] K.-Y. Law and H. Zhao, *Surface wetting characterization, contact angle, and fundamentals*. Springer, 2016.

[26] M. Delmas, M. Monthioux, and T. Ondarçuhu, "Contact angle hysteresis at the nanometer scale," *Physical Review Letters*, vol. 106, no. 13, 2011.

[27] J. Eick, R. Good, and A. Neumann, "Thermodynamics of contact angles. ii. rough solid surfaces," *Journal of Colloid and Interface Science*, vol. 53, no. 2, p. 235–248, 1975.

[28] H. Busscher, A. V. Pelt, P. D. Boer, H. D. Jong, and J. Arends, "The effect of surface roughening of polymers on measured contact angles of liquids," *Colloids and Surfaces*, vol. 9, no. 4, p. 319–331, 1984.

[29] C. Extrand and Y. Kumagai, "An experimental study of contact angle hysteresis," *Journal of Colloid and Interface Science*, vol. 191, no. 2, p. 378–383, 1997.

[30] G. R. Wood and A. G. Walton, "Homogeneous nucleation kinetics of ice from water," *Journal of Applied Physics*, vol. 41, no. 7, p. 3027–3036, 1970.

[31] T. M. Schutzius, S. Jung, T. Maitra, P. Eberle, C. Antonini, C. Stamatopoulos, and D. Poulikakos, "Physics of icing and rational design of surfaces with extraordinary icephobicity," *Langmuir*, vol. 31, no. 17, p. 4807–4821, 2014.

[32] R. P. Sear, "Nucleation: theory and applications to protein solutions and colloidal suspensions," *Journal of Physics: Condensed Matter*, vol. 19, p. 033101, Mar 2007.

[33] I. Gutzow and J. Schmelzer, "The vitreous state: thermodynamics, structure, rheology, and crystallization," 2015.

[34] Z. Zhang and X.-Y. Liu, "Control of ice nucleation: freezing and antifreeze strategies," *Chemical Society Reviews*, vol. 47, no. 18, p. 7116–7139, 2018.

[35] J. Mullin, "5 - nucleation," in *Crystallization (Fourth Edition)* (J. Mullin, ed.), pp. 181 – 215, Oxford: Butterworth-Heinemann, fourth edition ed., 2001.

[36] N. H. Fletcher, "Size effect in heterogeneous nucleation," *The Journal of Chemical Physics*, vol. 29, no. 3, p. 572–576, 1958.

[37] N. Akhtar, G. Anemone, D. Farias, and B. Holst, "Fluorinated graphene provides long lasting ice inhibition in high humidity," *Carbon*, vol. 141, p. 451–456, 2019.

[38] G. Malenkov, "Liquid water and ices: understanding the structure and physical properties," *Journal of Physics: Condensed Matter*, vol. 21, no. 28, p. 283101, 2009.

[39] K. Li, S. Xu, J. Chen, Q. Zhang, Y. Zhang, D. Cui, X. Zhou, J. Wang, and Y. Song, "Viscosity of interfacial water regulates ice nucleation," *Applied Physics Letters*, vol. 104, p. 101605, Oct 2014.

[40] M. P. Goertz, J. E. Houston, and X.-Y. Zhu, "Hydrophilicity and the viscosity of interfacial water," *Langmuir*, vol. 23, no. 10, p. 5491–5497, 2007.

[41] D. Richard and D. Quéré, "Bouncing water drops," *Europhysics Letters (EPL)*, vol. 50, no. 6, p. 769–775, 2000.

[42] L. Mishchenko, B. Hatton, V. Bahadur, J. A. Taylor, T. Krupenkin, and J. Aizenberg, "Design of ice-free nanostructured surfaces based on repulsion of impacting water droplets," *ACS Nano*, vol. 4, p. 7699–7707, Sep 2010.

[43] V. Bahadur, L. Mishchenko, B. Hatton, J. A. Taylor, J. Aizenberg, and T. Krupenkin, "Predictive model for ice formation on superhydrophobic surfaces," *Langmuir*, vol. 27, p. 14143–14150, Jun 2011.

[44] T. Verho, J. T. Korhonen, L. Sainiemi, V. Jokinen, C. Bower, K. Franze, S. Franssila, P. Andrew, O. Ikkala, R. H. A. Ras, and et al., "Reversible switching between superhydrophobic states on a hierarchically structured surface," *Proceedings of the National Academy of Sciences*, vol. 109, p. 10210–10213, Nov 2012.

[45] G. Heydari, E. Thormann, M. Järn, E. Tyrode, and P. M. Claesson, "Hydrophobic surfaces: Topography effects on wetting by supercooled water and freezing delay," *The Journal of Physical Chemistry C*, vol. 117, p. 21752–21762, Nov 2013.

[46] M. He, H. Li, J. Wang, and Y. Song, "Superhydrophobic surface at low surface temperature," *Applied Physics Letters*, vol. 98, no. 9, p. 093118, 2011.

[47] M. J. Kreder, J. Alvarenga, P. Kim, and J. Aizenberg, "Design of anti-icing surfaces: smooth, textured or slippery?," *Nature Reviews Materials*, vol. 1, no. 1, 2016.

[48] A. Alizadeh, M. Yamada, R. Li, W. Shang, S. Otta, S. Zhong, L. Ge, A. Dhinojwala, K. R. Conway, V. Bahadur, and et al., "Dynamics of ice nucleation on water repellent surfaces," *Langmuir*, vol. 28, no. 6, p. 3180–3186, 2012.

[49] Y. Shen, H. Tao, S. Chen, L. Zhu, T. Wang, and J. Tao, "Icephobic/anti-icing potential of superhydrophobic ti6al4v surfaces with hierarchical textures," *RSC Advances*, vol. 5, no. 3, p. 1666–1672, 2015.

[50] L. Yin, Q. Xia, J. Xue, S. Yang, Q. Wang, and Q. Chen, "In situ investigation of ice formation on surfaces with representative wettability," *Applied Surface Science*, vol. 256, no. 22, p. 6764–6769, 2010.

[51] X.-X. Zhang and M. Chen, "Icephobicity of functionalized graphene surfaces," *Journal of Nanomaterials*, vol. 2016, p. 1–8, 2016.

[52] K. K. Varanasi, T. Deng, J. D. Smith, M. Hsu, and N. Bhate, "Frost formation and ice adhesion on superhydrophobic surfaces," *Applied Physics Letters*, vol. 97, p. 234102, Jun 2010.

[53] J. Liu, C. Zhu, K. Liu, Y. Jiang, Y. Song, J. S. Francisco, X. C. Zeng, and J. Wang, "Distinct ice patterns on solid surfaces with various wettabilities," *Proceedings of the National Academy of Sciences*, vol. 114, p. 11285–11290, Sep 2017.

[54] P. R. Wallace, "The band theory of graphite," *Physical Review*, vol. 71, p. 622–634, Jan 1947.

[55] K. S. Novoselov, "Electric field effect in atomically thin carbon films," *Science*, vol. 306, no. 5696, p. 666–669, 2004.

[56] J.-H. Chen, C. Jang, S. Xiao, M. Ishigami, and M. S. Fuhrer, "Intrinsic and extrinsic performance limits of graphene devices on sio2," *Nature Nanotechnology*, vol. 3, no. 4, p. 206–209, 2008.

[57] K. Cao, S. Feng, Y. Han, L. Gao, T. H. Ly, Z. Xu, and Y. Lu, "Elastic straining of free-standing monolayer graphene," *Nature Communications*, vol. 11, no. 1, 2020.

[58] L. A. Falkovsky, "Optical properties of graphene," *Journal of Physics: Conference Series*, vol. 129, p. 012004, Jan 2008.

[59] P. Hofmann, *Surface Physics: An Introduction*. Philip Hofmann, 2013.

[60] A. H. Castro Neto, F. Guinea, N. M. R. Peres, K. S. Novoselov, and A. K. Geim, "The electronic properties of graphene," *Rev. Mod. Phys.*, vol. 81, pp. 109–162, Jan 2009.

[61] X. Miao, S. Tongay, M. K. Petterson, K. Berke, A. G. Rinzler, B. R. Appleton, and A. F. Hebard, "High efficiency graphene solar cells by chemical doping," *Nano Letters*, vol. 12, p. 2745–2750, Oct 2012.

[62] S. Böhm, "Graphene against corrosion," *Nature Nanotechnology*, vol. 9, no. 10, p. 741–742, 2014.

[63] K. S. Novoselov and A. H. C. Neto, "Two-dimensional crystals-based heterostructures: materials with tailored properties," *Physica Scripta*, vol. T146, p. 014006, Jan 2012.

[64] J. Coraux, A. T. Ndiaye, M. Engler, C. Busse, D. Wall, N. Buckanie, F.-J. M. Z. Heringdorf, R. V. Gastel, B. Poelsema, T. Michely, and et al., "Growth of graphene on Ir(111)," *New Journal of Physics*, vol. 11, p. 039801, Mar 2009.

[65] H. Hattab, A. T. N'Diaye, D. Wall, C. Klein, G. Jnawali, J. Coraux, C. Busse, R. V. Gastel, B. Poelsema, T. Michely, and et al., "Interplay of wrinkles, strain, and lattice parameter in graphene on iridium," *Nano Letters*, vol. 12, p. 678–682, Sep 2012.

[66] A. T. N'Diaye, R. van Gastel, A. J. Martínez-Galera, J. Coraux, H. Hattab, D. Wall, F.-J. M. zu Heringdorf, M. H. von Hoegen, J. M. Gómez-Rodríguez, B. Poelsema, C. Busse, and T. Michely, "In situobservation of stress relaxation in epitaxial graphene," *New Journal of Physics*, vol. 11, p. 113056, nov 2009.

[67] S. Bae, H. Kim, Y. Lee, X. Xu, J.-S. Park, Y. Zheng, J. Balakrishnan, T. Lei, H. R. Kim, Y. I. Song, and et al., "Roll-to-roll production of 30-inch graphene films for transparent electrodes," *Nature Nanotechnology*, vol. 5, no. 8, p. 574–578, 2010.

[68] P. R. Kidambi, D. D. Mariappan, N. T. Dee, A. Vyatskikh, S. Zhang, R. Karnik, and A. J. Hart, "A Scalable Route to Nanoporous Large-Area Atomically Thin Graphene Membranes by Roll-to-Roll Chemical Vapor Deposition and Polymer Support Casting," *ACS Applied Materials & Interfaces*, vol. 10, no. 12, p. 10369–10378, 2018.

[69] A. T. Ndiaye, J. Coraux, T. N. Plasa, C. Busse, and T. Michely, "Structure of epitaxial graphene on Ir(111)," *New Journal of Physics*, vol. 10, no. 4, p. 043033, 2008.

[70] P. J. Feibelman, "Pinning of graphene to Ir(111) by flat Ir dots," *Physical Review B*, vol. 77, no. 16, 2008.

[71] R. Balog, B. Jørgensen, L. Nilsson, M. Andersen, E. Rienks, M. Bianchi, M. Fanetti, E. Lægsgaard, A. Baraldi, S. Lizzit, and et al., "Bandgap opening in graphene induced by patterned hydrogen adsorption," *Nature Materials*, vol. 9, no. 4, p. 315–319, 2010.

[72] R. Brako, D. Šokčević, P. Lazić, and N. Atodiresei, "Graphene on the Ir(111) surface: from van der waals to strong bonding," *New Journal of Physics*, vol. 12, p. 113016, Oct 2010.

[73] F. Banhart, J. Kotakoski, and A. V. Krasheninnikov, "Structural defects in graphene," *ACS Nano*, vol. 5, no. 1, p. 26–41, 2010.

[74] P. A. Denis and F. Iribarne, "Comparative study of defect reactivity in graphene," *The Journal of Physical Chemistry C*, vol. 117, p. 19048–19055, Sep 2013.

[75] Q. Yu, L. A. Jauregui, W. Wu, R. Colby, J. Tian, Z. Su, H. Cao, Z. Liu, D. Pandey, D. Wei, and et al., "Control and characterization of individual grains and grain boundaries in graphene grown by chemical vapour deposition," *Nature Materials*, vol. 10, p. 443–449, Aug 2011.

[76] P. Y. Huang, C. S. Ruiz-Vargas, A. M. V. D. Zande, W. S. Whitney, M. P. Levendorf, J. W. Kevek, S. Garg, J. S. Alden, C. J. Hustedt, Y. Zhu, and et al., "Grains and grain boundaries in single-layer graphene atomic patchwork quilts," *Nature*, vol. 469, no. 7330, p. 389–392, 2011.

[77] O. V. Yazyev and S. G. Louie, "Topological defects in graphene: Dislocations and grain boundaries," *Physical Review B*, vol. 81, no. 19, 2010.

[78] A. K. Geim, "Graphene Prehistory," *Physica Scripta*, vol. T146, p. 014003, Jan 2012.

[79] Z. Xu, H. Sun, X. Zhao, and C. Gao, "Ultrastrong fibers assembled from giant graphene oxide sheets," *Advanced Materials*, vol. 25, p. 188–193, Sep 2012.

[80] R. Joshi, S. Alwarappan, M. Yoshimura, V. Sahajwalla, and Y. Nishina, "Graphene oxide: the new membrane material," *Applied Materials Today*, vol. 1, no. 1, p. 1–12, 2015.

[81] D. A. Dikin, S. Stankovich, E. J. Zimney, R. D. Piner, G. H. B. Dommett, G. Evmenenko, S. T. Nguyen, and R. S. Ruoff, "Preparation and characterization of graphene oxide paper," *Nature*, vol. 448, no. 7152, p. 457–460, 2007.

[82] R. K. Upadhyay, S. Naicker, A. Barman, S. S. Roy, T. Thundat, and P. R. Waghmare, "Fabrication of free-standing graphene oxide films using a facile approach toluene swollen paraffin peeling and green reduction of these films into highly conductive reduced graphene oxide films," *Chemical Engineering Journal*, vol. 354, p. 149–161, 2018.

[83] S. Schöche, N. Hong, M. Khorasaninejad, A. Ambrosio, E. Orabona, P. Maddalena, and F. Capasso, "Optical properties of graphene oxide and reduced graphene oxide determined by spectroscopic ellipsometry," *Applied Surface Science*, vol. 421, p. 778–782, 2017.

[84] E. Grånäs, J. Knudsen, U. A. Schröder, T. Gerber, C. Busse, M. A. Arman, K. Schulte, J. N. Andersen, and T. Michely, "Oxygen intercalation under graphene on Ir(111): Energetics, kinetics, and the role of graphene edges," *ACS Nano*, vol. 6, p. 9951–9963, Dec 2012.

[85] R. Larciprete, S. Fabris, T. Sun, P. Lacovig, A. Baraldi, and S. Lizzit, "Dual path mechanism in the thermal reduction of graphene oxide," *Journal of the American Chemical Society*, vol. 133, p. 17315–17321, Feb 2011.

[86] J. Jung, H. Lim, J. Oh, and Y. Kim, "Functionalization of graphene grown on metal substrate with atomic oxygen: Enolate vs epoxide," *Journal of the American Chemical Society*, vol. 136, p. 8528–8531, Oct 2014.

[87] Z. Novotny, M.-T. Nguyen, F. P. Netzer, V.-A. Glezakou, R. Rousseau, and Z. Dohnálek, "Formation of supported graphene oxide: Evidence for enolate species," *Journal of the American Chemical Society*, vol. 140, p. 5102–5109, May 2018.

[88] P. Lacovig, M. Pozzo, D. Alfè, P. Vilmercati, A. Baraldi, and S. Lizzit, "Growth of dome-shaped carbon nanoislands on Ir(111): The intermediate between carbidic clusters and quasi-free-standing graphene," *Physical Review Letters*, vol. 103, Dec 2009.

[89] R. Larciprete, S. Ulstrup, P. Lacovig, M. Dalmiglio, M. Bianchi, F. Mazzola, L. Hornekær, F. Orlando, A. Baraldi, P. Hofmann, and et al., "Oxygen switching of the epitaxial graphene–metal interaction," *ACS Nano*, vol. 6, no. 11, p. 9551–9558, 2012.

[90] L. A. Belyaeva and G. F. Schneider, "Wettability of graphene," *Surface Science Reports*, vol. 75, no. 2, p. 100482, 2020.

[91] J. Rafiee, X. Mi, H. Gullapalli, A. V. Thomas, F. Yavari, Y. Shi, P. M. Ajayan, and N. A. Koratkar, "Wetting transparency of graphene," *Nature Materials*, vol. 11, no. 3, p. 217–222, 2012.

[92] S. Wang, Y. Zhang, N. Abidi, and L. Cabrales, "Wettability and surface free energy of graphene films," *Langmuir*, vol. 25, no. 18, p. 11078–11081, 2009.

[93] G. Scocchi, D. Sergi, C. Dangelo, and A. Ortona, "Wetting and contact-line effects for spherical and cylindrical droplets on graphene layers: A comparative molecular-dynamics investigation," *Physical Review E*, vol. 84, Jan 2011.

[94] F. Du, J. Huang, H. Duan, C. Xiong, and J. Wang, "Wetting transparency of supported graphene is regulated by polarities of liquids and substrates," *Applied Surface Science*, vol. 454, p. 249–255, 2018.

[95] R. Raj, S. C. Maroo, and E. N. Wang, "Wettability of graphene," *Nano Letters*, vol. 13, p. 1509–1515, Jul 2013.

[96] Z. Li, Z. Zhen, M. Chai, X. Zhao, Y. Zhong, and H. Zhu, "Transparent electrothermal film defoggers and antiicing coatings based on wrinkled graphene," *Small*, vol. 16, no. 4, p. 1905945, 2019.

[97] Z. Li, Y. Wang, A. Kozbial, G. Shenoy, F. Zhou, R. Mcginley, P. Ireland, B. Morganstein, A. Kunkel, S. P. Surwade, and et al., "Effect of airborne contaminants on the wettability of supported graphene and graphite," *Nature Materials*, vol. 12, no. 10, p. 925–931, 2013.

[98] A. I. Aria, P. R. Kidambi, R. S. Weatherup, L. Xiao, J. A. Williams, and S. Hofmann, "Time evolution of the wettability of supported graphene under ambient air exposure," *The Journal of Physical Chemistry C*, vol. 120, no. 4, p. 2215–2224, 2016.

[99] G. Yiapanis, A. J. Makarucha, J. S. Baldauf, and M. T. Downton, "Simulations of graphitic nanoparticles at air–water interfaces," *Nanoscale*, vol. 8, no. 47, p. 19620–19628, 2016.

[100] A. V. Prydatko, L. A. Belyaeva, L. Jiang, L. M. C. Lima, and G. F. Schneider, "Contact angle measurement of free-standing square-millimeter single-layer graphene," *Nature Communications*, vol. 9, Oct 2018.

[101] N. Wei, C. Lv, and Z. Xu, "Wetting of graphene oxide: A molecular dynamics study," *Langmuir*, vol. 30, no. 12, pp. 3572–3578, 2014.

[102] P. Sun, M. Zhu, K. Wang, M. Zhong, J. Wei, D. Wu, Z. Xu, and H. Zhu, "Selective ion penetration of graphene oxide membranes," *ACS nano*, vol. 7, no. 1, pp. 428–437, 2013.

[103] X. Zhang, P. Song, and X. Cui, "Photoinduced hydrophobic surface of graphene oxide thin films," *Thin Solid Films*, vol. 520, no. 9, pp. 3539–3543, 2012.

[104] C.-T. Hsieh and W.-Y. Chen, "Water/oil repellency and work of adhesion of liquid droplets on graphene oxide and graphene surfaces," *Surface and Coatings Technology*, vol. 205, no. 19, pp. 4554–4561, 2011.

[105] R. Rasuli, Z. Mokarian, R. Karimi, H. Shabanzadeh, and Y. Abedini, "Wettability modification of graphene oxide by removal of carboxyl functional groups using non-thermal effects of microwave," *Thin Solid Films*, vol. 589, p. 364–368, 2015.

[106] M. Zokaie and M. Foroutan, "Confinement effects of graphene oxide nanosheets on liquid–solid phase transition of water," *RSC Advances*, vol. 5, no. 118, p. 97446–97457, 2015.

[107] G. Bai, D. Gao, Z. Liu, X. Zhou, and J. Wang, "Probing the critical nucleus size for ice formation with graphene oxide nanosheets," *Nature*, vol. 576, no. 7787, pp. 437–441, 2019.

[108] H. Geng, X. Liu, G. Shi, G. Bai, J. Ma, J. Chen, Z. Wu, Y. Song, H. Fang, and J. Wang, "Graphene oxide restricts growth and recrystallization of ice crystals," *Angewandte Chemie International Edition*, vol. 56, no. 4, pp. 997–1001, 2017.

[109] L. J. Whitman, "Tunneling microscopy and spectroscopy," *digital Encyclopedia of Applied Physics*, 2003.

[110] E. Laegsgaard, F. Besenbacher, K. Mortensen, and I. Stensgaard, "A fully automated, 'thimble-size' scanning tunnelling microscope," *Journal of Microscopy*, vol. 152, no. 3, p. 663–669, 1988.

[111] M. Sardela, *Practical materials characterization*. Springer, 2016.

[112] O. I. Klyushnikov, "Method to determine the work function using x-ray photoelectron spectroscopy," *Journal of Structural Chemistry*, vol. 39, no. 6, p. 944–947, 1998.

[113] J. F. Moulder, W. F. Stickle, P. E. Sobol, and K. D. Bomben, *Handbook of X-ray photoelectron spectroscopy: a reference book of standard spectra for identification and interpretation of XPS data*. Physical Electronics, 1995.

[114] A. Zangwill, *Physics at surfaces*. Cambridge University Press, 1988.

[115] S. Doniach and M. Sunjic, "Many-electron singularity in x-ray photoemission and x-ray line spectra from metals," *Journal of Physics C: Solid State Physics*, vol. 3, p. 285–291, Jan 1970.

[116] https://phys.au.dk/en/research/research-areas/condensed-matter-physics/surface-dynamics-group/the lab/, "The surface dynamics laboratory," *Accessed: June 15 2020*.

[117] I. Horcas, R. Fernández, J. M. Gómez-Rodríguez, J. Colchero, J. Gómez-Herrero, and A. M. Baro, "Wsxm: A software for scanning probe microscopy and a tool for nanotechnology," *Review of Scientific Instruments*, vol. 78, no. 1, p. 013705, 2007.

[118] https://www.kolibrik.net/en/kolxpd, "Kolxpd: Spectroscopy data measurement and processing," *Accessed: June 10 2020*.

[119] https://www.dataphysics instruments.com/products/oca/, "Oca – optical contact angle measuring and contour analysis systems," *Accessed: June 12 2020*.

[120] D. S. Shin, H. G. Kim, H. S. Ahn, H. Y. Jeong, Y.-J. Kim, D. Odkhuu, N. Tsogbadrakh, B. H. Kim, *et al.*, "Distribution of oxygen functional groups of graphene oxide obtained from low-temperature atomic layer deposition of titanium oxide," *RSC advances*, vol. 7, no. 23, pp. 13979–13984, 2017.

[121] R. Al-Gaashani, A. Najjar, Y. Zakaria, S. Mansour, and M. Atieh, "Xps and structural studies of high quality graphene oxide and reduced graphene oxide prepared by different chemical oxidation methods," *Ceramics International*, vol. 45, p. 14439–14448, 2019.

[122] Y. C. G. Kwan, G. M. Ng, and C. H. A. Huan, "Identification of functional groups and determination of carboxyl formation temperature in graphene oxide using the xps o 1s spectrum," *Thin Solid Films*, vol. 590, p. 40–48, 2015.

[123] L. Kyhl, R. Bisson, R. Balog, M. N. Groves, E. L. Kolsbjerg, A. M. Cassidy, J. H. Jørgensen, S. Halkjær, J. A. Miwa, A. G. Čabo, and et al., "Exciting h2 molecules for graphene functionalization," *ACS Nano*, vol. 12, no. 1, p. 513–520, 2017.

[124] N. Giovambattista, P. G. Debenedetti, and P. J. Rossky, "Effect of surface polarity on water contact angle and interfacial hydration structure," *The Journal of Physical Chemistry B*, vol. 111, no. 32, pp. 9581–9587, 2007.

[125] J. D. Miller, S. Veeramasuneni, J. Drelich, M. R. Yalamanchili, and G. Yamauchi, "Effect of roughness as determined by atomic force microscopy on the wetting properties of ptfe thin films," *Polymer Engineering & Science*, vol. 36, no. 14, p. 1849–1855, 1996.

[126] K. Göbbels, T. Kuenzel, A. V. Ooyen, W. Baumgartner, U. Schnakenberg, and P. Bräunig, "Neuronal cell growth on iridium oxide," *Biomaterials*, vol. 31, no. 6, p. 1055–1067, 2010.

[127] K. Xu, J. Zhang, X. Hao, C. Zhang, N. Wei, and C. Zhang, "Wetting properties of defective graphene oxide: A molecular simulation study," *Molecules*, vol. 23, no. 6, p. 1439, 2018.

[128] X. Feng, S. Maier, and M. Salmeron, "Water splits epitaxial graphene and intercalates," *Journal of the American Chemical Society*, vol. 134, no. 12, p. 5662–5668, 2012.

[129] Z. Li, S. Li, H.-Y. T. Chen, N. Gao, K. Schouteden, X. Qiang, J. Zhao, S. Brems, C. Huyghebaert, C. V. Haesendonck, and et al., "Strongly hole-doped and highly decoupled graphene on platinum by water intercalation," *The Journal of Physical Chemistry Letters*, vol. 10, no. 14, p. 3998–4002, 2019.

[130] K. T. He, J. D. Wood, G. P. Doidge, E. Pop, and J. W. Lyding, "Scanning tunneling microscopy study and nanomanipulation of graphene-coated water on mica," *Nano Letters*, vol. 12, no. 6, p. 2665–2672, 2012.

[131] G. He, Q. Wang, H. K. Yu, D. Farías, Y. Liu, and A. Politano, "Water-induced hydrogenation of graphene/metal interfaces at room temperature: Insights on water intercalation and identification of sites for water splitting," *Nano Research*, vol. 12, no. 12, p. 3101–3108, 2019.

Appendix A

A.1 Supplementary STM Analysis

A.1.1 STM FFT images

Figure 1 shows full FFT images of the low-coverage sample before (a)) and after (b)) oxygen dose, respectively. Corresponding STM images can be found in the section 6.1.1 and 6.1.2 in the main text.

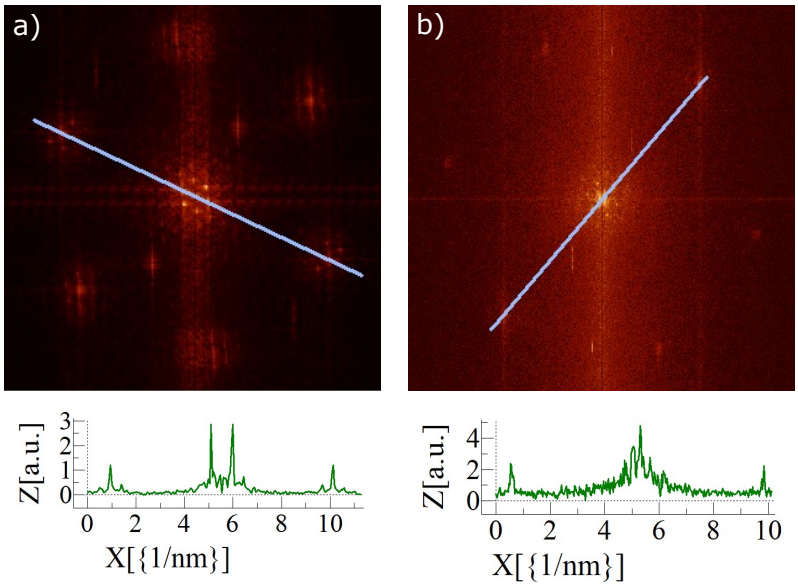

Figure 1: The full FFT images of the low-coverage sample a) before and after b) oxygen dose.

Figure 2a) and b) shows the FFT image of the high-coverage sample before and after oxygen dose, respectively. Corresponding STM images can be found in section 6.2.1 and 6.2.2 in the main text.

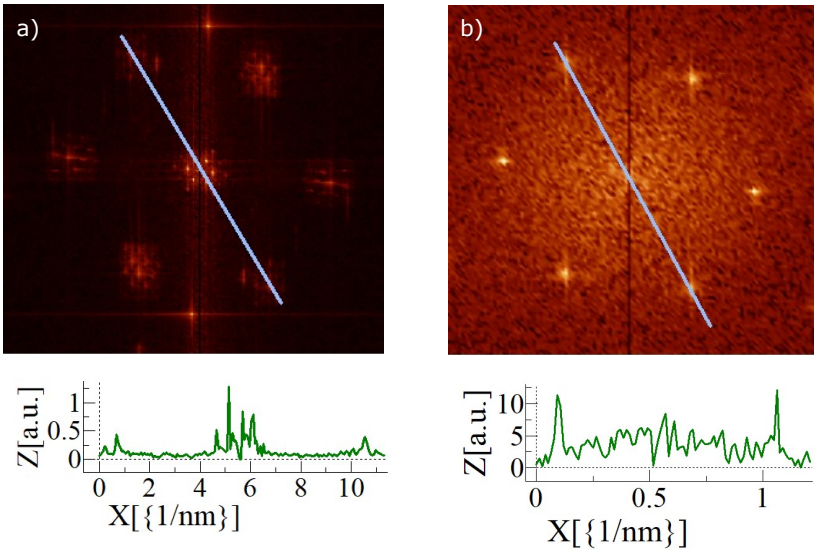

Figure 2: The full FFT images of the high-coverage sample a) before and after b) oxygen dose.

Figure 3a) and b) shows the FFT image of a functionalized area and an intercalated area after wetting and icing experiments, respectively. Corresponding STM images can be found in section 6.5.1 in the main text.

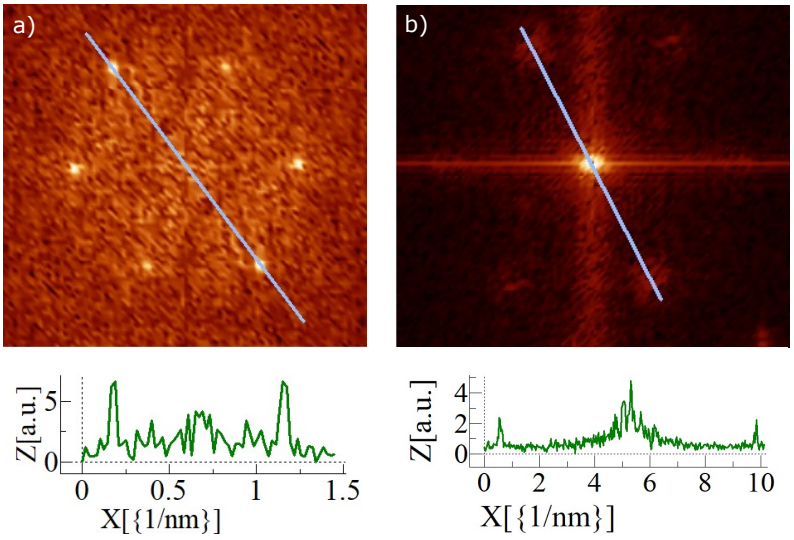

Figure 3: The full FFT images of the high-coverage sample at a) a functionalized area and at b) an intercalated area.

A.1.2 STM Coverage Analysis (Low-Coverage Sample)

Figure 4 shows the STM images that were used to quantify the coverage for the low coverage sample, as discussed in section 6.1.2 in the main text.

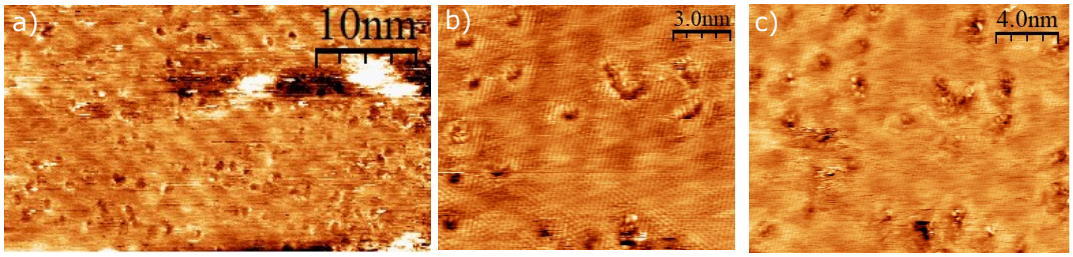

Figure 4: Three images used for coverage analysis. a) Scanning parameters: It: 1490 pA, Vt: 5.5 mV. b) Scanning parameters: It: 960 pA, Vt: 11.0 mV. c) Scanning parameters: 940 pA, Vt: 11.0 mV.

A.1.3 STM High-Coverage Large Area Images

Figure 5 shows the STM images of large areas of graphene. These images were used to draw the conclusion that only small patch(es) on the sample consisted of bare Ir(111) after graphene growth (discussed in section 6.2.1 in the main text). Figure 5b) is a zoom of the black area in a).

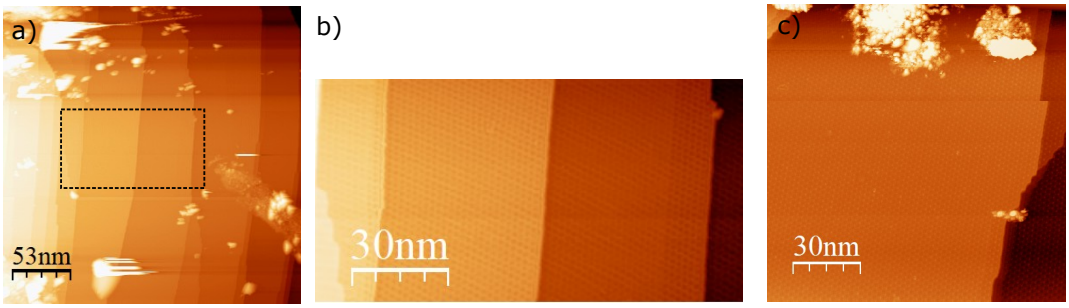

Figure 5: Large-scale STM images of the high-coverage sample. a) Scanning parameters: 1480 pA, 106.8 mV. b) Area marked with black rectangle in (a). c) Scanning parameters: It: 810 pA, Vt: 106.8 mV.

A.1.4 Corrugation Analysis

Figure 6, 7, 8, and 9 represent the STM images used for corrugation calculation for the O-Gr/Ir(111) low-coverage sample, O-Gr/Ir(111) high-coverage sample, Gr/Ir(111) step-edges, and Gr/Ir(111) wrinkles, respectively. The left panel shows the STM images and the right panel show the histogram used for roughness analysis.

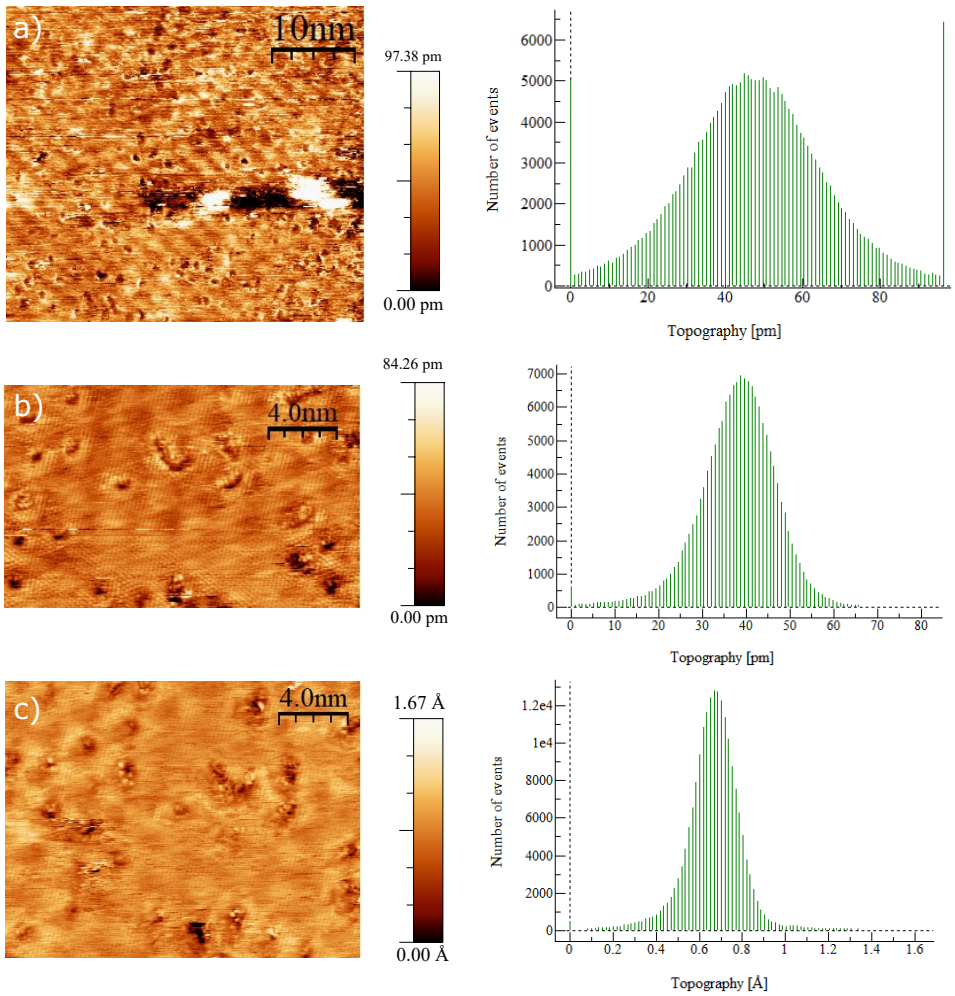

Figure 6: Left: STM images of the low-coverage O-Gr/Ir(111) sample, used for corrugation analysis for the low-coverage sample. Right: Toporaphy histogram of the corresponding image. a) Scanning parameters: It: 1490 pA, Vt: 5.5 mV. b) Scanning parameters: It: 960 pA, Vt: 11.0 mV. c) Scanning parameters: 940 pA, Vt: 11.0 mV.

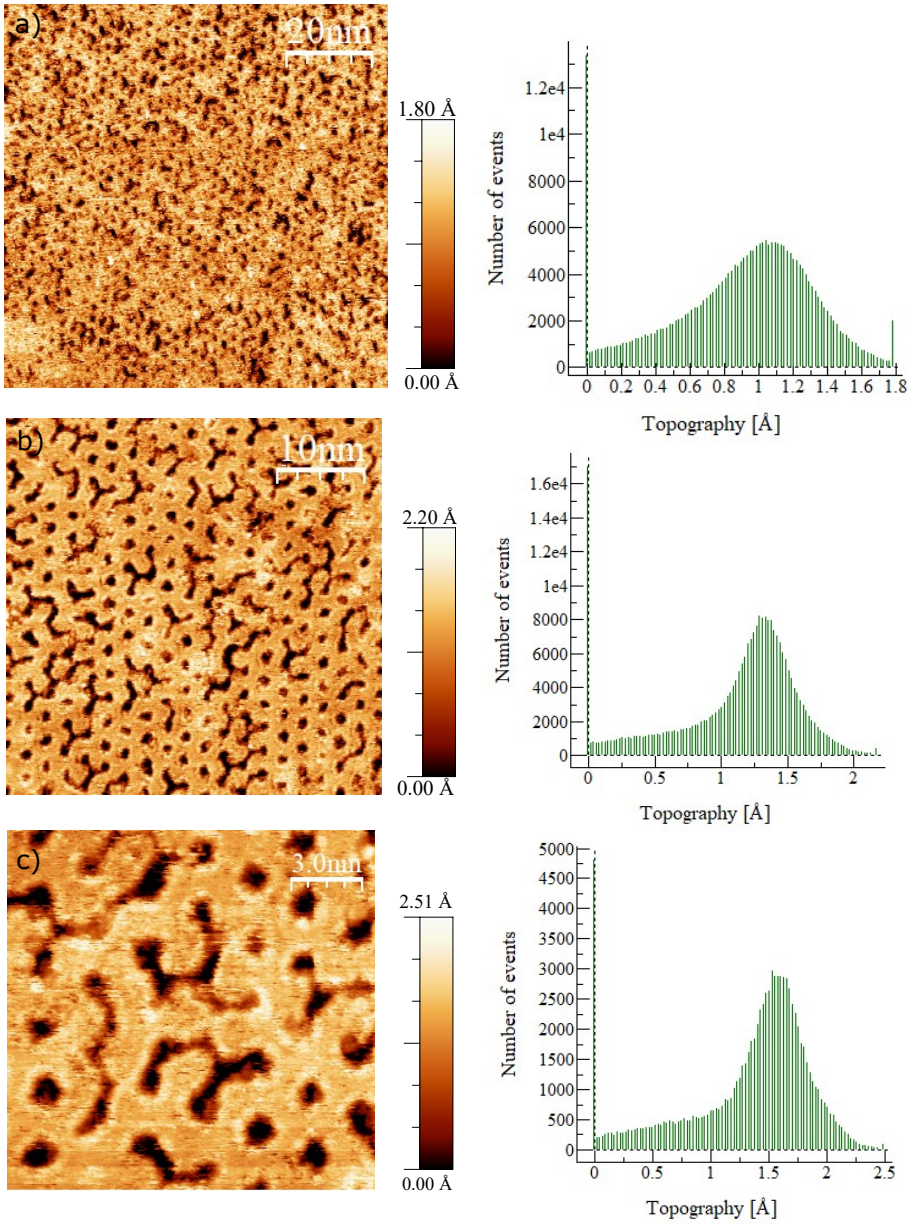

Figure 7: Left: STM images of the high-coverage O-Gr/Ir(111) sample, used for corrugation analysis for the high-coverage sample. Right: Toporaphy histogram of the corresponding image. a) Scanning parameters: It: 420 pA, Vt: 396.4 mV. b) Scanning parameters: It: 150 pA, Vt: 475.8 mV. c) Scanning parameters: It: 150 pA, Vt: 475.8 mV.

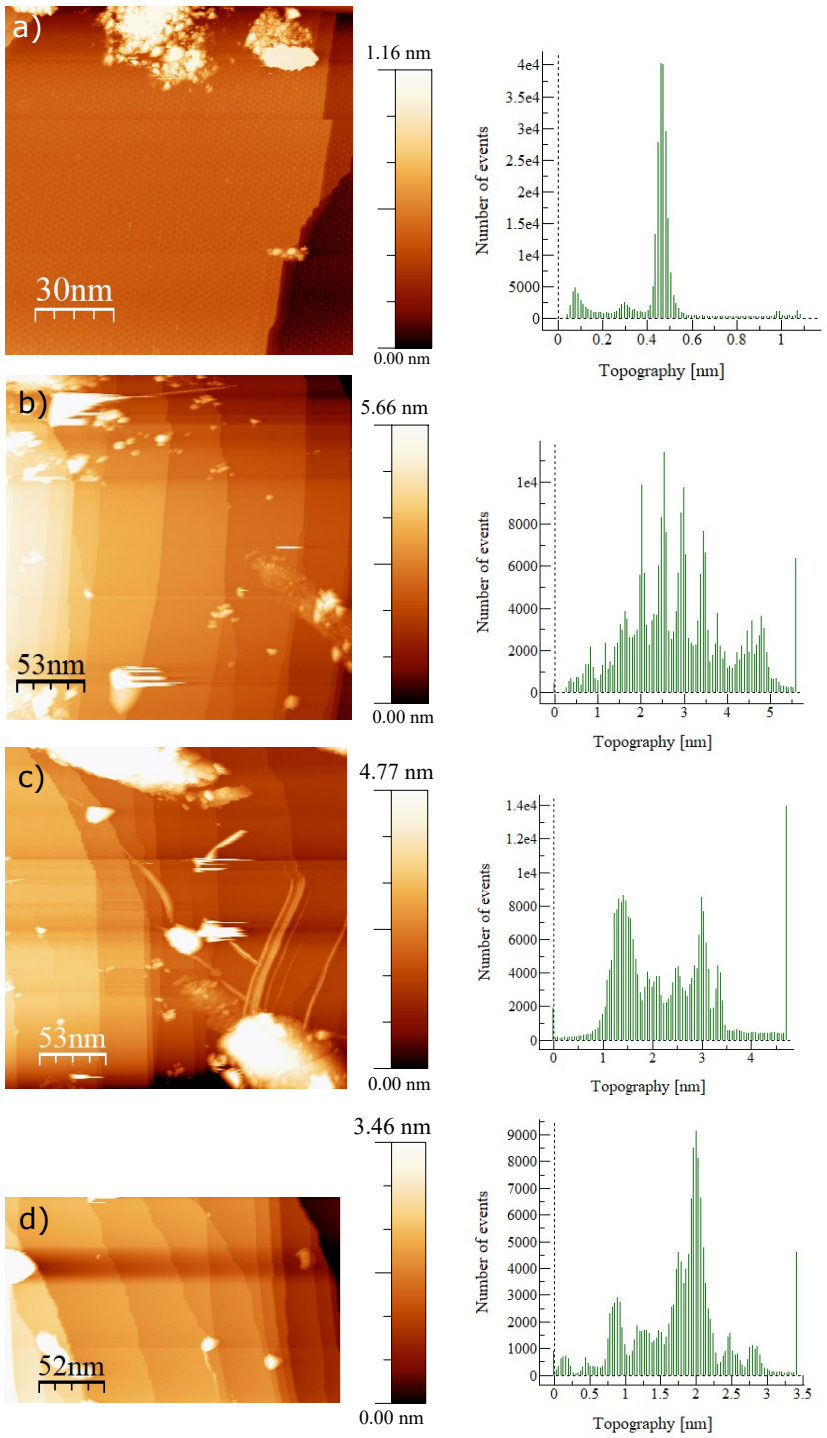

Figure 8: Left: STM images of the Gr/Ir(111) high-coverage sample, used for corrugation analysis for wrinkles on graphene. Right: Toporaphy histogram of the corresponding image. a) Scanning parameters: It: 810 pA, Vt: 106.8 mV. b) Scanning parameters: It: 760 pA, Vt: 106.8 mV. c) Scanning parameters: It: 790 nA, Vt: 106.8 mV. d) Scanning parameters: 1480 pA, 106.8 mV.

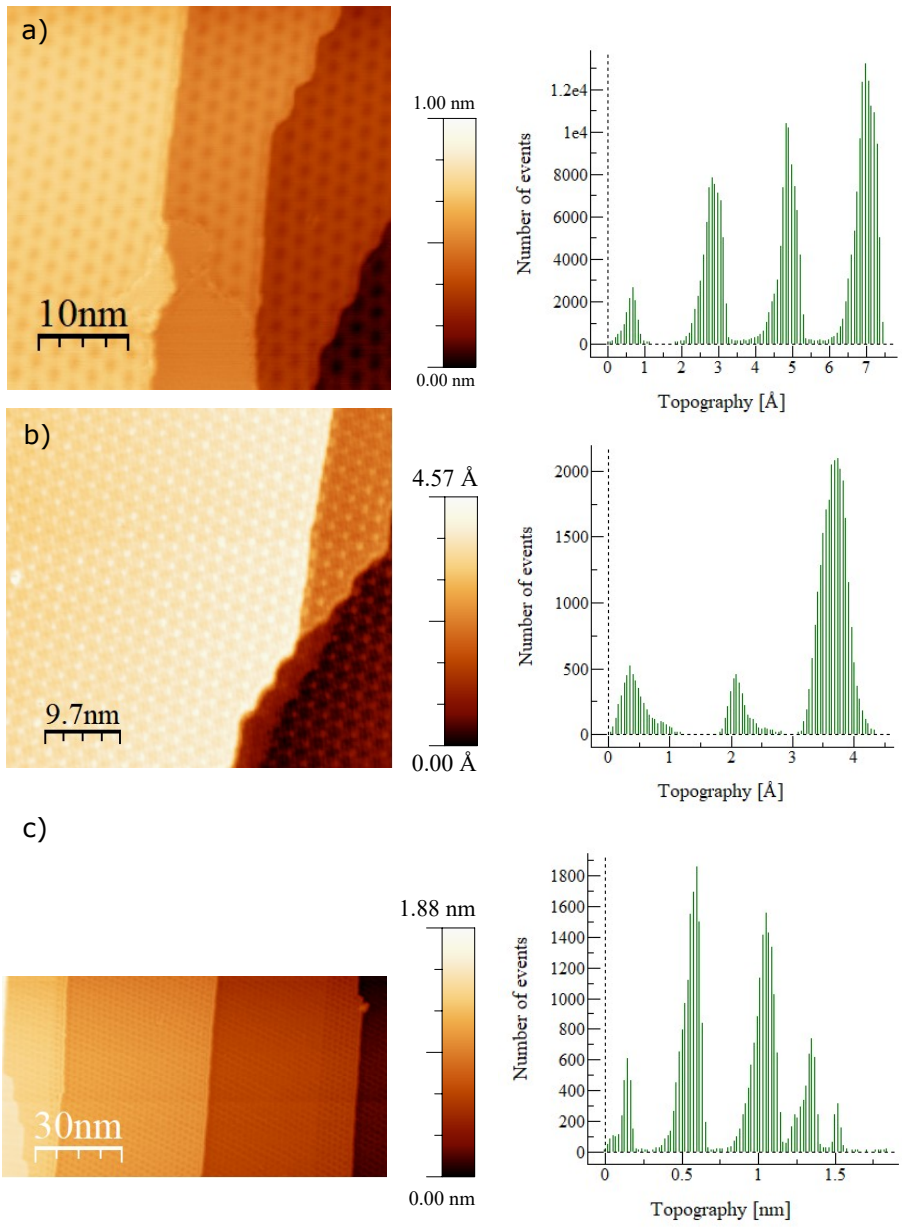

Figure 9: Left: STM images of the Gr/Ir(111) high-coverage sample, used for corrugation analysis for stepedges on graphene. Right: Toporaphy histogram of the corresponding image. a) Scanning parameters: 0.350 nA, Vt: 57.1 mV. b) Scanning parameters: It: 810 pA, Vt: 106.8 mV. c) Scanning parameters: 1480 pA, 106.8 mV.

Appendix B

B.2 Scientific Article

The article written on the basis of the result is presented in the following. The article will be submitted to Carbon.

Wetting and icing properties of oxidized graphene on Ir(111): A study of enolate functionalization

Signe Kyrkjebø,[1,2] Andrew Cassidy,[2] Naureen Akhtar,[1,3] Richard Balog,[2] Martha Scheffler,[2] Liv Hornekær,[2] Bodil Holst,[1,a)] and Ranveig Flatabø[1,b)]

[1)] *University of Bergen, Department of Physics and Technology, Bergen, Norway*

[2)] *Aarhus University, Department of Physics and Astronomy, Aarhus, Denmark*

[3)] *New address Naureeen*

Graphene oxide is one of the most common graphene derivatives with a wide range of applications. In chemically synthesized graphene oxide hydroxyl- and epoxy- groups are the dominating functional groups on the basal plane of graphene. Chemically synthesized graphene oxide is hydrophilic and has been shown to have good icephobic properties, both freestanding and when placed on a surface. In 2018 a new type of oxidized graphene was discovered on Ir(111), where the dominating functional group on the basal plane is enolates. Here we present the first study of surface properties of oxidized graphene on Ir(111) (O-Gr/Ir(111)) under ambient conditions. We find that the surface is almost hydrophobic with a water contact angle of $80° \pm 4°$. This is similar to that of bare Ir(111) thus indicating that oxidized graphene on Ir(111) is transparent to wetting. The freezing onset temperature is found to be $21°C \pm 1°C$. Scanning tunneling microscopy and x-ray photon spectroscopy obtained after the wetting and icing experiments show intercalation of oxygen and/or water. However, the intercalation mainly takes place on the edges where the graphene layer is less perfect. The intercalation appears to be accompanied by the loss of oxygen-containing functional groups.

[a)] Electronic mail: Bodil.Holst@uib.no

[b)] Electronic mail: Ranveig.Flatabo@uib.no

I. INTRODUCTION

Oxygen-functionalized graphene is one of the most common graphene derivatives. Graphene oxide was synthesized for the first time by exposing graphite to strong acids by B. Brody in 1859[1]. Currently, graphene oxide is usually made by the Hummers method, see e.g. ref.[2]. It has been successfully made into fibers[3], membranes[4], papers[5] and freestanding multilayered films[6], and it can be e.g. drop-casted onto various substrates[7]. The actual and potential applications of graphene oxide include energy storage[8], water treatment[9], sensors[10] and protective coatings[11]. The basal plane of chemically synthesized graphene oxide is mainly decorated with hydroxyl- and epoxy groups, see Fig. 1. The edges likely contain carboxyl-, carbonyl-, phenol groups, etc.,[12]. As-synthesized graphene oxide is non-stoichiometric (O:C ratio usually in the range 0.3 to 0.5)[13]. The oxygen-containing groups are distributed in the form of islands that are interspersed with regions of graphene[14]. Theory (DFT) predicts that graphene sheets functionalized with epoxy- and hydroxyl groups are stable (i.e. do not decompose into O_2, H_2O and graphene) at temperatures ≤ 70°C due to this island-like structure[13].

Chemically synthesized graphene oxide is hydrophilic (i.e. readily dispersible in water) with a reported water contact angle (WCA) in the range $\sim 25°$ - $55°$[15–18]. Carboxyl- and hydroxyl groups are considered the main hydrophilic functional groups. By removing the carboxyl groups from graphene oxide using non-thermal microwaves Rasuli et al.[19], increased the WCA from $\sim 30°$ to $\sim 70°$. Zhang et al.,[17] found that UV irradiation of graphene oxide thin films induced an increase in the WCA from 27.3° to 57.6°. They attributed this change to the removal of hydroxyl- and carbonyl groups.

The relatively large spread in observed WCA ($\sim 25°$ - $55°$) is typical for graphene-based materials; their wettability is highly debated. Pristine graphene has been suggested to be hydrophilic and hydrophobic; transparent, translucent, and opaque to wetting[20–23]. In 2018 Prydatko et al.,[22] showed that free-standing, clean graphene is hydrophilic with a WCA of $42° \pm 3°$. In general, the observed WCA depends upon the graphene (e.g. quality, storage, cleanliness, functionalization), the measurement conditions, and when supported by a substrate, the properties of the underlying substrate (e.g. cleanliness, roughness, chemical

composition, preparation)[20,22].

Despite its hydrophilic nature, graphene oxide, with epoxy- and hydroxyl groups, has been predicted to have superior icephobic properties (i.e. ability to repel ice)[24–27]. Zokaie et al.,[25] calculated the freezing onset temperature for confined water between two graphene oxide sheets to be as low as -37°C. The functional groups were found to force the water molecules near the sheets to remain in a liquid state due to confinement effects. The mean ice nucleation temperature of water containing graphene oxide sheets (average sheet size 8 nm or smaller) was experimentally demonstrated to be -27.6°C by Bai et al.,[27]. For graphene oxide sheets (8 nm in size) anchored to a silicon wafer, the ice nucleation temperature was found to be down to - 24.6°C depending upon the contact area between the water droplets and the surface[27]. Geng et al.,[26] demonstrated that a graphene oxide dispersion can suppress the growth of ice crystals, and concluded that graphene oxide behaves as an antifreeze protein. Specifically, they found that the hydroxyl group on the graphene basal plane binds more efficiently to ice crystals than to liquid water which gives rise to a curved ice crystal surface that inhibits the growth of ice.

The non-stoichiometric nature of chemically synthesized graphene oxide makes it challenging to control its properties[13]. One way to achieve uniform functionalization or to selectively functionalize one site over another is to expose chemical vapor deposited (CVD) grown graphene to atomic oxygen. Note that we distinguish between *graphene oxide* and *oxidized graphene*: graphene oxide is prepared in solution whereas oxidized graphene is CVD grown and supported by a substrate. CVD can yield high-quality single-layer graphene with a low concentration of defects. It was widely assumed that epoxy is the main functional group on the basal plane of oxidized graphene[28,29]. However, a new functional group, enolate, was recently discovered on graphene islands on Ru(0001)[30] and later on Ir(111)[31]. An enolate is a bond formation in which one carbon atom binds to an oxygen atom while a neighboring carbon atom binds to the underlying substrate, see Fig. 1. The stability of enolate-functionalized graphene upon exposure to air and water is not known, and to the best of our knowledge, the wetting- and icing properties of enolate-functionalized graphene have not been studied before this work.

Here, we present a study of oxygen-functionalize CVD-grown graphene on Ir(111). We measure the WCA of the oxidized graphene (enolate functionalized) on Ir(111) (O-Gr/Ir(111)) surface and the freezing onset temperature. Furthermore, we characterize the

O-Gr/Ir(111) on the atomic level using scanning tunneling microscopy (STM) and x-ray photoelectron spectroscopy (XPS) before and after exposure to air and water droplets.

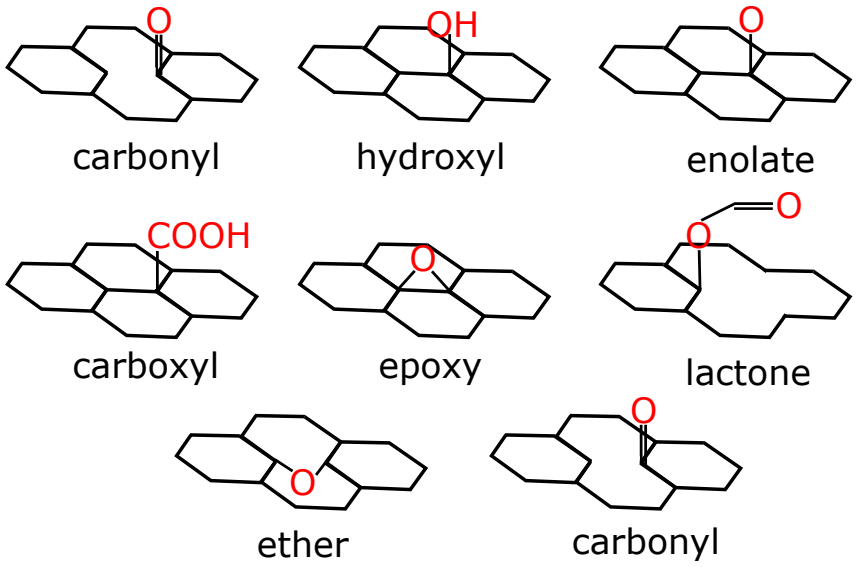

Figure 1: Various functional groups in oxygen-functionalized graphene.

II. EXPERIMENTAL

A. Graphene growth and oxygen functionalization

An (111) iridium crystal 7 mm in diameter and ?? mm thick with a miscut of ??? was mounted in a crystal sample holder made of tantalum. A K-type thermocouple was attached to the backside of the crystal to measure temperature. The sample remained mounted in the crystal sample holder throughout all experiments, see Fig. 2.

The sample was placed in a chamber with a base pressure of 10^{-10} mbar. The graphene was grown by dosing ethylene on the clean Ir(111) crystal at 3×10^{-7} mbar for 18 minutes at room temperature. The base pressure was around 10^{-10} mbar. Subsequently, the sample was flashed (in vacuum) to 1250°C. The sample temperature was then decreased to 900°C and the ethylene pressure was adjusted to 3×10^{-7} mbar for 15 minutes. The resulting Gr/Ir(111) sample was cooled to room temperature at a rate of 0.2°C/s using a temperature controller. Next, the sample was transferred to a different chamber using a vacuum suitcase with a base pressure of 10^{-5} mbar. The Gr/Ir(111) sample was annealed to 120 °C, cooled

to room temperature, and then exposed to a flux of oxygen atoms produced by cracking O_2 atoms in a heated Ir capillary (1560°C) for 4 minutes. The sample was placed 10 cm from the doser at normal incidence to maximize the cross-section, and the flux reaching the sample (7 mm i diameter) was estimated to be 1.5×10^{-11} atoms/s. The pressure in the main chamber during exposure to atomic oxygen was fixed at 1.8×10^{-7}mbar.

B. Surface characterization

The STM images were taken using an Aarhus type STM[32]. Images were recorded at room temperature and analyzed using the WsXM software[33].

XPS spectra before and after the wetting and icing experiments were recorded using a laboratory XPS (XR50 X-ray source and Phobios 150 energy analyzer from Specs, Germany) which generates photons with an energy of 1250 eV. According to the manual the spot size was 1-2 cm^2 (elliptical-shaped). Additionally, XPS spectra after the wetting and icing experiments were obtained using synchrotron radiation generated by ASTRID2 in the MatLine beamline. The photons generated were tuned to have energies of 340 eV and 650 eV to collect data for C1s and O1s, respectively. All XPS data were fitted using the KolXPD software[34].

C. Wetting and icing experiments

The sample was transported from Aarhus to Bergen. Care was taken to do this in the least invasive way. The crystal sample holder was placed upside down in a copper block, where it could sit firmly. The copper block was then wrapped in aluminium foil and placed in a plastic container. To the naked eye, the transport did not seem to damage the sample.

WCA and freezing onset temperature were measured using a DataPhysics OCA 20 instrument (DataPhysics GmbH, Germany). The measurements were done in ambient air at room temperature 22°C ± 2°C, and relative humidity of 30 % ± 2%. The copper block that housed the crystal sample holder was designed to ensure good thermal contact between the Peltier plate and the O-Gr/Ir(111) sample, see Fig. 2. A K-type thermocouple was used to measure the temperature of the O-Gr/Ir(111) surface. The WCA was measured using a 2 μL water droplet (DI water) at room temperature. Four cycles of WCA measurements,

each consisting of eight measurements, were conducted over five days. After each WCA measurement, the Peltier plate was cooled at a rate of 0.16 K/sec until the droplet froze to determine the WCA as a function of temperature and the freezing onset temperature.

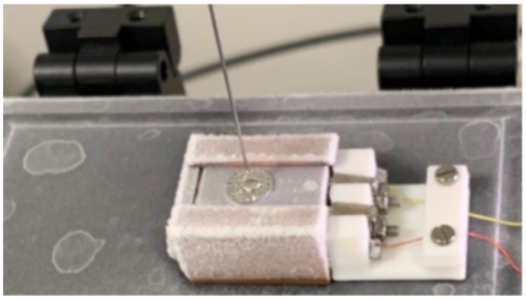

Figure 2: Image of the O-Gr/Ir(111) sample and sample holder used in the wetting and icing experiments. The needle dispers microlitre water droplets. The wires seen to the right are thermocouple wires which monitor the sample temperature.

III. RESULTS AND DISCUSSION

A. Surface analysis before the wetting and icing experiments

The slight mismatch between graphene lattice constant and Ir(111) surface atoms results in a moiré structure visible after graphene growth (see Fig. S1 in Suppl. Material). It consists of so-called ATOP sites where an Ir atom sits directly underneath the center of the carbon hexagonal; and HCP and FCC regions, where every second C atom is positioned directly above an Ir-atom. HCP and FCC regions differ in the arrangement of Ir atoms in the second and third Ir-layer. The remaining carbon atoms in between TOP and HCP/FCC regions show varying degrees of overlap with the underlying surface Ir atoms. This repeating moiré structure, with a 2.52 nm lattice constant, dominates in STM imaging of the Gr/Ir(111) basal plane[35].

STM images of oxidized graphene on Ir(111) are presented in Fig. 3. The fast fourier transform (FFT) of the area in Fig. 3(a) is shown as an inset. The hexagonal lattice constant is found to be 2.5 nm $\pm$ 0.05 nm, so the moiré structure is intact after oxygen dosing. The main functional group in O-Gr/Ir(111) is enolate. Enolates can only bind to FCC/HCP

regions of the moiré structure[31]. Therefore, the dark circular holes are assumed to be unreacted ATOP sites (i.e. bare graphene) and the remainder of the surface is FCC/HCP regions covered with oxygen species, see schematic in Fig. 3(b). The dark elongated structure, shown with a blue arrow in figure 3(b), shows unreacted intermediate areas (i.e. bare graphene).

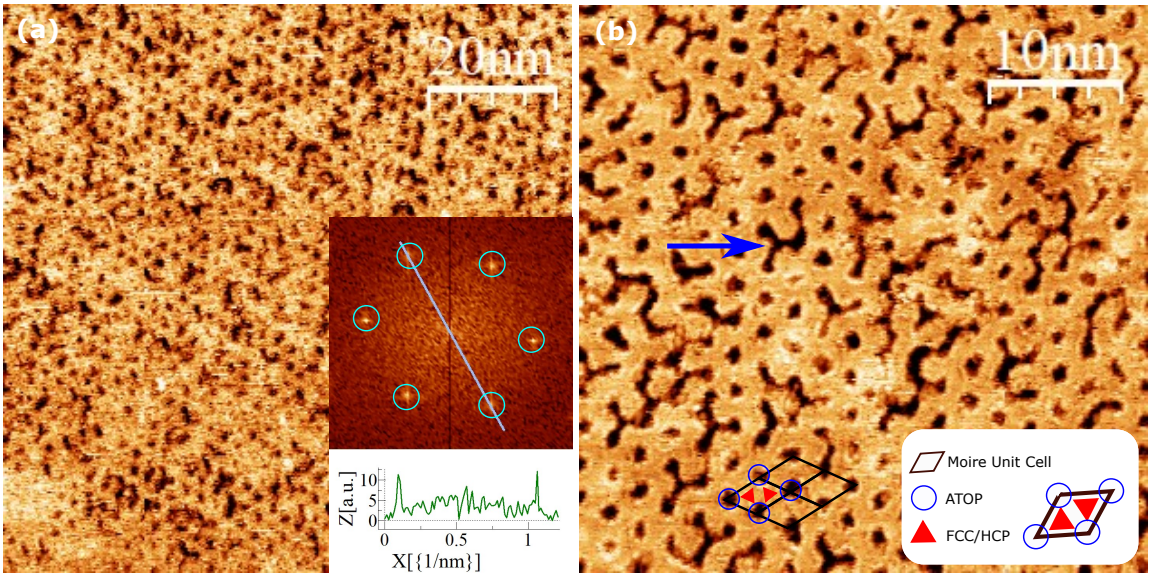

Figure 3: STM images of O-Gr/Ir(111) before wetting and icing experiments. (a) Image with corresponding FFT spectrum. The hexagonal pattern arising from the graphene-Ir(111) moiré structure is visible. The hexagonal lattice contstant is found to be 2.5 ± 0.05 nm, unchanged after oxygen dosing. Scanning parameters: It: 420.0 pA, Vt: 396.4 mV. (b) The dark elongated structures, highligted with a blue arrow, are assumed to be bare graphene, the remainder of the surface is assumed to be covered with oxygen. The moiré unit cell is shown with a black rhombus. Blue circles highlight uncreacted ATOP sites and red triangles show oxidized FCC/HCP sites. Scanning parameters: It: 150.0 pA, Vt: 475.8 mV.

XPS spectra (O1s and C1s) obtained before and after exposure to atomic oxygen are given in Fig. 4. Associated peaks and fitting details can be found in Table S1 and S2 respectively in Suppl. Material. The lower panel of Fig. 4 is recorded before oxidation. Oxygen- and sp^3 components are present on the Gr/Ir(111) surface, likely induced by impurities

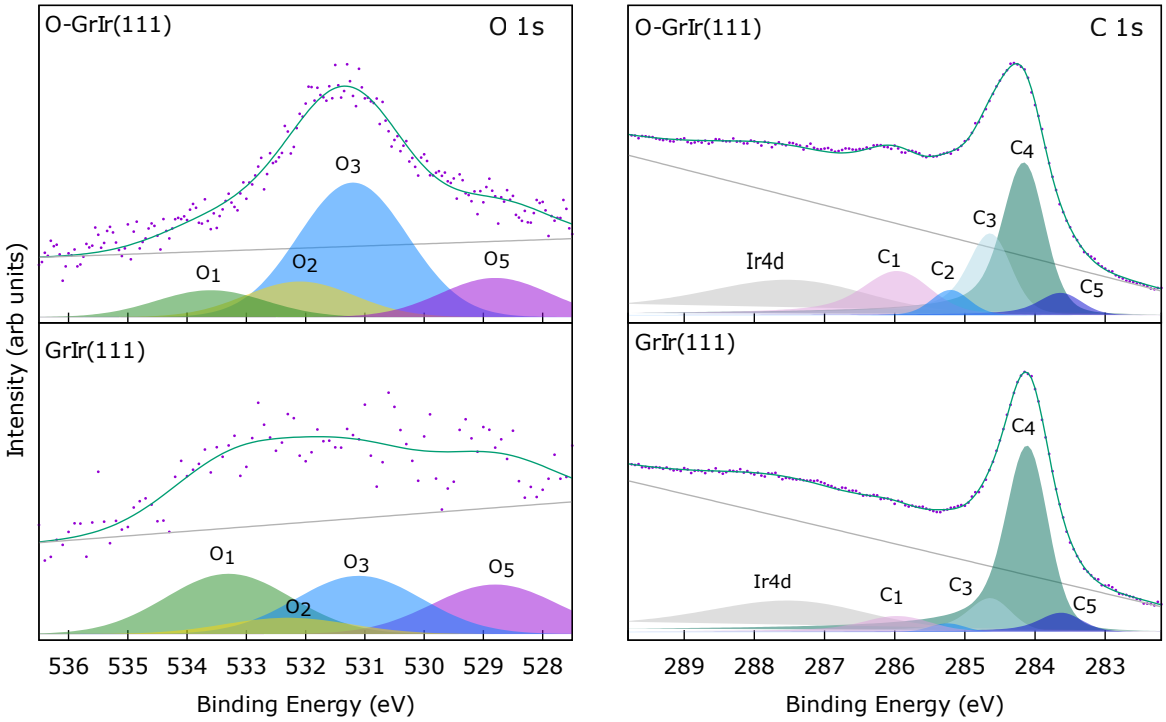

Figure 4: XPS spectra of (a) O1s and (b) C1s peaks. The purple dots are the raw data, the green curve is the fit and the gray line is the background. Lower panel shows pristine graphene on Ir(111), and upper panel is obtained after exposure to atomic oxygen. Peak details can be found in Suppl. Material.

in growth gas. In the O1s spectrum before oxidation, four components were fitted using Gaussian peaks, O_1 (533.4 eV), O_2 (532.2 eV), O_3 (531.2 eV) , and O_5 (528.8 eV). They are attributed to hydroxyl (O_1), ether (O_2), enolate (O_3) and epoxy- and carbonyl groups (O_5), respectively[14,31,36]. After oxygen exposure, the enolate peak (O_3) is the dominant component, in good agreement with literature[31].

Peaks in the C1s spectra are fitted using a Doniach-Šunjić function convoluted with a Gaussian. The sp^2 carbon component is dominant before oxidation, positioned at 284.1 eV (C_4). Furthermore, sp^3 components are observed, namely C_1 (285.9 eV), C_2 (285.3 eV), and C_3 (284.6 eV), attributed to carbonyl groups or a small amount of epoxy, ethers and enolate groups, respectively[31,36]. The Ir4d peak is a diffraction peak. Finally, the component C_5

(283.7 eV) can be attributed to graphene decoupled from iridium[37]. After oxidation, an increase in the sp^3 components are observed, however, C_4 is still the dominant component. It should be noted that the enolate peak (C_3) is expected to shift 0.2-0.5 eV to higher binding energy with the respect to the sp^2-peak (C_4)[31,36], but the XPS used cannot resolve two different peaks in this range. Thus, parts of the enolate peak might be unresolved, embedded in the sp^2-peak.

B. Wetting and icing experiments

Images of a sessile water droplet (2 μL) at various substrate temperatures is presented in Fig. 5. As evident from Fig. 5 the O-Gr/Ir(111) surface is almost hydrophobic at room temperature. The WCA is found to be 80° ± 4° (cycle 1) and the average of cycle 1 - cycle 4 77° ± 6°, see Fig. 6(a). This is significantly larger than what is reported on graphene oxide, except from when the carboxyl groups have been removed[19]. The O-Gr/Ir(111) surface is smooth (surface roughness roughly 1 nm including wrinkles), so the wetting properties are mainly dictated by chemical properties of the O-Gr/Ir(111) surface[38]. As mentioned above, the wettability of graphene-based materials is highly debated[39–41] Shih et al.,[39] calculated that (pristine) graphene is transparent to wetting (i.e. the wetting properties is determined by the underlying substrate) unless it rests on a superhydrophilic or superhydrophobic substrate. Göbbels et al.[42] found that the WCA of iridium increases with oxygen content starting at $\sim 82°$ for bare iridium with a roughness of 1.2 nm. It is therefore likely that oxidized graphene on Ir(111) is transparent (or partly transparent) to wetting. This is supported by a seperate experiment where the WCA of another oxidzied graphene on Ir(111) was measured. This sample had a much lower oxygen coverage, roughly 8 % of the surface was covered with oxygen species. The WCA (1 cycle, 8 measurements) is found to be 73° ± 6°. Finally, the WCA (1 cycle, 8 measurements) of bare graphene on Ir(111) is found to be 82° ± 4°. Graphene with a high oxygen coverage, graphene with a low oxygen coverage and bare graphene have differnet chemical potentials, and if they were opque to wetting on Ir(111), the surfaces should exhibit different WCA.

Alternatively, two observed factors can influence the wettability (i) airborne contamination and (ii) defects i.e. carbon vacancies, grain boundaries, and wrinkles. Firstly, airborne hydrocarbons have been reported to make pristine graphene hydrophobic[43]. The fact that

graphene oxide is hydrophilic under normal treatment indicates that it is not prone to airborne contamination[15–18]. XPS spectra obtained after wetting and icing experiments suggest that enolate-functionalized oxidized graphene might be different. The XPS spectra indicate that hydrocarbons are present on the O-Gr/Ir(111) surface. This will be discussed in greater detail in Sec. III C. Secondly, it was predicted by Xu et al., that vacancy defects increase the WCA of graphene oxide[44]. As will be discussed in greater detail , XPS spectra as well as STM images obtained after the wetting and icing experiments show an increase in vacancy defects as well as intercalation of oxygen and/or water underneath the graphene[37,45–47]. Intercalation was mainly observed along the edges of the surface. These areas also had a lower density of functional groups. The WCA on the edges of the sample is found to be 79° ± 3° (average of five measurements). Thus regions with different chemical environments exhibit similar wettability, pointing again towards transparency to wetting. It should moreover be noted that we do not observe a significant change in WCA over a period of 4 cycles (see Fig. 6(a)).

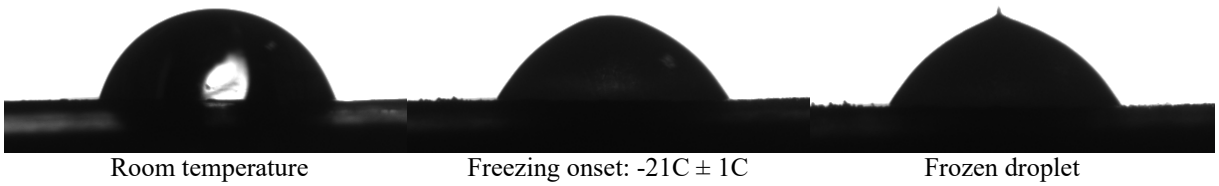

Figure 5: Snapshots of a sessile water droplet (2 μL) at room temperature (left), at the freezing onset where the doplet turns opaque (middle) and frozen state with the characteristic pointy-tip shape (right).

Figure 6(b) presents the WCA as a function of temperature. As the temperature decreases so does the WCA. For temperatures above 0°C this is due to condensation, and at subzero temperatures frost can facilitate spreading[48]. The freezing onset temperature of O-Gr/Ir(111) is found to be -21°C ± 1°C (see middle panel of Fig. 5). The freezing onset is assumed to mark the start of the freezing process. The droplet heats up adiabatically resulting in a mixed liquid/ice phase. This is evident as a loss of water clarity[49,50]. In the second stage of freezing, the ice front moves upwards and forms a pointy-tip-shaped ice droplet (see right panel of Fig. 5). Heat is now released to the substrate by conduction.

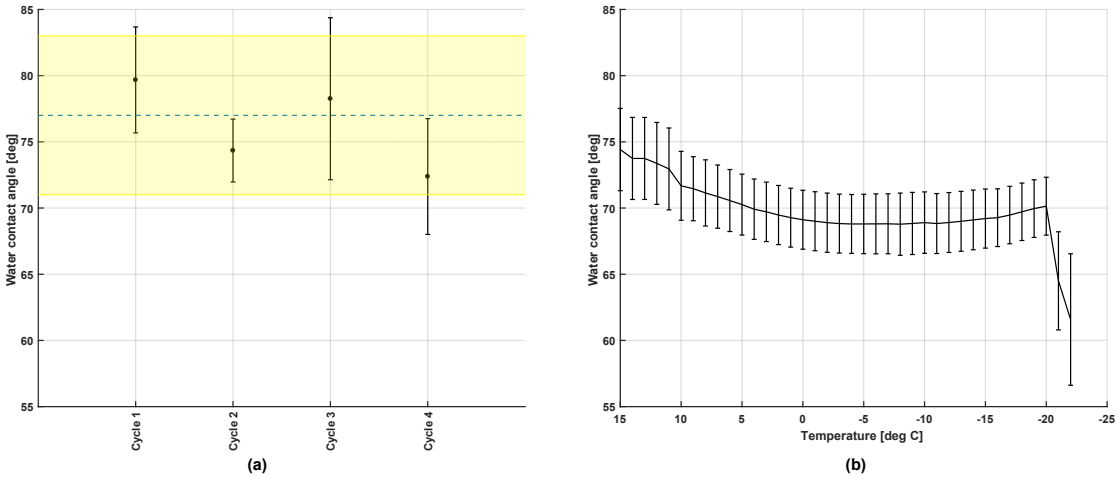

Figure 6: (a) Average WCA of O-Gr/Ir(111). The four cycles are obtained over the course of five days. The overall average (cycle 1 - cycle 4) is the dotted line with shaded errorbars. (b) Average WCA as a function of temperature. The plot is the average of eigth measurements (cycle 1). The freezing onset is found to be -21°C ± 1°C. When the droplet freezes, it changes apperance. This sudden change causes the large variation in the WCA around -20°C.

The large variations in WCA in Fig. 6(b) at temperatures around -20°C is a result of this sudden change in droplet appearance.

The freezing onset temperature is quite close to that of graphene oxide on silicon (down to -24.6°C)[27] and to that of fluorinated graphene on Ru(0001) on sapphire[50], where Akhtar et al.,[50] reported a freezing onset temperature of -23 °C ± 1°C (estimated 25 % fluorine coverage on graphene on Ru(0001) on sapphire), -20 °C ± 1°C (estimated 10 % fluorine coverage on graphene on Ru(0001) on sapphire) and -18 °C ± 1°C (graphene on Ru(0001) on sapphire). A theoretical study showed that functionalization (Na^+-, Cl^--ions, and methane) of graphene lowers the freezing onset temperature due to the formation of a viscous water layer on the surface[51]. Our results indicate that enolate-functionalized graphene exhibits similar properties. Furthermore, on the edges of O-Gr/Ir(111) sample the freezing onset temperature is found to be -18°C ± 1°C (WCA = 79° ± 3°). The post-icing surface analysis shows that the edges contain bare Ir-patches and regions with intercalated oxygen species (Gr/O/Ir(111)). The edges also have a lower density of functional groups. It thus appears that O-Gr is transparent to wetting, but not to icing. Put in other words, the wettability

of the surface is determined by the underlying Ir(111) substrate but the ability to prevent freezing is influenced by the functionalized graphene.

C. Surface analysis after the wetting and icing experiments

STM images of the O-Gr/Ir(111) obtained after the wetting and icing experiments are presented in Fig. 7. The bright elongated structures in Fig. 7(a), highlighted with a blue arrow, looks similar to the darker elongated structures in Fig. 3(a) and is therefore believed to be bare graphene (different scanning parameters give rise to the difference in contrast). Figure 7(a) thus shows a highly oxidized graphene surface. Within this area, the moiré lattice constant is found to be 2.62 ± 0.03 nm, proving that the moiré structure is intact. The dark holes, highlighted with a white arrow, were not observed prior to icing experiments, so they are likely defects induced by exposure to air, water and/or freezing.

Figure 7(b) shows bright elevated regions with white dot-like structures on top. The height profile of the blue line is given in the inset. The STM image and the height profile are in good agreement with previous reported values for water intercalated underneath graphene[52]. Each layer of water molecules correspond to a height difference of $\sim$ 1 Å. It has been suggested that water is not uniformly distributed underneath graphene, so the white dot-like structure is thus likely arising from a second layer of water. The dark holes correspond to the dark-hole defects observed in Fig. 7(a) (white arrow).

An atomically-resolved STM image of the area inside the black rectangle in Fig. 7(b) is shown in Fig. 7(c) with the FFT as the inset. This image reveals a hexagonal pattern of atoms with lattice constant corresponding to that of graphene, confirming that graphene rests on top of the elevated regions and that foreign species (presumably water and/or oxygen) are intercalated between the graphene and the Ir(111) surface (Gr/O/Ir(111)). The fact that graphene is visible in Fig. 7(c) implies that oxygen-containing groups are lost upon exposure to air/water and/or ice. Intercalation is only observed in regions where the functional groups are lost (see also Fig. S2 in Suppl. Material). Figure 7 hence shows that the chemical environment is not uniform across the surface after the wetting and icing experiments.

XPS spectra obtained after the wetting and icing experiments are given in Fig. 8. In the O1s spectrum, ether (O_2 at 532.1 eV), enolate (O_3 at 531.1), and oxygen species interacting

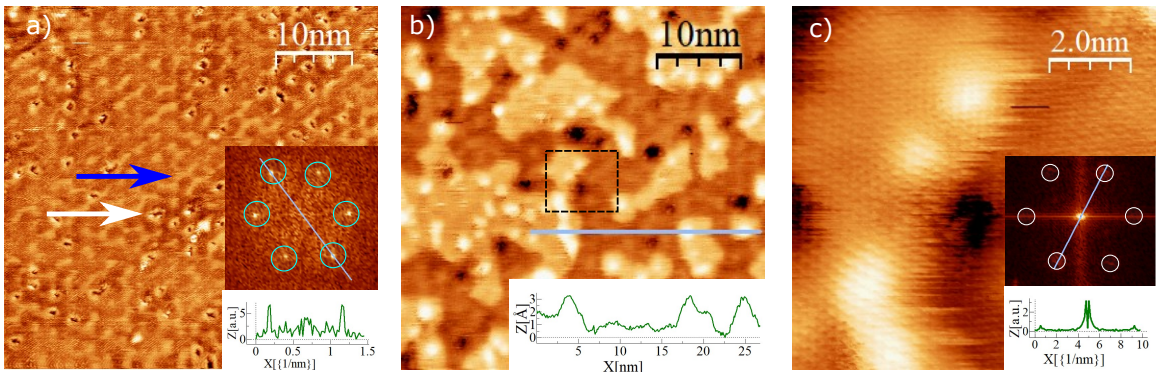

Figure 7: STM images obtained after completion of the wetting and icing experiments. In (a) the bright elongated structures (highlighted with a blue arrow) is likely bare graphene. In this region the surface is highly oxidized. The white arrow highlights a defect. The FTT and height profile shows the line spacing of the moiré structure. Scanning parameters: It: -440.0 pA, Vt: -38.8 mV. In (b) the elevated (bright) regions indicate water and/or oxygen intercalation. The height profile of the line scan is shown as an inset and it correlates well with values reported for water intercalation[52] (see main text). Scanning parameters: 470 pA, Vt: 38.8 mV. (c) Atomically resolved image of bare graphene obtained from the area marked with black rectangle in (b). The FFT and height profile shows the line spacing of the graphene hexagonal structure. Scanning parameters: It: -440.0 pA, Vt: 38.8 mV.

with Ir(111) (O_4 at 530.1 eV) dominate the detected signal. O_4 originates from oxygen species (e.g. O, OH, H_2O) that are either intercalated or interacting with bare Ir(111). The ether component can originate from (i) damaged graphene and/or (ii) organic dust (including hydrocarbons) adsorbed to the graphene. In the C1s spectrum most of the signal has shifted by 1 eV to higher binding energy, indicating a shift from predominantly sp^2 carbon to predominantly sp^3 carbon. Additionally, the C_5 component originates from graphene that has decoupled from Ir(111) in intercalated areas.

XPS spectra obtained at the edge of the sample are included in Fig. S2 in Suppl. Material. It shows that the chemical environment at the edges differs significantly from that at the center of the sample. As already mentioned, the center consists of highly functioalized regions, as well as hydrocarbons and vacancies. Along the edges, there are intercalated oxygen species and bare Ir patches, and less functionalized regions. Bare Ir(111) (which

can be seen in Fig. S1 in Suppl. Material) and grain boundaries have been reported to be possible intercalation routes[37,45], and intercalation is only observed in regions where oxygen-containing functional groups are lost.

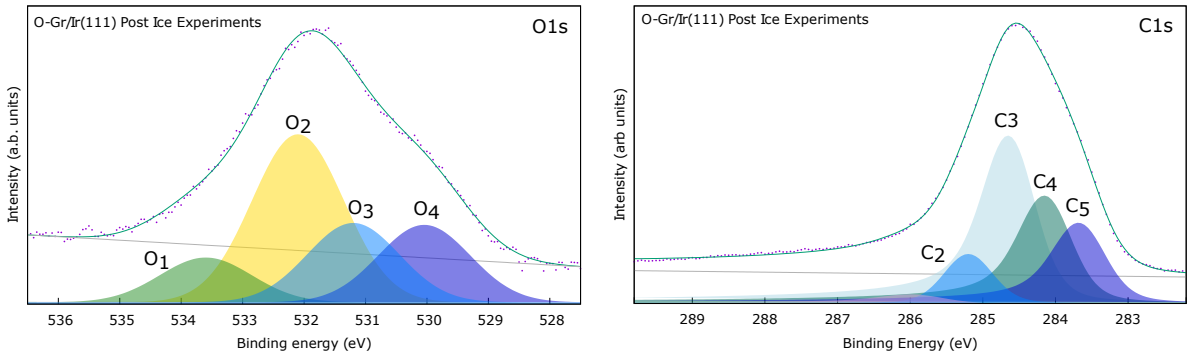

Figure 8: XPS spectra of O1s (left panel) and C1s (right panel) peaks measured in the MatLine beamline. The purple dots are the raw data, the green curve is the fit and the gray line is the background. Peak details can be found in supplementary material.

IV. CONCLUSION

In this work the wetting and icing properties of enolate functionalized graphene on Ir(111) are studied. The surface is almost hydrophobic at room temperature with a WCA 80° ± 4°. The observed WCA is significantly larger than what is reported on untreated, standard graphene oxide with hydroxyl- and epoxy groups which is hydrophilic. The observed WCA is argued to be caused by wetting transparency, but is also discussed with respect to adsorption of airborne contaminants, and intercalation of water and/or oxygen. The freezing onset temperature of the O-Gr/Ir(111) surface is found to be -21°C ± 1°C, indicating that enolate-functionalized graphene exhibit the property theoretically predicted for functionalized graphene and experimentally demonstrated for fluorinated graphene, namely a lowering of the freezing onset temperature compared to that of bare graphene. In theory this lowering is contributed to the formation of a viscous water layer on the surface. This suggests that O-Gr on Ir(111) is transparent to wetting, but not to icing. The STM images and the XPS spectra demonstrate that the chemical environment of the surface change after exposure to air, water and ice.

V. ACKNOWLEDGMENT

R.F is funded by the Norwegian Research Council's FORNY programme.

VI. SUPPLEMENTARY MATERIAL

Figure S1 show STM images of Gr/Ir(111) sample before oxygen exposure. In S1(a) a small patch of bare Ir(111) is visible. This was the only patch containing bare Ir(111) that was observed, larger areas were scanned. Therefore, only a very small percentage of the surface was assumed to consist of bare Ir(111). The larger pattern visible in Fig. S1(a)-(c) is the moiré superstructure that arises from the lattice mismatches between Ir(111) and graphene The hexagonal pattern is visible in the FFT inset in Fig. S1(b) and the moiré lattice constant was found to be 2.5 nm ± 0.1 nm. The unit cell of the moiré superstructure is shown with a black rhombus in Fig. S1(c)

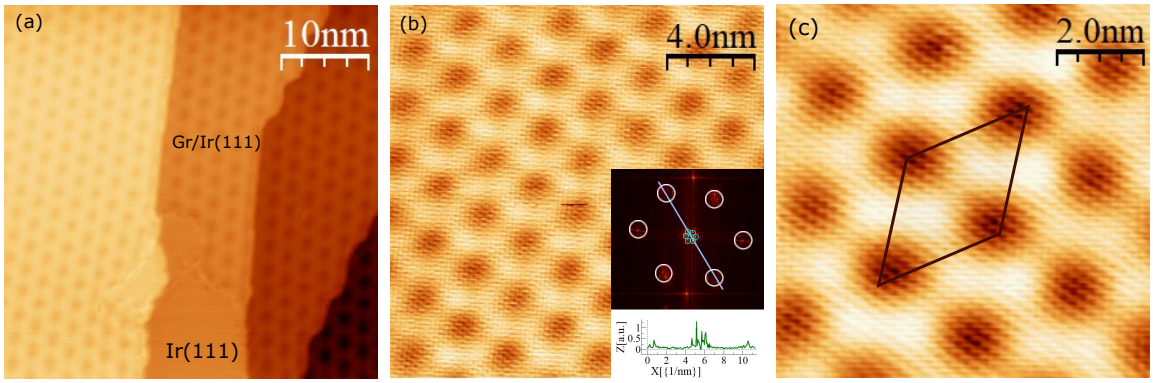

Figure S1: STM images of graphene on Ir(111) prior to the wetting and icing experiments. (a) STM image showing the moiré structure and a small patch of bare Ir(111) . The atomic steps on the Ir(111) surface are clearly visible. Scanning parameters: It: 350.0 pA, Vt: 57.1 mV (b) Atomic-resolution image with corresponding FFT spectrum. The moiré lattice constant was found to be 2.5 ± 0.1 nm, in good agreement with literature[35]. The rhombus hihglights the moiré unit cell. Scanning parameters: It: -920.0 pA, Vt: -2.4 mV.

Table S1 and S2 presents assosiated peaks to Fig. 4. and Fig. S2.

Table S1: Binding energy (BE), Gaussian full width at half maximum (GFWHM) and associated bond assignment/groups of O1s XPS peaks in Fig. 4 and Fig. S2. The XPS data were obtained prior to the wetting and icing experiments. A Gaussian function with a linear background is fitted to the peaks.

Component	BE (eV)	GFWHM (eV)	Assignment
	O-Gr/Ir(111)		
O_1	533.60	2.17	C-OH[14]
O_2	532.10	2.17	C-O-C[36]
O_3	531.20	2.17	C-O[31]
O_5	528.80	2.17	C=O[31]
	Gr/Ir(111)		
O_1	533.60	2.50	C-OH[14]
O_2	532.20	2.50	C-O-C[36]
O_3	531.10	2.50	C-O[31]
O_5	528.80	2.50	C=O[31]

Table S2: Binding energy (BE), Gaussian full width at half max (GFWHM), Lorentzian full width at half max (LFWHM), asymmetric fraction allowed (asym) and associated bond assignment/groups of XPS C1s peaks in Fig. 4 and Fig. S2. The XPS data were obtained prior to the wetting and icing experiments. The peaks are fitted by a Doniach-Sunjic function convolved with a Gaussian function and a linear background.

Component	BE (eV)	GFWHM (eV)	LFWHM (eV)	Asym	Assignment
			O-Gr/Ir(111)		
Ir4d	287.36	2.30	0.50	0.12	Diffraction peak
C_1	285.90	0.90	0.28	0.12	C=O[31]
C_2	285.20	0.70	0.07	0.00	C-O-C[36]
C_3	284.60	0.60	0.14	0.07	C-O[31,36]
C_4	284.12	0.60	0.14	0.1	C-C
C_5	283.58	0.6	0.14	0.05	Decoupled graphene[37]
			Gr/Ir(111)		
Ir4d	287.30	2.30	0.50	0.12	Diffraction Peak
C_1	285.90	0.90	0.08	0.04	C=O[31]
C_2	285.25	0.58	0.01	0.00	C-O-C[36]
C_3	284.60	0.60	0.14	0.11	C-O[31,36]
C_4	284.08	0.60	0.14	0.10	C-C
C_5	283.59	0.60	0.14	0.00	Decoupled graphene[37]

Table S3: Summary of the XPS O1s peaks and fitting parameters obatined after the wetting and icing experiments in the MatLine beamline, presented in Fig. 8. The peaks are fitted using Gaussian with linear background. BE stands for binding energy and GFWHM Gaussian full width half maximum.

Component	**BE (eV)**	**GFWHM (eV)**	**assignment**
O_1	533.60	1.76	C-OH[14]
O_2	532.10 (eV)	1.76	C-O-C[36]
O_3	531.20 (eV)	1.76	C-O[31]
O_4	530.04 (eV)	1.76	O-Ir(111)[37]
O_5	528.80 (eV)	1.76	C=O[31]

Table S4: Summary of the XPS C1s peaks and fitting parameters obatined after the wetting and icing experiments in the MatLine beamline, presented in Fig. 8. The peaks are fitted using Doniach-Sunjic function convoluted with a Gaussian, and a linear background. BE stands for binding energy, GFWHM and LFWHM for Gaussian and Lorenzian full width half maximum respectively and asym for the asymmetric fraction allowed.

Component	**BE (eV)**	**GFWHM (eV)**	**LFWHM (eV)**	**asym**	**assignment**
C_1	285.80	0.55	0.00	0.12	C=O[31]
C_2	285.20	0.69	0.15	0.00	C-O-C[36]
C_3	284.60	0.68	0.23	0.12	C-O[3136]
C_4	284.1	0.68	0.23	0.12	C-C[31]
C_5	283.62	0.68	0.23	0.12	Decoupled graphene[37]

In addition to the synchrotron XPS spectra presented in the main text, the laboratory XPS was used to collect data after icing experiments with both incident and grazing emission, and one spectrum collected at the edge of the sample. The laboratory XPS spectra (O1s and C1s) are presented in Figure S2. The spectra recorded before the wetting and icing experiments are included in the figure for comparison. Peak details are given in Table S5 and S6.

In the O1s spectrum before the wetting and icing experiments, the O_3 component (531.2 eV) which is assigned to enolates, dominates[31] (as discussed in the main text). In the O1s spectrum recorded after the wetting and icing experiments obtained with normal emission, the enolate component, O_3, is significantly suppressed. The ether-component (O_2) and O-Ir component (O_4) dominate the detected signal, which accumulatively indicates damaged graphene and/or a contaminated surface, as well as intercalation. The signal from the enolate group is likely buried in the signal from the two more intense peaks. Grazing angle emission is more surface sensitive and a probe larger area of the sample. In the O1s grazing angle spectrum, the enolate peak O_3 dominates, whereas the O_4-peak (O-Ir) is significantly reduced. The O1s spectrum collected from the edges of the sample differs from the spectrum recorded at the center of the sample and contains roughly similar contributions from O_3 and O_4. This suggests that oxygen is interacting with Ir, either intercalated or on bare Ir patches, dominate at the edges.

In the C1s spectrum before the icing and wetting experiments, C_4 is the dominant component. In the C1s spectrum recorded with normal emission after the wetting and icing experiments most of the signal has shifted with 1 eV to higher binding energies. This indicates a shift from an abundance of sp^2-carbons to an abundance of sp^3-carbons. The ether component (C_2) dominates the signal, in good agreement with the O1s spectrum. The sp3/sp2 ratio has increased from 0.91 (pre icing) to 2.55 (after icing). In the grazing emission C1s spectrum, the sp3/sp2 ratio is 3.53, however, there is a larger contribution from the sp^2-component (C_4). This can again be explained by the fact that grazing emission collects data from a larger area of the sample, including the edges. It thus seems like there is more intercalation (C_5) and less sp^3 carbon on the edges. The edge-C1s spectrum confirms this hypothesis. The sp^3 peaks are less prominent compared to the C1s grazing emission

spectrum, implying that there are less organic dust and fewer damages on the graphene on the edge compared to the center of the sample. Moreover, less sp^3-carbon implies less functional groups. Thus functional groups are lost on the edge of the sample and in these regions intercalation is observed.

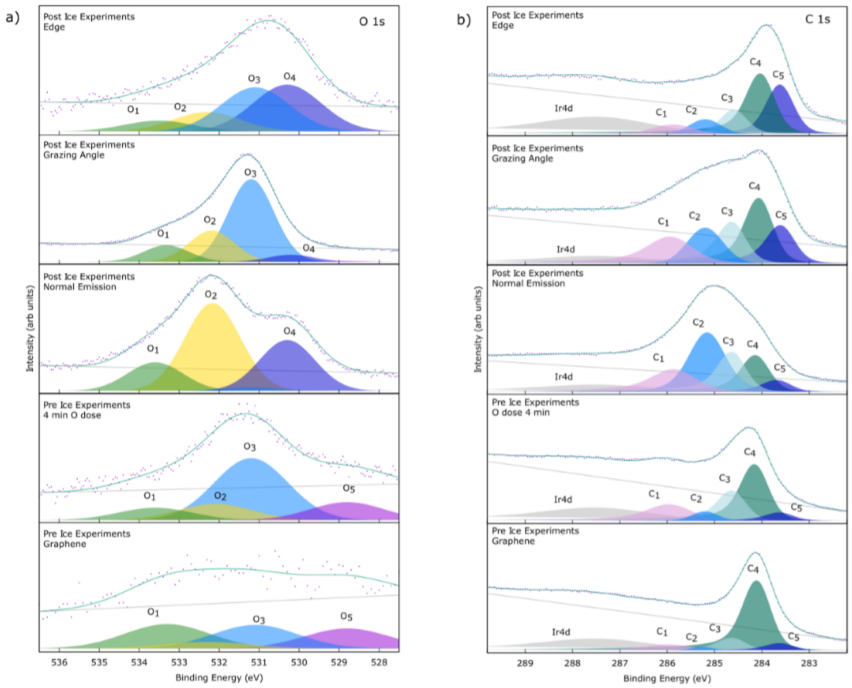

Figure S2: Laboratory XPS spectra obtained before and after the wetting and icing experiments. (a) O1s and (b) C1s

Table S5: Summary of the XPS O1s peaks and fitting parameters obatined after the wetting and icing experiments in the MatLine beamline, presented in Fig. 8. The peaks are fitted using Gaussian with linear background. BE stands for binding energy and GFWHM Gaussian full width half maximum.

Component	**BE (eV)**	**GFWHM (eV)**	**assignment**
O-GrIr(111) Post Ice Experiments Edge			
O_1	533.52	2.00	C-OH[14]
O_2	532.30	2.00	C-O-C[36]
O_3	531.10 (eV)	2.00	C-O[31]
O_4	530.30 (eV)	2.00	O-Ir(111)[37]
O_5	528.80 (eV)	2.00	C=O[31]
O-GrIr(111) Post Ice Experiments Grazing Emission			
O_1	533.32	1.34	C-OH[14]
O_2	532.19 (eV)	1.34	C-O-C[36]
O_3	531.20 (eV)	1.34	C-O[31]
O_4	530.20 (eV)	1.34	O-Ir(111)[37]
O_5	528.80 (eV)	1.34	C=O[31]
O-GrIr(111) Post Ice Experiments Normal Emission			
O_1	533.60	1.64	C-OH[14]
O_2	532.16 (eV)	1.64	C-O-C[36]
O_3	531.20 (eV)	1.64	C-O[31]
O_4	530.30 (eV)	1.64	O-Ir(111)[37]
O_5	528.80 (eV)	1.64	C=O[31]

Table S6: Summary of the XPS C1s peaks and fitting parameters obatined after the wetting and icing experiments in the MatLine beamline, presented in Fig. 8. The peaks are fitted using Doniach-Sunjic function convoluted with a Gaussian, and a linear background. BE stands for binding energy, GFWHM and LFWHM for Gaussian and Lorenzian full width half maximum respectively and asym for the asymmetric fraction allowed.

Component	**BE (eV)**	**GFWHM (eV)**	**LFWHM (eV)**	**asym**	**assignment**
		O-GrIr(111) Post Ice Experiments Edge			
Ir4d	287.30	2.30	0.50	0.12	Diffraction peak
C_1	285.90	0.85	0.03	0.05	C=O[31]
C_2	285.20	0.90	0.04	0.00	C-O-C[36]
C_3	284.60	0.65	0.15	0.00	C-O[31,36]
C_4	284.00	0.65	0.15	0.10	C-C
C_5	283.63	0.65	0.15	0.07	Decoupled graphene[37]
		O-GrIr(111) Post Ice Experiments Grazing Emission			
Ir4d	287.36	2.30	0.12	0.50	Diffraction peak
C_1	285.87	0.88	0.09	0.11	C=O[31]
C_2	285.21	0.90	0.04	0.00	C-O-C[36]
C_3	284.56	0.65	0.11	0.15	C-O[31,36]
C_4	284.00	0.65	0.15	0.10	C-C
C_5	283.56	0.65	0.15	0.11	Decoupled Graphene[37]
		O-GrIr(111) Post Ice Experiments Normal Emission)			
Ir4d	287.36	2.30	0.50	0.10	Diffraction peak
C_1	285.90	0.74	0.29	0.12	C=O[31]
C_2	285.20	0.80	0.00	0.30	C-O-C[36]
C_3	284.60	0.65	0.15	0.12	C-O[31,36]
C_4	284.07	0.65	0.15	0.10	C-C
C_5	283.60	0.65	0.15	0.12	Decoupled Graphene[37]

REFERENCES

[1]A. Geim, Physica Scripta **2012**, 014003 (2012).

[2]D. C. Marcano, D. V. Kosynkin, J. M. Berlin, A. Sinitskii, Z. Sun, A. Slesarev, L. B. Alemany, W. Lu, and J. M. Tour, ACS nano **4**, 4806 (2010).

[3]Z. Xu, H. Sun, X. Zhao, and C. Gao, Advanced Materials **25**, 188 (2013).

[4]R. Joshi, S. Alwarappan, M. Yoshimura, V. Sahajwalla, and Y. Nishina, Applied Materials Today **1**, 1 (2015).

[5]D. A. Dikin, S. Stankovich, E. J. Zimney, R. D. Piner, G. H. Dommett, G. Evmenenko, S. T. Nguyen, and R. S. Ruoff, Nature **448**, 457 (2007).

[6]R. K. Upadhyay, S. Naicker, A. Barman, S. S. Roy, T. Thundat, and P. R. Waghmare, Chemical Engineering Journal **354**, 149 (2018).

[7]S. Schöche, N. Hong, M. Khorasaninejad, A. Ambrosio, E. Orabona, P. Maddalena, and F. Capasso, Applied Surface Science **421**, 778 (2017).

[8]F. Li, X. Jiang, J. Zhao, and S. Zhang, Nano energy **16**, 488 (2015).

[9]Y. Wei, Y. Zhang, X. Gao, Z. Ma, X. Wang, and C. Gao, Carbon **139**, 964 (2018).

[10]S. Basu and P. Bhattacharyya, Sensors and Actuators B: Chemical **173**, 1 (2012).

[11]J. Hu, Y. Ji, Y. Shi, F. Hui, H. Duan, and M. Lanza, Ann. J. Mater. Sci. Eng **1**, 16 (2014).

[12]D. R. Dreyer, S. Park, C. W. Bielawski, and R. S. Ruoff, Chemical society reviews **39**, 228 (2010).

[13]S. Zhou and A. Bongiorno, Scientific reports **3**, 2484 (2013).

[14]D. S. Shin, H. G. Kim, H. S. Ahn, H. Y. Jeong, Y.-J. Kim, D. Odkhuu, N. Tsogbadrakh, B. H. Kim, *et al.*, RSC advances **7**, 13979 (2017).

[15]N. Wei, C. Lv, and Z. Xu, Langmuir **30**, 3572 (2014).

[16]P. Sun, M. Zhu, K. Wang, M. Zhong, J. Wei, D. Wu, Z. Xu, and H. Zhu, ACS nano **7**, 428 (2013).

[17]X. Zhang, P. Song, and X. Cui, Thin Solid Films **520**, 3539 (2012).

[18]C.-T. Hsieh and W.-Y. Chen, Surface and Coatings Technology **205**, 4554 (2011).

[19]R. Rasuli, Z. Mokarian, R. Karimi, H. Shabanzadeh, and Y. Abedini, Thin Solid Films **589**, 364 (2015).

[20]L. A. Belyaeva and G. F. Schneider, Surface Science Reports , 100482 (2020).

[21]L. A. Belyaeva, P. M. van Deursen, K. I. Barbetsea, and G. F. Schneider, Advanced materials **30**, 1703274 (2018).

[22]A. V. Prydatko, L. A. Belyaeva, L. Jiang, L. M. Lima, and G. F. Schneider, Nature communications **9**, 1 (2018).

[23]D. Kim, N. M. Pugno, M. J. Buehler, and S. Ryu, Scientific reports **5**, 15526 (2015).

[24]Y. Zheng, C. Su, J. Lu, and K. P. Loh, Angewandte Chemie International Edition **52**, 8708 (2013).

[25]M. Zokaie and M. Foroutan, RSC Advances **5**, 97446 (2015).

[26]H. Geng, X. Liu, G. Shi, G. Bai, J. Ma, J. Chen, Z. Wu, Y. Song, H. Fang, and J. Wang, Angewandte Chemie International Edition **56**, 997 (2017).

[27]G. Bai, D. Gao, Z. Liu, X. Zhou, and J. Wang, Nature **576**, 437 (2019).

[28]N. A. Vinogradov, K. Schulte, M. L. Ng, A. Mikkelsen, E. Lundgren, N. Martensson, and A. Preobrajenski, The Journal of Physical Chemistry C **115**, 9568 (2011).

[29]M. Z. Hossain, J. E. Johns, K. H. Bevan, H. J. Karmel, Y. T. Liang, S. Yoshimoto, K. Mukai, T. Koitaya, J. Yoshinobu, M. Kawai, *et al.*, Nature chemistry **4**, 305 (2012).

[30]Z. Novotny, M.-T. Nguyen, F. P. Netzer, V.-A. Glezakou, R. Rousseau, and Z. Dohnalek, Journal of the American Chemical Society **140**, 5102 (2018).

[31]A. Cassidy, S. Pedersen, H. Bluhm, V. Calisti, T. Angot, E. Salomon, R. Bisson, and L. Hornekaer, Physical Chemistry Chemical Physics **20**, 28370 (2018).

[32]E. Lægsgaard, F. Besenbacher, K. Mortensen, and I. Stensgaard, Journal of microscopy **152**, 663 (1988).

[33]I. Horcas, R. Fernández, J. Gomez-Rodriguez, J. Colchero, J. Gómez-Herrero, and A. Baro, Review of scientific instruments **78**, 013705 (2007).

[34]https://www.kolibrik.net/en/kolxpd, Accessed: June 10 2020.

[35]J. Coraux, T. N. Plasa, C. Busse, T. Michely, *et al.*, New Journal of Physics **10**, 043033 (2008).

[36]R. Larciprete, S. Fabris, T. Sun, P. Lacovig, A. Baraldi, and S. Lizzit, Journal of the American Chemical Society **133**, 17315 (2011).

[37]E. Granas, J. Knudsen, U. A. SchroÌˆder, T. Gerber, C. Busse, M. A. Arman, K. Schulte, J. N. Andersen, and T. Michely, ACS nano **6**, 9951 (2012).

[38]N. Giovambattista, P. G. Debenedetti, and P. J. Rossky, The Journal of Physical Chemistry B **111**, 9581 (2007).

[39]C.-J. Shih, Q. H. Wang, S. Lin, K.-C. Park, Z. Jin, M. S. Strano, and D. Blankschtein, Physical review letters **109**, 176101 (2012).

[40]C.-J. Shih, M. S. Strano, and D. Blankschtein, Nature materials **12**, 866 (2013).

[41]J. Rafiee, X. Mi, H. Gullapalli, A. V. Thomas, F. Yavari, Y. Shi, P. M. Ajayan, and N. A. Koratkar, Nature materials **11**, 217 (2012).

[42]K. Göbbels, T. Kuenzel, A. van Ooyen, W. Baumgartner, U. Schnakenberg, and P. Bräunig, Biomaterials **31**, 1055 (2010).

[43]Z. Li, Y. Wang, A. Kozbial, G. Shenoy, F. Zhou, R. McGinley, P. Ireland, B. Morganstein, A. Kunkel, S. P. Surwade, *et al.*, Nature materials **12**, 925 (2013).

[44]K. Xu, J. Zhang, X. Hao, C. Zhang, N. Wei, and C. Zhang, Molecules **23**, 1439 (2018).

[45]X. Feng, S. Maier, and M. Salmeron, Journal of the American Chemical Society **134**, 5662 (2012).

[46]R. Nair, H. Wu, P. Jayaram, I. Grigorieva, and A. Geim, Science **335**, 442 (2012).

[47]G. He, Q. Wang, H. K. Yu, D. Farías, Y. Liu, and A. Politano, Nano Research **12**, 3101 (2019).

[48]G. Heydari, E. Thormann, M. JaÌˆrn, E. Tyrode, and P. M. Claesson, The Journal of Physical Chemistry C **117**, 21752 (2013).

[49]S. Jung, M. Dorrestijn, D. Raps, A. Das, C. M. Megaridis, and D. Poulikakos, Langmuir **27**, 3059 (2011).

[50]N. Akhtar, G. Anemone, D. Farias, and B. Holst, Carbon **141**, 451 (2019).

[51]X.-X. Zhang and M. Chen, Journal of Nanomaterials **2016** (2016).

[52]K. T. He, J. D. Wood, G. P. Doidge, E. Pop, and J. W. Lyding, Nano letters **12**, 2665 (2012).